JETP Letters, Vol. 82, No. 5, 2005, pp. 243–247. Translated from Pis'ma v Zhurnal Éksperimental'noĭ i Teoreticheskoĭ Fiziki, Vol. 82, No. 5, 2005, pp. 275–278.
Original Russian Text Copyright © 2005 by Pupyshev.

Extrapolation of the Differential Cross Section for Triplet *pp* Scattering to Low Energies

V. V. Pupyshev

Joint Institute for Nuclear Research, Dubna, Moscow region, 141980 Russia

e-mail: pupyshev@thsun1.jinr.ru

Received June 16, 2005; in final form, July 14, 2005

It has been shown that the differential cross section for low-energy triplet *pp* scattering that is caused by the sum of the nuclear and magnetic interactions in the Coulomb field of the protons is a rapidly oscillating function and has second-order poles in the forward and backward directions. In order to extrapolate such a cross section to the energy region below 10 MeV, a simple low-energy approximation has been proposed. New phenomena—proton–proton analogues of the Mott and Schwinger effects—are discussed. © *2005 Pleiades Publishing, Inc.*

PACS numbers: 03.65.Nk, 13.40.Ks, 13.75.Gs

1. INTRODUCTION

This work continues the preceding study [1] of the role of the magnetic interaction in low-energy triplet *pp* scattering. Let us recall the commonly accepted *pp* model [2] used in this work.

The proton scattering is described by the standard Schrödinger equation with the total interaction $V^{ca} = V^{\mathrm{c}} + V^{a}$, where V^a decreases for $r \longrightarrow \infty$ faster than the Coulomb potential $V^{\mathrm{c}}(r) = m_p(e/\hbar)^2/r = 1/rR$, where m_p is the proton mass, e is the elementary charge, r is the interproton distance, and R is the Bohr radius of the *pp* system.

Three cases are theoretically possible. In the first case, $a = \mathrm{s}$ and $V^a = V^{\mathrm{s}}$ is the short-range nuclear interaction. In the second case, $a = m$ and $V^a = V^{\mathrm{m}}$ is the magnetic interaction. In the third, most realistic, case, $a = ms$ and $V^a = V^{\mathrm{ms}} = V^{\mathrm{m}} + V^{\mathrm{s}}$ is the superposition of the magnetic and nuclear interactions. The magnetic interaction is the sum $V^{\mathrm{m}} = V^{\mathrm{mt}} + V^{\mathrm{m}ls}$ of the tensor interaction between the magnetic moments of the protons

$$V^{\mathrm{mt}} \equiv b_{\mathrm{t}}\frac{S_{12}}{r^3}, \quad b_{\mathrm{t}} \equiv -\frac{m_p}{\hbar^2}\mu_p^2\mu_0^2, \qquad S_{12} \equiv [3(\mathbf{s}_1 \cdot \mathbf{r})(\mathbf{s}_2 \cdot \mathbf{r}) - r^2(\mathbf{s}_1 \cdot \mathbf{s}_2)]/4r^2, \tag{1}$$

and the spin–orbit interaction of the magnetic moment of one proton with the electromagnetic field of the other proton

$$V^{\mathrm{m}ls} = b_{ls}\frac{(\mathbf{l} \cdot \mathbf{s})}{r^3}, \quad b_{ls} \equiv -\frac{m_p}{\hbar^2}8\mu_0^2\left(\mu_p - \frac{1}{4}\right). \tag{2}$$

Here, μ_p is the magnetic moment of the proton in μ_0 magneton units; $\mathbf{s}_1$ and $\mathbf{s}_2$ are the proton spin operators; and $\mathbf{s} \equiv \mathbf{s}_1 + \mathbf{s}_2$, $\mathbf{l}$, and $\mathbf{j} \equiv \mathbf{l} + \mathbf{s}$ are the operators of the spin, orbital angular momentum, and total angular momentum of the *pp* system, respectively. In calculations, the soft-core Reid potential [3] is used as V^{s}.

Let us introduce the following notation: k is the momentum, $E = (k\hbar)^2/m_p$ is the energy, and θ and φ are the scattering angles of the protons; $q \equiv kR$ and $\eta \equiv 1/2q$ are the dimensionless parameters; $\delta_{l,j}^{\mathrm{c},a}$, $\varepsilon_j^{\mathrm{c},a}$, and $d\sigma^{\mathrm{c},a}(\theta;\, q) = d\sigma^{\mathrm{c},a}/d\theta\sin\theta$ are the phases, mixing parameters, and differential cross section, respectively, for scattering caused by the interaction V^a in the field V^{c}. The phase $\delta_{l,j}^{\mathrm{c},a}$ is equal to the difference between the total phase $\delta_{l,j}^{\mathrm{c}a}$ of scattering caused by the superposition $V^{\mathrm{c}} + V^a$ and the Coulomb phase δ_l^{c}. The phases $\delta_{l,j}^{\mathrm{c},a}$ and cross sections $d\sigma^{\mathrm{c},a}$ for the cases $a = \mathrm{s}$, m, and ms are called Coulomb–nuclear, Coulomb–magnetic, and Coulomb–magnetic–nuclear.

The main aim of this work is to fill a gap in the theory of low-energy *pp* scattering, namely, to derive a simple formula that is appropriate for extrapolation of the Coulomb–magnetic–nuclear cross section $d\sigma^{\mathrm{c,ms}}$ to the low-energy region ($E < 10$ MeV) and explicitly reproduces all low-energy and angular features of such a cross section. To discuss these features, it is necessary to recall the Mott [4] and Schwinger [5] effects.

The Mott effect [6] is manifested as fast oscillations in the differential cross section for the low-energy Coulomb scattering of two identical particles that have the form $\cos\{2\eta\ln[\cot(\theta/2)]\}$, where θ is the scattering angle and η is the Sommerfeld parameter.

0021-3640/05/8205-0243$26.00 © 2005 Pleiades Publishing, Inc.

The Schwinger effect [7] is a rapid increase in the differential cross section $d\sigma_n$ for the neutron scattering by a spinless nucleus at small scattering angles ($d\sigma_n \approx \mathrm{const}[\cot(\theta/2)]^2$, $\theta \longrightarrow 0$). This increase is caused by the spin–orbit interaction of the magnetic moment of the neutron with the electromagnetic field of the nucleus.

2. ANALYSIS OF THE CROSS SECTIONS

We begin to derive low-energy approximate formulas ($q \longrightarrow 0$) for the cross section $d\sigma^{\mathrm{c},a}$, $a = s$, m, and ms. According to Table II in [8],

$$\begin{aligned} d\sigma^{\mathrm{c},a} &= \pi[(1/2)|M_{00}^{\mathrm{c},a}|^2 + |M_{10}^{\mathrm{c},a}|^2 \\ &+ |M_{01}^{\mathrm{c},a}|^2 + |M_{1,-1}^{\mathrm{c},a}|^2 + |M_{11}^{\mathrm{c},a}|^2], \end{aligned} \tag{3}$$

where the amplitudes $M_{nn'}^{\mathrm{c},a}(\varphi, \theta; q)$ are represented as series containing associated Legendre polynomials P_l^n with $l = 1, 3, \ldots$ and the partial amplitudes

$$\begin{aligned} \alpha_{l,j}^{\mathrm{c},a} &= \exp(2i\delta_l^{\mathrm{c}})[\cos 2\varepsilon_j^{\mathrm{c},a}\exp(2i\delta_{l,j}^{\mathrm{c},a}) - 1], \\ \alpha_j^{\mathrm{c},a} &= i\sin 2\varepsilon_j^{\mathrm{c},a}\exp\{i[\delta_{j+1,j}^{\mathrm{c},a} + \delta_{j-1,j}^{\mathrm{c},a}]\}. \end{aligned} \tag{4}$$

In particular,

$$\begin{aligned} M_{10}^{\mathrm{c},a} &= R\frac{\exp(-i\varphi)}{\sqrt{2}iq}\sum_{l=1,3,\ldots}\Bigg\{\alpha_{l,l+1}^{\mathrm{c},a} - \alpha_{l,l-1}^{\mathrm{c},a} \\ &+ \left[\frac{l+2}{l+1}\right]^{1/2}\alpha_{l+1}^{\mathrm{c},a} - \left[1 - \frac{1}{l}\right]^{1/2}\alpha_{l-1}^{\mathrm{c},a}\Bigg\}P_l^1(\cos\theta). \end{aligned}$$

Each series $M_{nn'}^{\mathrm{c},a}$ can be represented in the form

$$M_{nn'}^{\mathrm{c},a} = M_{nn'}^{\mathrm{c},a}(j \le 2) + M_{nn'}^{\mathrm{c},a}(j > 2), \tag{5}$$

where the sum $M_{nn'}^{\mathrm{c},a}(j \le 2)$ is the contribution from the pp states with $j \le 2$ and the series $M_{nn'}^{\mathrm{c},a}(j > 2)$ is the contribution from all other terms. As is known [1], all parameters $\delta_{l,j}^{\mathrm{c},a}$ and $\varepsilon_j^{\mathrm{c},a}$ for $a = s$, m, and ms are much less than unity for $E < 10$ MeV. For this reason, we set $\alpha_{l,j}^{\mathrm{c},a} \approx 2i\exp(2i\delta_l^{\mathrm{c}})\delta_{l,j}^{\mathrm{c},a}$ and $\alpha_j^{\mathrm{c},a} \approx 0$ for all partial amplitudes given by Eqs. (4).

Let us analyze the Coulomb–nuclear scattering ($a = s$). For $q \longrightarrow 0$, all Coulomb–nuclear phases decrease rapidly

$$\delta_{l,j}^{\mathrm{c},\mathrm{s}}(q) \sim q^{2l+1}\exp(-\pi\eta). \tag{6}$$

Therefore, the main contribution to the amplitudes $M_{nn'}^{\mathrm{c},\mathrm{s}}$ comes from the pp states with $j < 2$ and the standard approximation $M_{nn'}^{\mathrm{c},\mathrm{s}} \approx M_{nn'}^{\mathrm{c},\mathrm{s}}(j < 2)$ is valid. In this approximation, the Coulomb–nuclear cross section given by Eq. (3) is equal to the sum $d\sigma_2^{\mathrm{c},a}$ with $a = s$:

$$\begin{aligned} d\sigma_2^{\mathrm{c},a} \equiv \pi(R/q)^2\Bigg\{&[2(\delta_{1,0}^{\mathrm{c},a} + 2\delta_{1,2}^{\mathrm{c},a})^2 \\ &+ 9(\delta_{1,1}^{\mathrm{c},a} + \delta_{1,2}^{\mathrm{c},a})^2](\cos\theta)^2 \\ &+ \left[\frac{9}{2}(\delta_{1,1}^{\mathrm{c},a} - \delta_{1,2}^{\mathrm{c},a})^2 + 2(\delta_{1,2}^{\mathrm{c},a} - \delta_{1,0}^{\mathrm{c},a})^2\right](\sin\theta)^2\Bigg\}. \end{aligned} \tag{7}$$

All phases $\delta_{l,j}^{\mathrm{c},\mathrm{s}}$ in this sum can be approximated as [1]

$$\delta_{1,j}^{\mathrm{c},\mathrm{s}} \approx \bar{\delta}_{1,j}^{\mathrm{c},\mathrm{s}} \equiv -q^3C_1^2(\eta)A_{1,j}^{\mathrm{c},\mathrm{s}}[1 + h^{\mathrm{c}}(\eta)q^3C_1^2(\eta)A_{1,j}^{\mathrm{c},\mathrm{s}}], \tag{8}$$

where $h^{\mathrm{c}}(\eta)$ and $C_1^2(\eta)$ are the known Coulomb functions and $A_{1,j}^{\mathrm{c},\mathrm{s}}$ are the Coulomb–nuclear scattering lengths for the soft-core Reid interaction.

Let us analyze Coulomb–magnetic scattering ($a = m$) for the case $V^{\mathrm{m}} = V^{\mathrm{m}ls}$, when all phases $\delta_{l,j}^{\mathrm{c},\mathrm{m}}$ have the low-energy asymptotic form [1, 9]

$$\begin{aligned} \tilde{\delta}_{l,j}^{\mathrm{c},\mathrm{m}}(q) &= [j(j+1) - l(l+1) - s(s+1)]\tau_l(q), \\ \tau_l(q) &\equiv -q\frac{b_{ls}}{R}\frac{2l + 1 - \eta[\pi - 2\mathrm{Im}\psi(l + 1 + i\eta)]}{2l(l+1)(2l+1)}, \end{aligned} \tag{9}$$

$s = 1$, and Ψ is the Ψ function. The Born approximation for the phases $\delta_{l,j}^{\mathrm{c},\mathrm{m}} \approx \tilde{\delta}_{l,j}^{\mathrm{c},\mathrm{m}}$ generates the Born approximation for the amplitudes $M_{nn'} \approx \tilde{M}_{nn'}^{\mathrm{c},\mathrm{m}}$. Since only the following two amplitudes among the five amplitudes $\tilde{M}_{nn'}^{\mathrm{c},\mathrm{m}}$ are nonzero,

$$\begin{aligned} \tilde{M}_{10}^{\mathrm{c},\mathrm{m}} = -[\tilde{M}_{01}^{\mathrm{c},\mathrm{m}}]^* &= \sqrt{2}b_{ls}\exp(-i\varphi) \\ &\times[g(\theta; q) + g(\pi - \theta; q)], \end{aligned} \tag{10}$$

where

$$g(\theta; q) \equiv \sum_{l=1,2,\ldots}\exp[2i\delta_l^{\mathrm{c}}(q)]\tau_l(q)P_l^1(\cos\theta),$$

the cross section given by Eq. (3) for $a = m$ is approximated as

$$d\sigma^{\mathrm{c},\mathrm{m}} \approx d\tilde{\sigma}^{\mathrm{c},\mathrm{m}} \equiv 2\pi|\tilde{M}_{10}^{\mathrm{c},\mathrm{m}}|^2. \tag{11}$$

The leading term of the low-energy asymptotic formula for the auxiliary series g is determined by the method described in detail in [10]. First, we verify that this term is generated by the part of the series g with large values $l \gg \eta$. Then, the Coulomb phases and polynomials in this part are replaced by the leading terms of their asymptotic formulas for $l \longrightarrow \infty$, the resulting series is approximated by the integral with respect to l, and the asymptotic form of the integral is determined by the stationary phase method. The stationary phase point is $l_0 \sim \eta\cot(\theta/2)$. Therefore, the asymptotic behavior of the series g is determined by its terms with large ordinal numbers $l \sim l_0$. Substituting the found asymptotic behavior for g in Eq. (10), we obtain the following asymptotic forms for the amplitudes $\tilde{M}_{10}$ and $\tilde{M}_{01}$:

$$\begin{aligned}\tilde{M}_{10}^{\mathrm{c,\,m}} &= -[\tilde{M}_{01}^{\mathrm{c,\,m}}]^* \sim [i2^{-1/2}\exp(-i\varphi)]b_{ls} \\ &\times \exp[i\omega(\eta)][\alpha(\theta)+\alpha(\pi-\theta)],\end{aligned} \tag{12}$$

where $\omega(\eta) \equiv 2\eta(\ln\eta - 1)$ by definition and

$$\alpha(\theta) \equiv \frac{t(\theta)}{[\sin(\theta/2)]^{2i\eta}}, \quad t(\theta) \equiv \frac{2\cot(\theta/2)+\theta-\pi}{1+\cos\theta}. \tag{13}$$

According to Eqs. (11)–(13), the cross section $d\sigma^{\mathrm{c,\,m}}$ has the low-energy asymptotic behavior

$$\begin{aligned}d\sigma^{\mathrm{c,\,m}} &\approx d\tilde{\sigma}^{\mathrm{c,\,m}} \sim \pi|b_{ls}|^2(|t(\theta)|^2 + |t(\pi-\theta)|^2) \\ &+ 2\pi|b_{ls}|^2\cos\{2\eta\ln[\tan(\theta/2)]\}t(\theta)t(\pi-\theta).\end{aligned} \tag{14}$$

This asymptotic expression oscillates rapidly due to the Mott factor $\cos\{2\eta\ln[\tan(\theta/2)]\}$ and increases unboundedly due to the functions $t(\theta)$ and $t(\pi-\theta)$ as $|\cot(\theta/2)|^2$ and $|\tan(\theta/2)|^2$ for $\theta \longrightarrow 0$ and $\theta \longrightarrow \pi$, respectively. Since the asymptotic behavior of the series g is determined by its terms with $l \sim l_0 \sim \eta\cot(\theta/2)$, the main contribution to the nonzero amplitudes $\tilde{M}_{10}^{\mathrm{c,\,m}}$ and $\tilde{M}_{01}^{\mathrm{c,\,m}}$, as well as to the cross section $d\sigma^{\mathrm{c,\,m}}$ and its approximation $d\tilde{\sigma}^{\mathrm{c,\,m}}$, comes from the *pp* states with large total angular momenta $j \sim l_0$.

Let us analyze Coulomb magnetic–nuclear scattering ($a = ms$). As was shown in [1], to correctly describe the phases $\delta_{l,\,j}^{\mathrm{c,\,ms}}$ for low energies, in addition to the nuclear interaction V^{s}, both magnetic interactions V^{mt} and $V^{\mathrm{m}ls}$ and only the $V^{\mathrm{m}ls}$ interaction should be taken into account if $j < 2$ and otherwise, respectively. For this reason, for $j < 2$, we use the exact phases $\delta_{l,\,j}^{\mathrm{c,\,ms}}$ corresponding to the sum $V^{\mathrm{s}} + V^{\mathrm{mt}} + V^{\mathrm{m}ls}$ and, for $j > 2$, we set $\delta_{l,\,j}^{\mathrm{c,\,ms}} = \delta_{l,\,j}^{\mathrm{c,\,m}} \approx \tilde{\delta}_{l,\,j}^{\mathrm{c,\,m}}$, where $\tilde{\delta}_{l,\,j}^{\mathrm{c,\,m}}$ are approximations (9) for the phases $\delta_{l,\,j}^{\mathrm{c,\,m}}$ corresponding to the interaction $V^{\mathrm{m}ls}$. Therefore, $M^{\mathrm{c,\,ms}}(j > 2) \approx \tilde{M}^{\mathrm{c,\,m}}(j > 2)$ and decompositions (5) are approximated by the sums

$$M_{nn'}^{\mathrm{c,\,ms}} \approx M_{nn'}^{\mathrm{c,\,ms}}(j \le 2) + \tilde{M}_{nn'}^{\mathrm{c,\,m}}(j > 2). \tag{15}$$

As was shown above, $\tilde{M}_{nn'}^{\mathrm{c,\,m}}(j > 2) = 0$ if $|n| = |n'|$, and the main contribution to nonzero series $\tilde{M}_{10}^{\mathrm{c,\,m}}$ and $\tilde{M}_{01}^{\mathrm{c,\,m}}$ comes from the *pp* states with large j values. Therefore, the parts $\tilde{M}_{10}^{\mathrm{c,\,m}}(j > 2)$ and $\tilde{M}_{01}^{\mathrm{c,\,m}}(j > 2)$ of these series have the same low-energy asymptotic behaviors given by Eq. (12). In view of these properties of the amplitudes $\tilde{M}_{nn'}^{\mathrm{c,\,ms}}$, representation (15) corresponds to the following approximation of cross section (3):

$$d\sigma^{\mathrm{c,\,ms}} \approx d\tilde{\sigma}^{\mathrm{c,\,ms}} \equiv d\tilde{\sigma}^{\mathrm{c,\,m}} + d\sigma_{\mathrm{int}} + d\sigma_2^{\mathrm{c,\,ms}}, \tag{16}$$

where $d\sigma_2^{\mathrm{c,\,ms}}$ and $d\tilde{\sigma}^{\mathrm{c,\,m}}$ are the cross sections given by Eqs. (7) and (14), and the interference cross section

$$\begin{aligned}d\sigma_{\mathrm{int}} &\equiv \pi b_{ls}(R/q)[2(\delta_{1,\,2}^{\mathrm{c,\,ms}} - \delta_{1,\,0}^{\mathrm{c,\,ms}}) \\ &+ \sqrt{3}(\delta_{1,\,1}^{\mathrm{c,\,ms}} - \delta_{1,\,2}^{\mathrm{c,\,ms}})]\gamma_{\mathrm{int}}\end{aligned} \tag{17}$$

depends on the scattering angle θ as the function

$$\begin{aligned}\gamma_{\mathrm{int}} &\equiv \sin\{2\eta\ln[\sin(\theta/2)]\}t(\theta)\cos(\theta/2) \\ &+ \sin\{2\eta\ln[\cos(\theta/2)]\}t(\pi-\theta)\sin(\theta/2).\end{aligned} \tag{18}$$

In the limit $q \longrightarrow 0$, the contributions to cross section (16) are

$$\begin{aligned}d\tilde{\sigma}^{\mathrm{c,\,m}} &= O(b_{ls}^2) \neq 0, \quad d\sigma_{\mathrm{int}} = O[b_{ls}(b_t + b_{ls})q^2], \\ d\sigma_2^{\mathrm{c,\,ms}} &= O[(b_t + b_{ls})^2 q^4].\end{aligned} \tag{19}$$

The contribution $d\tilde{\sigma}^{\mathrm{c,\,m}}$ is oscillating and singular at $\theta = 0$ and π, the contribution $d\sigma_{\mathrm{int}}$ is oscillating and regular, and the contribution $d\sigma_2^{\mathrm{c,\,ms}}$ is regular and is not oscillating. Consequently, the cross section $d\sigma^{\mathrm{c,\,ms}}$ has features for low energies: it depends slightly on energy, increases unboundedly in the forward ($\theta = 0$) and backward ($\theta = \pi$) directions, and is a rapidly oscillating function of the angle θ.

The weak energy dependence and unbounded increase of the cross section $d\sigma^{\mathrm{c,\,ms}}$ in the forward direction ($\theta = 0$) as $[\cot(\theta/2)]^2$ are the same features as those for the Schwinger cross section $d\sigma_n \approx \mathrm{const}[\cot(\theta_n/2)]^2$ and are attributed to interactions of the same nature, namely, the interaction of the magnetic moment of one particle with the electromagnetic field of the other particle. For this reason, the effect that is expected in the triplet *pp* scattering and is manifested as these features of the cross section $d\sigma^{\mathrm{c,\,ms}}$ is a Coulomb magnetic *pp* analogue of the Schwinger effect.

Fast oscillations of the cross section $d\sigma^{\mathrm{c,\,ms}}$ as a function of the angle for low energies are the same features as those for the cross section of the Coulomb scattering of two arbitrary identical particles and are caused by the identity and Coulomb interaction of protons. Thus, the second effect that is expected in triplet *pp* scattering and is manifested as such oscillations of the cross section $d\sigma^{\mathrm{c,\,ms}}$ is a Coulomb magnetic *pp* analogue of the Mott effect. The amplitudes of the oscillations are small, because the oscillating contribution to sum (14) is much smaller than its first and second terms for all angles and, according to Eq. (19), the other oscillating term $d\sigma_{\mathrm{int}}$ in the cross section $d\sigma^{\mathrm{c,\,ms}}$ decreases

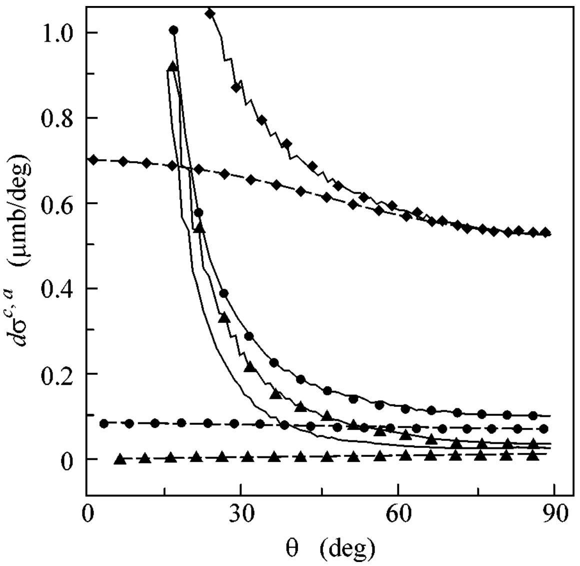

Fig. 1. Cross sections (solid lines with symbols) $d\sigma^{\text{c, ms}}$ and (dashed lines with symbols) $d\sigma^{\text{c, s}}$ for E = (triangles) 50, (circles) 100, and (diamonds) 200 keV and (the line without symbols) the cross section $d\sigma^{\text{c, ms}}$ for E = 10 keV.

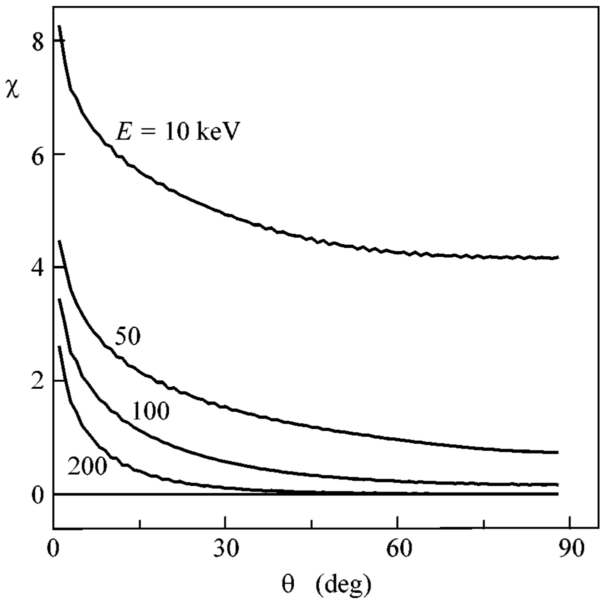

Fig. 2. Function $\chi(d\sigma, \theta)$for various energies E and the thin straight line corresponds to $\chi = 0$.

with energy. Calculation of the cross sections confirms these conclusions.

Let us obtain another approximate formula for the cross section $d\sigma^{\text{c, ms}}$. Formulas (7) and (16)–(18) provide approximate parameterizations $d\sigma^{\text{c, s}} \approx d\sigma_2^{\text{c, s}}$ and $d\sigma^{\text{c, ms}} \approx \tilde{d}\sigma^{\text{c, ms}}$ of the cross sections $d\sigma^{\text{c, s}}$ and $d\sigma^{\text{c, ms}}$ in terms of the phases $\delta_{l,j}^{\text{c, s}}$ and $\delta_{l,j}^{\text{c, ms}}$ with $j \le 2$. Let us replace the phases $\delta_{l,j}^{\text{c, s}}$ and $\delta_{l,j}^{\text{c, ms}}$ in these formulas by, respectively, the approximations $\bar{\delta}_{l,j}^{\text{c, s}}$ and the approximations $\delta_{l,j}^{\text{c, ms}} \approx \bar{\delta}_{l,j}^{\text{c, s}} + \tilde{\delta}_{l,j}^{\text{c, m}}$, where $\bar{\delta}_{l,j}^{\text{c, s}}$ and $\tilde{\delta}_{l,j}^{\text{c, m}}$ are given by Eqs. (8) and (9), which are obtained in [1]. As a result, we arrive at the explicit approximate parameterizations $d\hat{\sigma}^{\text{c, s}}$ and $d\hat{\sigma}^{\text{c, ms}}$ of the cross sections $d\sigma^{\text{c, s}}$ and $d\sigma^{\text{c, ms}}$ in terms of the Coulomb–nuclear scattering lengths $A_{l,j}^{\text{c, s}}$, whose values are the only data on the nuclear interaction that are necessary for calculating the approximation $d\hat{\sigma}^{\text{c, ms}}$. In this sense, the approximation $d\sigma^{\text{c, ms}} \approx d\hat{\sigma}^{\text{c, ms}}$ is independent of the choice of the nuclear interaction.

3. CALCULATION OF THE CROSS SECTIONS

The cross section $d\sigma^{\text{c}, a}$ is calculated for low energies ($E < 10$ MeV) and two cases $a = s$ and ms in the same scheme. The phases $\delta_{l,j}^{\text{c}, a}$ with $a = s$ and ms and $j \le 2$ are calculated using the equations for the phase functions [1]. For $j > 2$, we set $\delta_{l,j}^{\text{c, s}} \equiv 0$ and $\delta_{l,j}^{\text{c, ms}} = \tilde{\delta}_{l,j}^{\text{c, m}}$; i.e., the contribution from the nuclear interaction V^{s} to the phases $\delta_{l,j}^{\text{c, ms}}$ for $j > 2$ is ignored and the contribution $\delta_{l,j}^{\text{c, m}}$ form the magnetic interaction $V^{\text{m}} = V^{\text{m}ls} + V^{\text{mt}}$ is approximated by the sum of the leading terms of their asymptotic formulas (9) that are uniform in l for $q \longrightarrow 0$. As was mentioned in [1], where the pp phases were analyzed, all these approximations are quite appropriate for $E < 10$ MeV. The phases thus obtained are used to calculate the finite parts ($l \le l_{\text{max}} < 20\eta\cot(\theta/2)$) of all series $M_{nn'}^{\text{c}, a}$. Such a choice of l_{max} provides calculation of the cross sections $d\sigma^{\text{c}, a}$ with $a = s$ and ms (shown in Fig. 1) and function $\chi \equiv \log[d\sigma^{\text{c, ms}}/d\sigma^{\text{c, s}}]$ (shown in Fig. 2) with an accuracy to four decimal places. Comparison of the calculated cross section $d\sigma^{\text{c, ms}}$ with its approximations $d\tilde{\sigma}^{\text{c, ms}}$ and $d\hat{\sigma}^{\text{c, ms}}$ shows that the relative accuracy of these approximations for $E < 10$ MeV and $0 < \theta < \pi$ is equal to 10^{-3} and 10^{-2}, respectively.

Figure 1 illustrates a pp analogue of the Schwinger effect that is manifested as an increase in the cross section $d\sigma^{\text{c, ms}}$ in the limit of small scattering angles ($\theta \longrightarrow 0$). For E = 10 keV, the cross section $d\sigma^{\text{c, ms}}$ in the plot scale cannot be distinguished from the cross section $d\tilde{\sigma}^{\text{c, m}}$ given by Eq. (14). Noticeable oscillations in the cross sections $d\sigma^{\text{c, ms}}$ are manifestations of a pp analogue of the Mott effect. As is seen, the cross sections $d\sigma^{\text{c, s}}$ and $d\sigma^{\text{c, ms}}$ differ radically from each other.

As is seen in Fig. 2, the contribution of the magnetic interaction should be included in the calculation of the differential cross section $d\sigma^{c, ms}$, because this contribution for $E \leq 200$ keV significantly exceeds the contribution from the nuclear interaction and the excess increases as the energy or angle θ decreases.

4. CONCLUSIONS

The conclusions are summarized as follows. For energies below 10 MeV, the interaction of the magnetic moment of a proton with the electromagnetic field of the other proton makes a significant contribution to the differential cross section $d\sigma^{c, ms}$ for triplet *pp* scattering that is caused by the sum of the nuclear and magnetic interactions in the Coulomb field of the protons. Owing to the magnetic interaction, the cross section $d\sigma^{c, ms}$ for these energies depends only slightly on the energy for scattering angles $\theta < 30°$ and $\theta > 150°$, has second-order poles in the forward and backward directions (a Coulomb magnetic *pp* analogue of the Schwinger effect), and is a rapidly oscillating function of the scattering angle due to the identity of the protons (a Coulomb magnetic *pp* analogue of the Mott effect). All features of the energy and angular dependences of the cross section $d\sigma^{c, ms}$ for $E < 10$ MeV are reproduced with a relative accuracy of $\sim 10^{-3}$ by derived extrapolation formula (16). A less accurate parameterization $d\hat{\sigma}^{c, ms}$ of the cross section $d\sigma^{c, ms}$ in terms of the Coulomb nuclear scattering lengths $A_{l, j}^{c, s}$ with $j \leq 2$ follows from this formula.

I am grateful to V.B. Belyaev and S.I. Vinitskiĭ for valuable remarks. This work was supported by the Russian Foundation for Basic Research (project no. 04-02-16828).

REFERENCES

1. V. V. Pupyshev, Zh. Éksp. Teor. Fiz. **124**, 1222 (2003) [JETP **97**, 1093 (2003)].
2. V. G. J. Stoks and J. J. de Swart, Phys. Rev. C **42**, 1235 (1990).
3. R. V. Reid, Jr., Ann. Phys. (N.Y.) **50**, 411 (1968).
4. N. F. Mott, Proc. R. Soc. London, Ser. A **124**, 425 (1929).
5. J. Schwinger, Phys. Rev. **73**, 407 (1948).
6. J. R. Taylor, *Scattering Theory: The Quantum Theory of Nonrelativistic Colluions* (Wiley, New York, 1972; Mir, Moscow, 1975).
7. N. A. Blasov, *Neutrons* (Nauka, Moscow, 1971) [in Russian].
8. H. P. Stapp, T. J. Ypsilantis, and M. Metropolis, Phys. Rev. **105**, 302 (1957).
9. R. O. Berger and L. Spruch, Phys. Rev. **138**, B1106 (1965).
10. A. A. Kvitsinskiĭ, Teor. Mat. Fiz. **65**, 226 (1985).

Translated by R. Tyapaev

JETP Letters, Vol. 82, No. 5, 2005, pp. 248–252. From Pis'ma v Zhurnal Éksperimental'noĭ i Teoreticheskoĭ Fiziki, Vol. 82, No. 5, 2005, pp. 279–283.
Original English Text Copyright © 2005 by Schützhold, Mostame.

Quantum Simulator for the *O*(3) Nonlinear Sigma Model¶

R. Schützhold and S. Mostame
Institut für Theoretische Physik, Technische Universität Dresden, D-01062 Dresden, Germany
e-mail: schuetz@theory.phy.tu-dresden.de; sarah@theory.phy.tu-dresden.de

Received July 11, 2005

We propose a design for the construction of a laboratory system based on present-day technology which reproduces and thereby simulates the quantum dynamics of the *O*(3) nonlinear sigma model. Apart from its relevance in condensed-matter theory, this strongly interacting quantum field theory serves as an important toy model for quantum chromodynamics (QCD) since it reproduces many crucial properties of QCD. The proposed design is therefore a feasibility and proof-of-principle study for more general analogue quantum simulators. © *2005 Pleiades Publishing, Inc.*

PACS numbers: 03.67.–a, 11.10.Kk, 68.65.–k

INTRODUCTION

In many areas of physics, progress has been thwarted by our lack of understanding of strongly interacting quantum systems with many degrees of freedom, such as quantum field theories. Beyond perturbation theory with respect to some parameter or semiclassical models/methods, there are not many analytical tools available for the treatment of these systems. Numerical methods are hampered by the exponentially increasing amount of resources required for the simulation of quantum systems with many degrees of freedom in general. However, this obstacle applies to classical computers only—quantum computers will be able to simulate other quantum systems with polynomial effort [1]. But as long as universal quantum computers of sufficient size (e.g., number of QuBits) are not available, one has to search for alternatives. One possibility is to design a special quantum system in the laboratory, which reproduces the Hamiltonian of a particular quantum field theory of interest [2]. This designed quantum system can then be regarded as a special quantum computer (instead of a universal one), which just performs the desired quantum simulation. In this Letter, we propose such a quantum simulator for the example of the *O*(3) nonlinear sigma model and demonstrate that it can (in principle) be constructed using present-day technology, cf. [2, 3].

The model. The 1 + 1 dimensional σ model [4–10] is described by the *O*(*N*) and Poincaré invariant action

$$\mathscr{L} = \frac{\hbar}{2c}\partial_\nu\boldsymbol{\sigma}\cdot\partial^\nu\boldsymbol{\sigma} = \frac{\hbar}{2c}[(\partial_t\boldsymbol{\sigma})^2 - c^2(\partial_x\boldsymbol{\sigma})^2], \qquad (1)$$

with the internal vector $\boldsymbol{\sigma} = (\sigma_1, \sigma_2, \ldots, \sigma_N) \in \mathbb{R}^N$ reflecting the *O*(*N*)-symmetry. So far, this theory describes *N* independent free fields, but the constraint

$$\boldsymbol{\sigma}^2 = \sigma_1^2 + \sigma_2^2 + \ldots + \sigma_N^2 = N/g^2, \qquad (2)$$

introduces an interaction corresponding to the coupling $g > 0$. For vanishing coupling $g \downarrow 0$, the curvature of the constraint sphere ($\boldsymbol{\sigma}^2 = N/g^2$) vanishes and we reproduce (locally) an effectively free theory. For finite coupling $g > 0$, we obtain a nontrivially interacting theory as long as $N \geq 3$, i.e., in the non-Abelian case. The classical ground state $\boldsymbol{\sigma}$ = const is *O*(*N*)-degenerate, but quantum interaction lifts that degeneracy and gives the classical Goldstone modes a mass gap; see, e.g., [7, 8].

Properties. Apart from its relevance in condensed-matter theory (partly due to its relation to spin systems such as antiferromagnets; see, e.g., [11]), it can be shown that the 1 + 1 dimensional *O*(*N*) σ model reproduces many crucial properties of quantum chromodynamics (QCD) and hence serves as an important toy model; see, e.g., [7]. The σ model is renormalizable (in 1 + 1 dimensions; cf. [10]) and its running coupling $g(p^2)$ generates asymptotic freedom $g^2(p^2 \gg \Lambda^2) \propto 1/\ln(p^2/\Lambda^2)$, cf. [5]. In analogy to QCD, the classical scale invariance $x^\nu \longrightarrow \Omega x^\nu$ is broken dynamically, corresponding to the dimensional transmutation $g \longrightarrow \Lambda$. Furthermore, the σ model generates nonvanishing vacuum condensates such as $\langle\hat{\mathscr{L}}\rangle \neq 0$ in the operator product expansion and reproduces the trace anomaly $\langle\hat{T}_\nu^\nu\rangle \neq 0$ (see, e.g., [7]). It also serves as a toy model for the study of the low-energy theorems and sum rules (see, e.g., [7]). Finally, for $N = 3$, the σ model exhibits instantons (mapping of $\mathbb{S}_2$ onto $\mathbb{R}^2$, cf. [6, 7]) and θ vacua.

The analogue. In order to reproduce the quantum dynamics of the 1 + 1 dimensional *O*(*N*) σ model according to Eqs. (1) and (2), let us consider a large number of perfectly insulating thin hollow spheres (radius ρ) lined up at equal distances Δ*x* with single

---

¶ The text was submitted by the authors in English.

0021-3640/05/8205-0248$26.00 © 2005 Pleiades Publishing, Inc.

electrons being captured by the polarizability (inducing a finite extraction energy) on each of the hollow spheres. These insulating spheres are surrounded by an arrangement of superconducting spheres (radius α) and wires (radius δ) as depicted in figure, which generate controlled interactions of the confined electrons via their image charges. The involved length scales including the typical wavelength of the excitations λ, the distance of elements (lattice spacing) Δx, the distance between the insulating and the conducting spheres γ, the radii of the insulating and conducting spheres (ρ and α) and wires δ (cf. figure) are supposed to obey the following hierarchy

$$\lambda \gg \Delta x \gg \gamma \gg \rho \sim \alpha \gg \delta. \qquad (3)$$

The total Lagrangian for the system of electrons reads

$$\mathscr{L} = \sum_i \left[\frac{m}{2}\dot{\mathbf{r}}_i^2 - V(\mathbf{r}_{i+1}, \mathbf{r}_i)\right], \qquad (4)$$

with m being the mass of the electrons and $V(\mathbf{r}_{i+1}, \mathbf{r}_i)$ their interaction potential, where only nearest neighbors are taken into account in view of the assumptions (3). In this limit, the interaction potential induced by the images of the electron charges e simplifies to

$$V(\mathbf{r}_{i+1}, \mathbf{r}_i) = \frac{e^2\alpha^2}{4\pi\varepsilon_0\gamma^4}\frac{(\mathbf{r}_{i+1}-\mathbf{r}_i)^2}{4\alpha + \Delta x/\ln(\Delta x/\delta)}, \qquad (5)$$

where the first addend in the denominator on the right-hand side is due to the capacitance of the conducting spheres $4\pi\varepsilon_0\alpha$ and the second one due to the capacitance of the long wires $2\pi\varepsilon_0\Delta x/\ln(\Delta x/\delta)$. Comparing the resulting Lagrangian in Eqs. (4) and (5) with the one in Eq. (1), we can read off the effective propagation speed

$$c_{\text{eff}} = c_0\sqrt{\frac{e^2}{4\pi\varepsilon_0 m c_0^2}\frac{2\alpha^2\Delta x^2/\gamma^4}{4\alpha + \Delta x/\ln(\Delta x/\delta)}}. \qquad (6)$$

Since the first term under the root represents the classical electron radius (of order 10^{-15} m), the effective propagation speed c_{eff} is much smaller than the speed of light in vacuum $c_0 \gg c_{\text{eff}}$ for realistic parameters (see below), i.e., we obtain a large slow-down. Furthermore, we may identify the effective coupling for $N = 3$

$$g_{\text{eff}} = \sqrt{3}\frac{\gamma}{\rho}\sqrt[4]{\frac{4\pi\varepsilon_0\hbar^2}{me^2}\frac{4\alpha + \Delta x/\ln(\Delta x/\delta)}{2\alpha^2}}, \qquad (7)$$

where the first term under the root is the classical electron radius over the square of the fine structure constant. The value of the effective coupling can be tuned by varying the ratio $\gamma/\rho \gg 1$ and may well be of order one (see parameters below). Strictly speaking, the above equation determines the value of the running coupling $g_{\text{eff}}(p^2)$ at a length scale corresponding to the lattice spacing Δx (lattice renormalization scheme). In complete analogy to Λ_{QCD}, the coupling $g_{\text{eff}}^2(p^2 \gg \Lambda_\sigma^2) \propto 1/\ln(p^2/\Lambda_\sigma^2)$ determines the induced scale of dynamical symmetry breakdown Λ_σ of the σ model (dimensional transmutation). This important quantity sets all other length scales such as the mass gap (see, e.g., [8]) and must satisfy the condition (3) for consistency, i.e., $\Lambda_\sigma\Delta x \ll 1$. Finally, identifying (again for $N = 3$)

$$\boldsymbol{\sigma}(x = i\Delta x) = \frac{\sqrt{3}}{g_{\text{eff}}}\frac{\mathbf{r}_i}{\rho}, \qquad (8)$$

the continuum limit ($\sum_i \Delta x \longrightarrow \int dx$ for $\lambda \gg \Delta x$) of Eq. (4) generates the Lagrangian (1) of the $O(3)$ nonlinear sigma model with the constraint (2) being implemented by $\mathbf{r}_i^2 = \rho^2$.

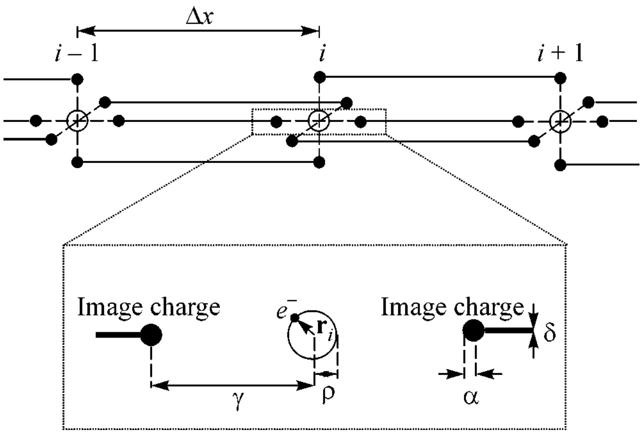

Sketch of the proposed analogue quantum simulator. The solid lines and spheres denote (super) conductors and the hollow spheres are insulators containing single electrons. Shown are just three elements of a long chain (top) and a close-up view (bottom) with the involved length scales.

Disturbances. Of course, for a realistic proposal, it is essential to estimate the impact of the contributions, which have been omitted so far. The additional kinetic terms due to inductances L of the wires are negligible $LI^2 \ll m\dot{\mathbf{r}}^2$ provided that

$$4\frac{\alpha}{\Delta x}\left(\frac{c_{\text{eff}}}{c_0}\right)^2\ln\left(\frac{\Delta x}{\delta}\right) \ll 1 \qquad (9)$$

holds, i.e., for a sufficiently large slow-down (as one would expect). For the same reason, the influence of the zero-point fluctuations of the electromagnetic field (inductance of free space) is negligible.

In contrast to sequential quantum algorithms, where errors may accumulate over many operations, the quantum simulation under consideration is basically a ground state problem and hence more similar to adiabatic quantum computing [12]. In this case, decoherence can be neglected as long as the interaction energies of the disturbances are much smaller than the energy gap between the ground state and the first excited state [12]. For the nonlinear σ model, this gap is determined by the induced scale Λ_σ (in analogy to QCD). Therefore, the energies of all perturbations (e.g., impurities in the material) must be much smaller than the gap of order $\hbar c_{\text{eff}}\Lambda_\sigma$. In particular, in order to see quantum behavior (where the Heisenberg uncertainty relation becomes important), the temperature must be small enough:

$$k_B T \ll \hbar c_{\text{eff}} \Lambda_\sigma. \tag{10}$$

Another issue concerns the spins of the electrons, which have been omitted so far. Fortunately, we may fix the electron spins by a small external magnetic field (see the next paragraph) and the various spin–spin and especially spin–orbit coupling terms are negligible (in comparison to $\hbar c_{\text{eff}}\Lambda_\sigma$) for the parameters provided below.

Phase diagram. Before investigating the impact of an external magnetic field, let us turn to the phase diagram of the nonlinear σ model in terms of the temperature T and the chemical potential μ. For low temperatures $k_B T \ll \hbar c_{\text{eff}}\Lambda_\sigma$ and small chemical potentials $\mu \ll \hbar c_{\text{eff}}\Lambda_\sigma$, we basically get the usual vacuum state. Note that the introduction of a chemical potential necessitates the definition of a particle number (which is a nontrivial issue in interacting theories). In the σ model, this can be achieved by means of the Noether current corresponding to the global $O(3)$ invariance $\mathbf{j}_\nu = \boldsymbol{\sigma} \times \partial_\nu \boldsymbol{\sigma}$ and the associated global charge along some internal axis $\mathbf{n}$ with $\mathbf{n}^2 = 1$

$$Q = \frac{1}{c_{\text{eff}}} \mathbf{n} \cdot \int dx \boldsymbol{\sigma} \times \dot{\boldsymbol{\sigma}}. \tag{11}$$

For the laboratory system, the Noether charge Q is just the total (orbital) angular momentum in units of $\hbar$. Note that still many charges $Q \gg 1$ are required to generate one magnetic flux quantum (due to $c_0 \gg c_{\text{eff}}$).

In terms of the chemical potential defined with respect to this (dimensionless) Noether charge, the grand-canonical Hamiltonian $\hat{H}_{\text{gc}}$ reads

$$\hat{H}_{\text{gc}} = \hat{H}_0 + \mu_N \hat{N} = \hat{H}_0 + \mu_Q \hat{Q}. \tag{12}$$

Translating this expression back to our laboratory system in Eq. (4), we observe that the chemical potential exactly corresponds to an external magnetic field $\mathbf{B}$ inducing the additional term $\dot{\mathbf{r}} \cdot \mathbf{A} = \dot{\mathbf{r}} \cdot (\mathbf{r} \times \mathbf{B})/3 = \mathbf{B} \cdot (\dot{\mathbf{r}} \times \mathbf{r})/3$

$$\mu_{\text{eff}} = \frac{e\hbar}{3m} B. \tag{13}$$

(The second-order term $e^2\mathbf{A}^2/m$ is three orders of magnitude smaller for the parameters given below and can be neglected.) When the effective chemical potential μ_{eff} exceeds the energy gap of order $\hbar c_{\text{eff}}\Lambda_\sigma$, the structure of the ground state changes, and the above Noether current $\mathbf{j}_\nu$ acquires a nonvanishing expectation value (quantum phase transition, see, e.g., [8]). At the critical field $B_{\text{crit}} = \mathcal{O}(m c_{\text{eff}}\Lambda_\sigma/e)$ where this quantum phase transition occurs, the energy of the electron spins is of the same order as the gap $\boldsymbol{\mu}_s \cdot \mathbf{B} = \mathcal{O}(\hbar c_{\text{eff}}\Lambda_\sigma)$ and thus much bigger than the temperature. Hence one can fix the electron spins with much smaller external magnetic fields $B \ll B_{\text{crit}}$ without disturbing the vacuum state too much. On the other hand, it is also possible to explore the full phase diagram (e.g., cross the quantum phase transition, monitored by a SQUID) by increasing the external magnetic field, which is completely equivalent to changing the chemical potential (and hence the number of particles). For the set of parameters discussed below, the critical field B_{crit} is on the order of milli-Tesla.

Experimental parameters. The aforementioned constraints, in particular Eqs. (3) and (10), provide the frame of a window of opportunity for the experimental realization of the proposed quantum simulator, which is (fortunately) open to present-day technology. Let us first explore the limit set by the ultra-low temperatures. For solid bodies of reasonable size, one can reach temperatures on the order of 10 μK by electron gas cooling via spin relaxation. If we choose our parameters according to $\delta = 100$ nm, $\rho = 400$ nm, $\alpha = 500$ nm, $\gamma = 2.5$ μm, and $\Delta x = 12.5$ μm, we obtain $g_{\text{eff}} = \mathcal{O}(1)$, $c_{\text{eff}} \approx 10^4$ m/s, $\Lambda_\sigma^{-1} \approx 125$ μm, and $\hbar c_{\text{eff}}\Lambda_\sigma$ corresponds to 600 μK, which satisfies all of the above assumptions reasonably well. Alternatively, we may start from the present state of nano-technology, which facilitates the production of nano-wires with a radius of order nanometer. If we explore this limit and choose $\delta = 1$ nm, $\rho = 12$ nm, $\alpha = 5$ nm, $\gamma = 25$ nm, and $\Delta x = 125$ nm, we obtain a similar value for g_{eff} and $c_{\text{eff}} \approx 10^5$ m/s, but now $\hbar c_{\text{eff}}\Lambda_\sigma$ corresponds to a temperature of order Kelvin. The range between μK and fractions of a Kelvin as well as between nanometres and micrometers provides a two or three orders of magnitude wide window of opportunity and the optimum experimental parameters are probably somewhere in the middle.

The thin (super) conducting wires can be switched on and off by local variations of the temperature (below and above the critical value). If the interaction $V(\mathbf{r}_{i+1}, \mathbf{r}_i)$ is switched off, the energy spectrum of the electrons is determined by the usual spherical harmonics

$$E_l = \frac{\hbar^2}{2m} \frac{l(l+1)}{\rho^2}. \tag{14}$$

The energy gap between the s state ($l = 0$) and p state ($l = 1$), i.e., without interaction $V(\mathbf{r}_{i+1}, \mathbf{r}_i)$, is one order of magnitude larger than with interaction $\hbar c_{\text{eff}}\Lambda_\sigma$. Consistently, the interaction potential $V(\mathbf{r}_{i+1}, \mathbf{r}_i)$ between the electrons on different spheres is of the same order of magnitude as the gap between the *s* state ($l = 0$) and *p* state ($l = 1$) on a single sphere leading to strong entanglement of the ground state. If we want to switch on the interaction $V(\mathbf{r}_{i+1}, \mathbf{r}_i)$ adiabatically (e.g., via changing the temperature of the wires) satisfying the condition for the adiabatic theorem $|\langle\psi_0|d\hat{H}(t)/dt|\psi_1\rangle|/(\Delta E_{01})^2 \ll 1$ in order to stay in the ground state $|\psi_0\rangle$, the typical adiabatic switching time should be longer than a few picoseconds. Finally, for the parameters discussed above, the various spin–spin and spin–orbit coupling energies are at least two orders of magnitude smaller than $\hbar c_{\text{eff}}\Lambda_\sigma$.

SUMMARY

As we have demonstrated above, it is (in principle) possible to construct a quantum simulator for the *O*(3) nonlinear σ model with present-day technology. Such a restricted quantum computer would allow the comparison, for a controllable scenario, between perturbative and nonperturbative analytical methods (renormalization flow [5, 10, 11], instantons [6], operator product expansion and vacuum condensates, low-energy theorems and sum rules [7], the S-matrix [8], etc.), as well as numerical results [9] on the one hand with real quantum simulations on the other hand. In contrast to most numerical simulations, for example, the proposed quantum simulator works in real (laboratory) time; i.e., it is not necessary to perform a Wick rotation to Euclidean time. This advantage facilitates the study of the evolution of excitations, for example collisions (S-matrix).

Furthermore, the proposed setup allows direct access to the quantum state and hence an investigation of the strong entanglement (e.g., in the ground state or near the quantum phase transition). This could be done via state-selective radio/micro-wave spectroscopy of transitions from the levels in Eq. (14) to some higher lying empty and isolated internal level (of the semiconductor) with a sharp energy, for example (fluorescence measurement). Generating the radio/microwaves via a circuit (waveguide) facilitates the position control of the measurement (vicinity of the inductance loop). Furthermore, one may also switch off the wires (e.g., by locally increasing the temperature) before the measurement.

It is also possible to create particles (and their antiparticles), which can be used to study the S-matrix, for example, via the illumination with (left and right) circular polarized radio/micro-wave radiation; cf. Eq. (11) and the subsequent remarks. Another interesting point is the robustness or fragility of nonperturbative properties (such as the instanton density) with respect to a small coupling to external degrees of freedom.

Apart from above points of interest, the construction of such a restricted quantum computer, which is especially dedicated to the simulation of the *O*(3) nonlinear σ model, would be an interesting feasibility study for more general quantum simulators for a comparably well understood (yet nontrivial) system. Finally, experience shows that the availability of a new tool (such as the proposed quantum simulator) yielding new tests and results usually leads us to a new level of understanding in physics with possibly unexpected outcomes.

Outlook. After having handled and understood the 1 + 1 dimensional situation, the extension to 2 + 1 dimensions should not be very problematic. The 2 + 1 dimensional *O*(3) nonlinear σ model loses some of the properties discussed above, but also acquires novel features, such as skyrmions which are described by the topological current $j^\rho = \epsilon^{\mu\nu\rho}\boldsymbol{\sigma}\cdot(\partial_\mu\boldsymbol{\sigma}\times\partial_\nu\boldsymbol{\sigma})$. The inclusion of an explicit *O*(3)-symmetry-breaking term $\mathbf{n}\cdot\boldsymbol{\sigma}$ should be easy in 1 + 1 and 2 + 1 dimensions. Note that we did not incorporate a topological (Chern-Simons type) θ-term $\mathcal{L}_\theta = \theta\epsilon^{\mu\nu}\boldsymbol{\sigma}\cdot(\partial_\mu\boldsymbol{\sigma}\times\partial_\nu\boldsymbol{\sigma})$ in our 1 + 1 dimensional scenario (in analogy to the θ term $G^*_{\mu\nu}G^{\mu\nu}$ in QCD), whose implementation is less straightforward. Further interesting topics are the behavior of strongly interacting quantum field theories (such as QCD and the σ model) during the cosmic expansion and the (long-range) entanglement of the nonperturbative vacuum state (which might be used as a tool for diagnosis and a resource).

R.S. gratefully acknowledges fruitful discussions with I. Affleck, B. Barbara, W. Hardy, M. Krusius, P. Stamp, G.'t Hooft, B. Unruh, G. Volovik, and E. Zhitnitsky, as well as support by the Humboldt foundation, the COSLAB Programme of the ESF, the Pacific Institute of Theoretical Physics, CIAR, and NSERC. This work was supported by the Emmy-Noether Programme of the German Research Foundation (DFG) under grant no. SCHU 1557/1-1.

REFERENCES

1. R. P. Feynman, Int. J. Theor. Phys. **21**, 467 (1982); S. Lloyd, Science **273**, 1073 (1996); S. Somaroo *et al.*, Phys. Rev. Lett. **82**, 5381 (1999).
2. D. Porras and J. I. Cirac, Phys. Rev. Lett. **92**, 207901 (2004); J. J. Garcia-Ripoll, M. A. Martin-Delgado, and J. I. Cirac, Phys. Rev. Lett. **93**, 250405 (2004).
3. M. V. Feigel'man *et al.*, Phys. Rev. B **70**, 224524 (2004).
4. M. Gell-Mann and M. Levy, Nuovo Cimento **16**, 705 (1960).
5. A. M. Polyakov, Phys. Lett. B **59**, 79 (1975).
6. A. M. Polyakov and A. A. Belavin, Pis'ma Zh. Éksp. Teor. Fiz. **22**, 503 (1975) [JETP Lett. **22**, 245 (1975)]; A. A. Belavin *et al.*, Phys. Lett. B **59**, 85 (1975); V. A. Fateev, I. V. Frolov, and A. S. Schwarz, Nucl. Phys. B **154**, 1 (1979).
7. V. A. Novikov *et al.*, Phys. Rep. **116**, 103 (1984); Fiz. Élem. Chastits At. Yadra **17**, 472 (1986) [Sov. J. Part. Nucl. **17**, 204 (1986)].

8. M. Luscher, Nucl. Phys. B **135**, 1 (1978); M. Luscher and K. Pohlmeyer, Nucl. Phys. B **137**, 46 (1978); Alexander B. Zamolodchikov and Alexey B. Zamolodchikov, Ann. Phys. **120**, 253 (1979); A. M. Polyakov and P. B. Wiegmann, Phys. Lett. B **131**, 121 (1983); P. B. Wiegmann, Phys. Lett. B **152**, 209 (1985); P. Hasenfratz, M. Maggiore, and F. Niedermayer, Phys. Lett. B **245**, 522 (1990).
9. G. Martinelli, G. Parisi, and R. Petronzio, Phys. Lett. B **100B**, 485 (1981); K. Symanzik, Nucl. Phys. B **226**, 205 (1983); Y. Iwasaki, Nucl. Phys. B **258**, 141 (1985); U. Wolff, Nucl. Phys. B **334**, 581 (1990).
10. E. Brezin, J. Zinn-Justin, and J. C. Le Guillou, Phys. Rev. D **14**, 2615 (1976); E. Brezin and J. Zinn-Justin, Phys. Rev. Lett. **36**, 691 (1976); W. A. Bardeen, B. W. Lee, and R. E. Shrock, Phys. Rev. D **14**, 985 (1976); S. Hikami and E. Brezin, J. Phys. A **11**, 1141 (1978).
11. A. M. Tsvelik, *Quantum Field Theory in Condensed Matter Physics* (Cambridge Univ. Press, Cambridge, 1995); P. Chaikin and T. C. Lubenski, *Principles of Condensed Matter Physics* (Cambridge Univ. Press, Cambridge, 1995); J. Zinn-Justin, Int. Ser. Monogr. Phys. **113**, 1 (2002).
12. E. Farhi *et al.*, Science **292**, 472 (2001); A. M. Childs, E. Farhi, and J. Preskill, Phys. Rev. A **65**, 012322 (2002).

JETP Letters, Vol. 82, No. 5, 2005, pp. 253–258. Translated from Pis'ma v Zhurnal Éksperimental'noĭ i Teoreticheskoĭ Fiziki, Vol. 82, No. 5, 2005, pp. 284–289.
Original Russian Text Copyright © 2005 by Mantsyzov.

Optical Zoomeron as a Result of Beatings of the Internal Modes of a Bragg Soliton

B. I. Mantsyzov

Faculty of Physics, Moscow State University, Vorob'evy gory, Moscow, 119992 Russia
e-mail: mants@genphys.phys.msu.ru

Received June 22, 2005; in final form, July 12, 2005

A new solution of two-wave Maxwell–Bloch equations has been obtained analytically and numerically. It describes the propagation of an oscillating nonlinear optical solitary wave, or optical zoomeron, in a one-dimensional periodic resonant Bragg structure. It has been shown that the appearance of large oscillations in the velocity and total amplitude of Bloch modes of the pulse is caused by beating of internal modes of the perturbed Bragg soliton. *© 2005 Pleiades Publishing, Inc.*

PACS numbers: 42.25.Fx, 42.50.Md, 42.65.Tg, 42.70.Qs

Investigations of the dynamics of nonlinear wave processes involving solitary nonlinear waves, or solitons, are continuously attracting great interest in various areas of natural sciences and engineering [1]. First of all, this interest is associated with the rich variety of nonlinear dynamic systems in nature whose evolution is to a high extent determined by the unique properties of solitons, namely, the conservation of the shape and velocity during propagation and after interaction. Strictly speaking, such properties are characteristic only of solutions of completely integrable nonlinear dynamic equations such as the sine-Gordon equation, Maxwell–Bloch equations, and nonlinear Schrödinger equation, which appear as a result of the use of certain approximations when solving a number of physical problems. Using the inverse-scattering method, one can mathematically construct an infinite number of completely integrable equations including those that, being taken with various initial conditions, can have both traditional soliton solutions and qualitatively new solutions called zoomerons [2]. A zoomeron is stable when propagating and interacting, as is typical for a soliton, but it exhibits new dynamics such that its amplitude and velocity oscillate considerably during motion, and a change not only in the magnitude but also in the sign of the velocity of the pulse is possible. For this reason, the appearance of zoomeronlike equations in actual physical problems would provide rich possibilities for studying new dynamic laws for nonlinear systems and would allow the generalization of various results concerning soliton dynamics to the case of oscillating pulses. Unfortunately, a physical phenomenon that is described by the completely integrable zoomeron equation has not yet found. At the same time, it is known [3] that a change in the magnitude of the velocity of solitonlike solutions in equations close to being completely integrable is possible, for example, in the trapping of the soliton by a perturbation, when oscillations with zero average velocity arise near the perturbation, as well as in the inelastic collision of pulses that is accompanied by the single excitation and absorption of the internal mode of the soliton [4]. Long-lived oscillations of the soliton amplitude are also possible when the internal mode is excited at nonzero frequency [5], but the velocity of the soliton is conserved or changes insignificantly in this case. The Bragg solitons of incompletely integrable Maxwell–Bloch equations [6] and nonlinear Schrödinger equations for coupled modes [7] are characterized by dynamic multistability, when, under certain initial conditions, oscillations arise in the velocity of the pulse with a characteristic change of the sign of the velocity, but only for zero average value. Numerical simulation of the dynamics of Bragg solitons in a resonantly absorbed lattice in the case of small detuning from the exact Bragg condition reveals strong oscillations of the amplitudes of Bloch waves and velocity of the Bragg soliton propagating with nonzero average velocity [8]. However, the physical cause of the appearance of such pulse dynamics is not yet understood.

In this work, the problem concerning the excitation of the internal mode in the standing Bragg soliton of the self-induced transparency with perturbed envelops of direct and inverse Bloch waves is solved. It is shown that two internal modes close in shape can be simultaneously excited at low and zero frequencies. As a result of beatings of these modes, a periodic energy exchange arises between the internal-mode fields and the resonant subsystem of two-level atoms in the Bragg soliton, which results in the appearance of oscillations in the inversion of excited atoms in the Bragg soliton. The solution is generalized to the case of a slowly moving soliton. Such a soliton is already perturbed due not only to the profile deformation but also to inversion oscillations accompanying the internal-mode beatings, which results in strong oscillations of the amplitude, polarization, inversion, and velocity of the pulse. Such dynamics of a solitary wave is characteristic of a zoomeron. The parameters of the solutions obtained by direct numerical integration of the two-wave Maxwell–Bloch equations agree well with the proposed analytical solution for the optical zoomeronlike pulse. The time dependence of the zoomeron velocity is obtained using the energy integral.

The problem concerning the coherent interaction of laser radiation with a one-dimensional resonant Bragg structure of periodically located thin layers containing two-level oscillators is described by two-wave Maxwell–Bloch equations [9] for the slow complex amplitudes of the electric field $E^{\pm}$ of the direct and inverse Bloch waves, average atomic dipole moment P normalized to the transition dipole moment, and inversion n:

$$\Omega_t + \tilde{\Omega}_x = 2P, \quad \tilde{\Omega}_t + \Omega_x = 0, \tag{1.1}$$

$$P_t = n\Omega, \quad n_t = -\frac{1}{2}(P^*\Omega + P\Omega^*). \tag{1.2}$$

Here, $\Omega = \Omega^+ + \Omega^-$; $\tilde{\Omega} = \Omega^+ - \Omega^-$; $\Omega^{\pm} = (2\tau_c\mu/\hbar)E^{\pm}$; τ_c is the cooperative time; μ is the matrix element of the transition density matrix; $x = x'/c\tau_c$ and $t = t'/\tau_c$ are dimensionless variables, where x' and t' are the space coordinate and time, respectively, and c is the speed of light; and the subscripts x and t stand for the respective partial derivatives. Equations (1) are written under the exact Bragg condition and for the identical frequencies of radiation and resonance transition of oscillators.

We first obtain an expression for the internal mode of the perturbed Bragg soliton with zero propagation velocity and then generalize the solutions to the case of a slowly moving soliton.

Equations (1) have the following integrals of motion corresponding to the conservation of the total energy W and topological charge Q of the localized $\Omega(x = +\infty; t) = 0$ solution:

$$W = \int_{-\infty}^{\infty} \frac{1}{4}\Omega\Omega^* + \frac{1}{4}\tilde{\Omega}\tilde{\Omega}^* + (1+n)dx, \qquad Q = \int_{-\infty}^{\infty} \tilde{\Omega}dx. \tag{2}$$

We seek the solution in the form of the linear superposition of the deformed standing soliton solution of Eqs. (1), Ω_s, $\tilde{\Omega}_s$, and small perturbation $\delta\Omega$, $\delta\tilde{\Omega}$ satisfying the second of Eqs. (1.1):

$$\Omega(x, t) = \Omega_s(x) + \delta\Omega, \quad \tilde{\Omega}(x, t) = \tilde{\Omega}_s(x) + \delta\tilde{\Omega}. \tag{3}$$

Here,

$$\delta\Omega = i\varepsilon f_t(t)\varphi(x), \qquad \delta\tilde{\Omega} = -i\varepsilon[f(t)\varphi_x(x) + \varphi_{1x}(x)]; \tag{4}$$

soliton components have the form $\Omega_s(x) = 0$ and $\tilde{\Omega}_s(x) = (4/\beta)\operatorname{sech}(\beta x)$, where $\beta \equiv \sqrt{2-\alpha}$ and α is the parameter of the soliton profile deformation such that $\alpha = 0$ corresponds to the exact soliton solution; ε is a small real parameter; and $f(t)$ and $\varphi(t)$ are real functions. The choice of perturbation $\delta\Omega$, $\delta\tilde{\Omega}$ in the form of imaginary additions (a phase shift of $\pi/2$ with respect to the soliton solution is generally necessary) ensures the elimination of cross terms $\int_{-\infty}^{\infty} dx(\delta\Omega\Omega_s^* + \delta\tilde{\Omega}\tilde{\Omega}_s^* + \text{c.c.}) = 0$ in the energy integral given in Eqs. (2). Thus, we exclude the interaction of the field components of the soliton with the internal mode but retain the possibility of the interaction of the internal mode with resonant oscillators. This interaction is described by Bloch equations (1.2), which have the following solutions for fields (3) and (4):

$$P(x, t) = -2\operatorname{sech}\beta x \tanh\beta x + i(-1 + 2\operatorname{sech}^2\beta x)\sin[\varepsilon(f\varphi + b\varphi_1)], \tag{5}$$

$$n(x, t) = (-1 + 2\operatorname{sech}^2\beta x)\cos[\varepsilon(f\varphi + b\varphi_1)],$$

where b is the integration constant determined from the initial conditions. Substituting Eqs. (3)–(5) into initial equations (1.1) and linearizing under the conditions ε, ω, $\alpha \ll 1$, we arrive at the expressions

$$f(t) = f_0\cos(\omega t + \phi_0), \quad \varphi_1(x) = \varphi_0\operatorname{sech}\beta x, \tag{6}$$

if $b = 1 - \alpha/2$. Here, ϕ_0 is the initial phase and the function amplitudes f_0 and φ_0 satisfy the conditions εf_0, $\varepsilon\varphi_0 \ll 1$. In what follows, $f_0 = 1$. The corresponding equation for the function $\varphi(x)$ has the form

$$\beta^{-2}\varphi_{xx} + \left[-1 + \frac{\omega^2 - \alpha}{2} + (2+\alpha)\operatorname{sech}^2\beta x\right]\varphi = 0. \tag{7}$$

Using perturbation theory, it is easy to show that the eigenvalue problem specified by Eq. (7) has the finite localized solution

$$\varphi(x) = \operatorname{sech}\beta x - \frac{\alpha}{3}(1 + \ln\cosh\beta x)\operatorname{sech}\beta x, \tag{8}$$

if

$$\omega^2 = -\alpha/3. \tag{9}$$

Substituting Eqs. (6) and (8) into Eq. (4) and omitting the $\varepsilon\omega^2$ terms, we obtain the following expressions for the found internal modes:

$$\delta\Omega = -i\varepsilon\omega\sin\omega t\operatorname{sech}\beta x, \qquad \delta\tilde{\Omega} = i\varepsilon\beta(\cos\omega t + \varphi_0)\operatorname{sech}\beta x\tanh\beta x. \tag{10}$$

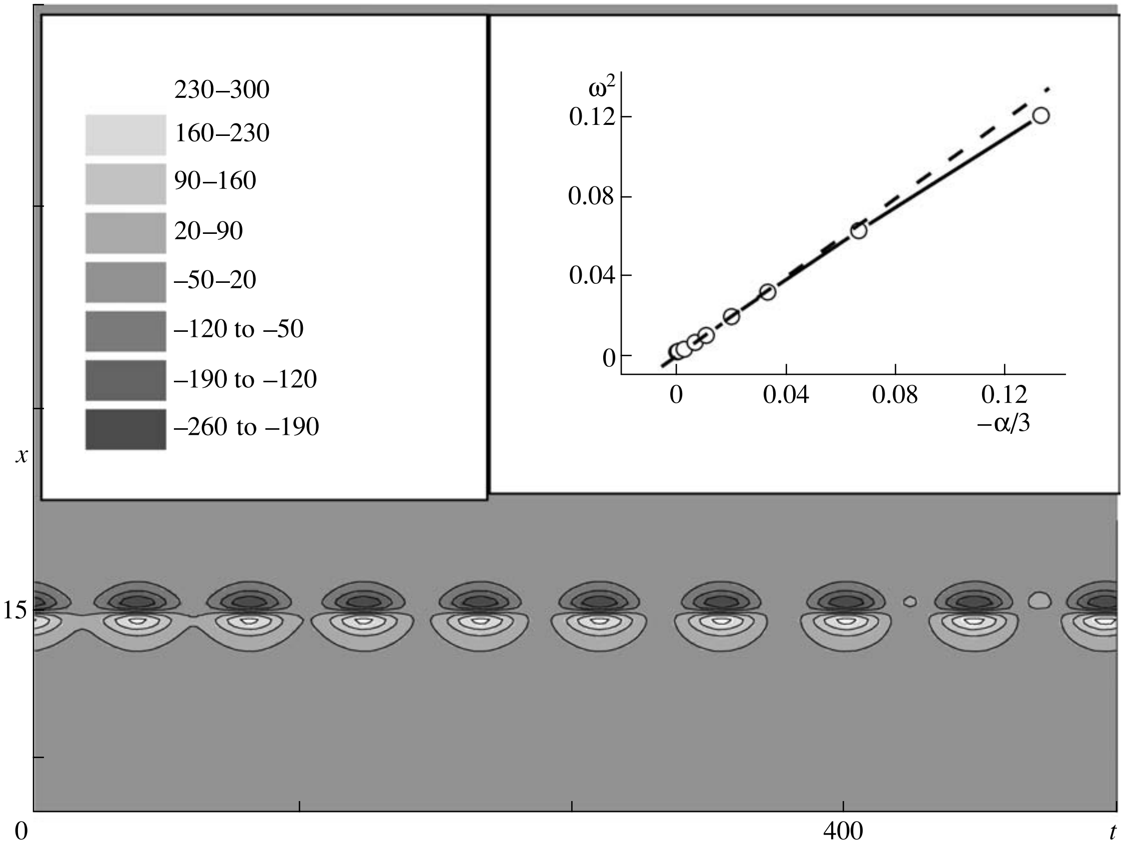

Fig. 1. Space–time dynamics of the difference field $\delta\tilde{\Omega}$ of the internal modes of the Bragg soliton in the presence of beatings of two modes with nonzero and zero frequencies. The inset shows the square of internal-mode oscillation frequency ω vs. the soliton-profile perturbation parameter α (dashed line) as calculated by Eq. (9) and (solid line) as obtained by numerically integrating Eqs. (1) with initial conditions (3), (5), and (10).

The low frequency of oscillations (9) is determined by the parameter of the soliton profile deformation $\alpha < 0$. The difference field $\delta\tilde{\Omega}$ given in Eqs. (10) is the superposition of two modes with nonzero and zero frequencies. The forms of these modes $\sim \operatorname{sech}\beta x \tanh\beta x$ are determined by functions φ_{1x} (6) and φ_x (8) and coincide with each other in the first approximation in the small parameter. This leads to effective beatings of these modes with the oscillating-mode frequency ω if $|\varphi_0| \approx 1$. Note that the presence of the zero-frequency internal mode for unperturbed soliton solutions [case $\omega = 0$ in Eq. (10)] is a characteristic feature of a number of nonlinear dynamic equations, including the sine-Gordon equation [3]. Figure 1 shows the results of the numerical integration of Eqs. (1) with the initial conditions in the form of the analytical solutions given by Eqs. (3), (5), and (10) for the standing soliton with the internal mode. The absence of losses on the emission of continuous spectrum waves indicates that the solutions found for the internal mode are stable. The oscillation frequency (see the inset in Fig. 1) and the form of the internal mode agree well with analytical results (9) and (10). In addition, this figure shows that, owing to beatings, the energy of the internal-mode fields varies from zero to a certain maximum value. In this case, the energy of the system of excited two-level atoms changes by the corresponding value due to a change in the conversion $n(x, t)$ given by Eq. (5). In the case considered above for the Bragg soliton with zero velocity, the beatings of the internal modes do not change the soliton velocity. However, for the moving Bragg soliton, a change in the maximum inversion of atoms in beatings of the internal modes is an additional perturbation of the soliton and can lead to a considerable change in the pulse propagation velocity.

Let us generalize the solutions obtained for the perturbed standing soliton given by Eqs. (3), (5), and (10) to the Bragg soliton propagating with low velocity $v \ll \omega$. We assume that the form of the envelop of the perturbed moving soliton coincides with the form of the exact solution [9], and the form of internal modes slightly differs from the above expressions (10). Let the pulse center coordinate $\xi(t)$ and its velocity $v(t) = \xi_t(t)$ depend on time due to the perturbation of the soliton in the presence of beatings of the internal modes. Thus,

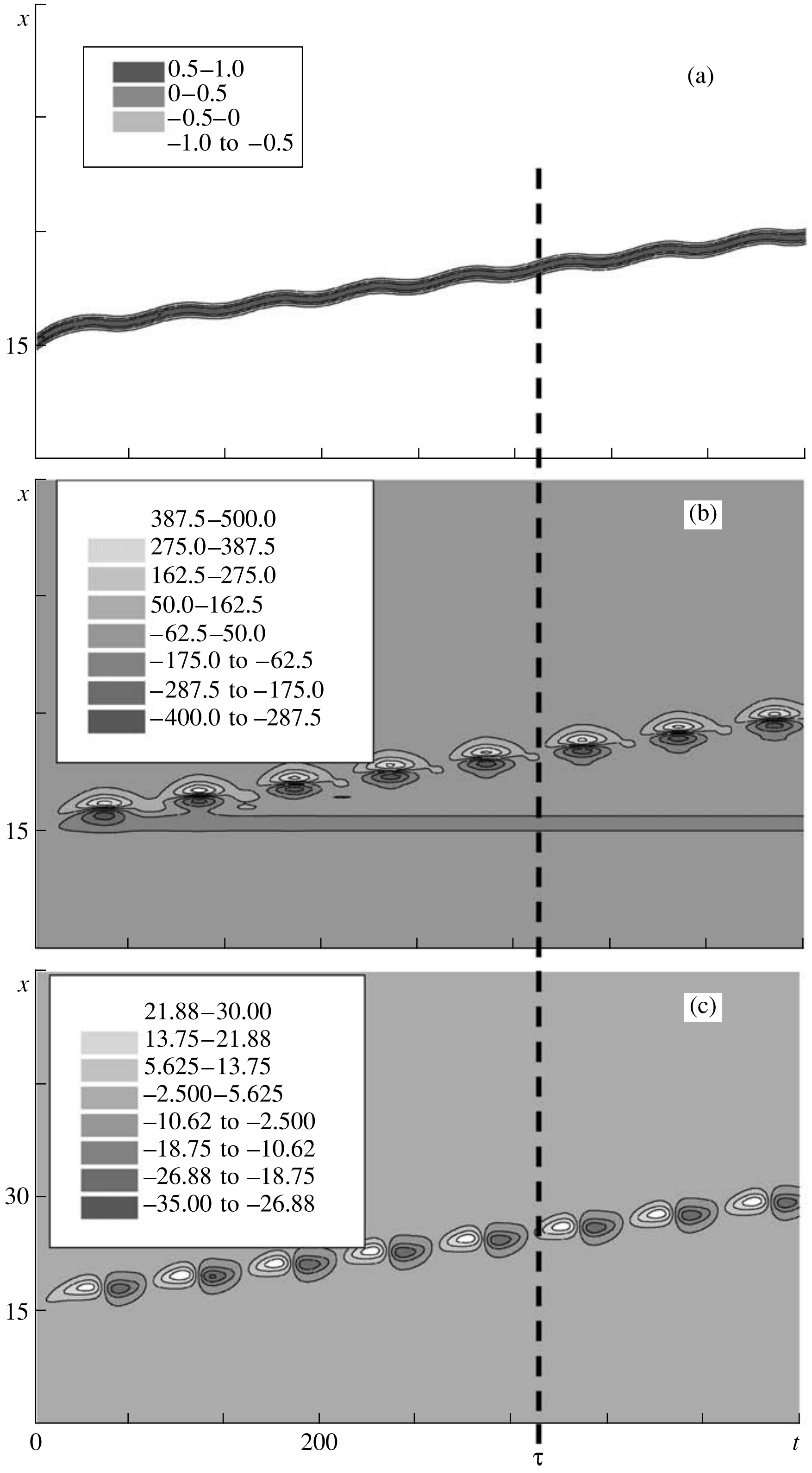

Fig. 2. Dynamics of the (a) inversion $n(x, t)$, (b) difference $\delta\tilde{\Omega}(x, t)$ (arb. units), and (c) total $\delta\Omega(x, t)$ (arb. units) internal-mode fields of the zoomeron-like pulse. The vertical dashed straight line corresponds to the time $t = \tau$ at which the amplitudes of internal-mode fields are equal to zero and the velocity of the pulse is maximal.

the trial solution is chosen in the form

$$\begin{aligned}
\Omega &= \frac{4v(t)}{\beta\sqrt{1-v^2}}\operatorname{sech}\frac{\beta(x-\xi(t))}{\sqrt{1-v^2}} \\
&\quad + i\varepsilon\omega\sin(\omega t)\operatorname{sech}\frac{\beta(x-\xi(t))}{\sqrt{1-v^2}}, \\
\tilde{\Omega} &= \frac{4}{\beta\sqrt{1-v^2}}\operatorname{sech}\frac{\beta(x-\xi(t))}{\sqrt{1-v^2}} \\
&\quad - i\frac{\varepsilon\beta}{\sqrt{1-v^2}}(\cos\omega t+\varphi_0)\operatorname{sech} \\
&\quad \times\frac{\beta(x-\xi(t))}{\sqrt{1-v^2}}\tanh\frac{\beta(x-\xi(t))}{\sqrt{1-v^2}}, \\
n &= \left(-1+2\operatorname{sech}^2\frac{\beta(x-\xi(t))}{\sqrt{1-v^2}}\right) \\
&\quad \times\left(1-\frac{1}{2}\varepsilon^2(\cos\omega t+\varphi_0)^2\operatorname{sech}^2\frac{\beta(x-\xi(t))}{\sqrt{1-v^2}}\right), \\
P &= -2\operatorname{sech}\frac{\beta(x-\xi(t))}{\sqrt{1-v^2}}\tanh\frac{\beta(x-\xi(t))}{\sqrt{1-v^2}} \\
&\quad + i\varepsilon\left(-1+2\operatorname{sech}^2\frac{\beta(x-\xi(t))}{\sqrt{1-v^2}}\right) \\
&\quad \times(\cos\omega t+\varphi_0)\operatorname{sech}\frac{\beta(x-\xi(t))}{\sqrt{1-v^2}}.
\end{aligned} \tag{11}$$

Substituting Eqs. (11) into the energy integral given in Eqs. (2), we arrive at the following expression for the pulse velocity:

$$v(t) = \frac{\varepsilon\omega\sqrt{\varphi_0}}{2}(1-\cos\omega t)^{1/2}. \tag{12}$$

As follows from Eqs. (11) and (12), the velocity and field amplitudes in the pulse, as well as the dipole moment and the inversion of atoms in the perturbed Bragg soliton, oscillate with the frequency of the internal mode of soliton (9), thus exhibiting the zoomeronlike dynamics of the pulse propagation.

In order to verify that the proposed trial solution given by Eq. (11) is sufficiently close to the exact solution, as well as to demonstrate the stability of such a zoomeronlike solution, we perform the direct numerical integration of Eqs. (1) taking analytical solution (11) as the initial conditions. As is seen in Fig. 2, the space–time dynamics of the inversion and internal-mode fields obtained in this integration correspond to analytical expressions (11). Similar results are also valid for the fields Ω_s and $\tilde{\Omega}_s$ of the soliton components of the solution and for the function of the dipole moment P. Topological charge (2) of the oscillating pulse obtained in numerical simulation satisfies the inequality $Q < 2\pi$, which corresponds to the analytical result with the substitution of solution (11) into Eq. (2): $Q = 2\pi + \alpha\pi$, where $\alpha < 0$. At the initial stage of the evolution of the solution, weak emission occurs (Fig. 2b), but the energy losses in this process are very small (about 0.05% of the pulse energy), which indicates that the trial zoomeronlike solution is close to the exact solution. The found zoomeronlike solution is quasistable, conserves stability for about one hundred oscillation periods, and elastically interacts with the soliton moving with velocity $v \geq 0.1$. The collision of two zoomeronlike pulses can be both elastic and inelastic, depending on the velocity and signs of the amplitudes of interacting pulses. Comparison of the plots in Fig. 2 provides a clear explanation of the cause of the appearance of oscillations in the zoomeronlike pulse. At $t = \tau$, when the pulse velocity is maximal (see Fig. 2a), the amplitudes of the internal-mode fields are equal to zero (see Figs. 2b and 2c). Further, the energy of internal modes increases due to the emission of the energy of excited medium atoms (the maximum inversion at the pulse center becomes less than unity in this case, see Fig. 3), the pulse stops and then the energy of the internal modes is absorbed by resonant atoms and the pulse is accelerated, again reaching the maximum velocity. Therefore, one can conclude that oscillations in the zoomeronlike pulse occur due to the beatings of the internal modes and to the energy exchange between the internal modes and resonant atoms, as follows from

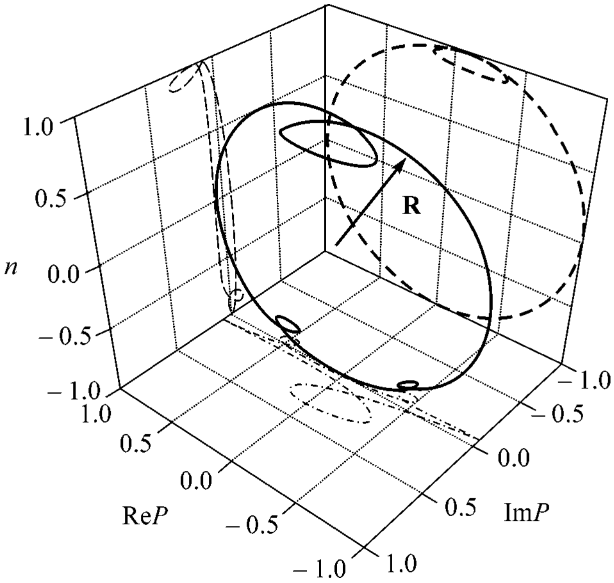

Fig. 3. (Solid line) Trajectory of the Bloch vector $\mathbf{R}(x = x_0; t) = \{\mathrm{Re}P; \mathrm{Im}P; n\}$ on a unit sphere at a certain point of the medium $x = x_0$ when the zoomeronlike pulse propagates. The dashed lines correspond to the projections of the shown trajectory on the coordinate planes. Each loop of the trajectory corresponds to one oscillation of the pulse.

analytical solutions (11) and (12). Moreover, the numerical simulation results confirm form (12) of the time dependence of the velocity of the zoomeronlike pulse and the linear frequency dependence of the maximum velocity. Thus, the solution given by Eqs. (11) and (12) for the zoomeronlike pulse accurately reproduces the dynamics of the oscillating pulse that is obtained in the direct numerical integration of two-wave Maxwell–Bloch equations (1).

In conclusion, we note that the two-wave Maxwell–Bloch equations, as follows from a number of the properties of their solutions, are incompletely integrable. It is difficult to expect that these equations have an exact zoomeron solution, which is an oscillating soliton of integrable nonlinear equations. For this reason, the approximate zoomeronlike solution described in this work is of interest as likely the first example of oscillating quasistable nonlinear solitary waves with nonzero average propagation velocity and a large amplitude of velocity oscillations, which appear in an actual physical problem, namely, in the problem concerning the propagation of laser pulses in a resonant Bragg structure.

I am grateful to A.I. Maĭmistov for stimulating discussions of the results. This work was supported by the Russian Foundation for Basic Research (project no. 04-02-16866).

REFERENCES

1. Yu. S. Kivshar and G. P. Agrawal, *Optical Solitons: From Fibers to Photonic Crystals* (Academic, San Diego, 2003).
2. F. Calogero and A. Degasperis, in *Solitons*, Ed. by R. Bullough and P. Caudrey (Springer, Berlin, 1980; Mir, Moscow, 1983).
3. Yu. S. Kivshar and B. A. Malomed, Rev. Mod. Phys. **61**, 763 (1989).
4. D. K. Campbell, J. F. Schonfeld, and C. A. Wingate, Physica D (Amsterdam) **9**, 1 (1983).
5. D. E. Pelinovsky, Yu. S. Kivshar, and V. A. Afanasjev, Physica D (Amsterdam) **116**, 121 (1998).
6. B. I. Mantsyzov and R. A. Silnikov, J. Opt. Soc. Am. B **19**, 2203 (2002).
7. A. De Rossi, C. Conti, and S. Trillo, Phys. Rev. Lett. **81**, 85 (1998).
8. B. I. Mantsyzov, Phys. Rev. A **51**, 4939 (1995).
9. B. I. Mantsyzov and R. N. Kuz'min, Zh. Éksp. Teor. Fiz. **91**, 65 (1986) [Sov. Phys. JETP **64**, 37 (1986)].

Translated by R. Tyapaev

JETP Letters, Vol. 82, No. 5, 2005, pp. 259–262. Translated from Pis'ma v Zhurnal Éksperimental'noĭ i Teoreticheskoĭ Fiziki, Vol. 82, No. 5, 2005, pp. 290–294.
Original Russian Text Copyright © 2005 by Razhev, Mkhitaryan, Churkin.

703- to 731-nm FI Laser Excited by a Transverse Inductive Discharge

A. M. Razhev[a], V. M. Mkhitaryan[b], and D. S. Churkin[a]
[a] *Institute of Laser Physics, Siberian Division, Russian Academy of Sciences, Novosibirsk, 630090 Russia*
e-mail: razhev@laser.nsc.ru
[b] *Physics Research Institute, National Academy of Sciences of Armenia, Ashtarak-2, 378410 Armenia*

Received July 11, 2005

It is proposed to use a pulsed transverse inductive discharge for exciting gas lasers operating on electron transitions in atoms and molecules. An electron transition laser on fluorine (FI) atoms pumped by a transverse inductive discharge is developed. Lasing at three wavelengths (703.75, 712.79, and 731.1 nm) is obtained by exciting He–F_2 (NF_3) gas mixtures in a pressure range from 20 to 350 Torr. The results of experimental investigation of the spectral, temporal, and energy characteristics of the inductive FI laser are presented. *© 2005 Pleiades Publishing, Inc.*

PACS numbers: 32.70.Fw, 42.55.Lt, 52.80.Yr

The rf induction excitation of continuous-wave lasing was reported in [1–3]. Continuous-wave lasing on transitions in atomic argon ions in the green spectral range under excitation by a longitudinal inductive rf discharge was obtained in [1, 2]. Lasing on vibrational transitions in CO_2 molecules in a wavelength range of 10.6 μm in an expanding nitrogen flow heated by an inductive discharge after the addition of cold CO_2 to it was reported in [3]. The possibility of developing a laser excited by a pulsed inductive discharge was discussed in [4].

In this work, a method for exciting laser active media by a pulsed transverse inductive discharge is proposed and experimentally implemented in order to obtain lasing on electron transitions in atoms and molecules in gases. It is important that the pulse repetition rate must be several hertz or higher; i.e., all processes of discharge formation, creation of population inversion, amplification, absorption, and quenching must occur during each pulse irrespective of the past history of the preceding pulse.

It is well known that a pulsed transverse electric discharge as a method for pumping gas lasers has a number of advantages over a pulsed longitudinal or continuous discharge. Here, we assume that the transverse discharge is an electric discharge in which the current flows in a direction perpendicular to the optical axis. Such a discharge ensures lasing on a very large number of transitions in atoms, molecules, and their ions due to realization of various (including new) mechanisms of producing population inversion in a wide range of pressures including atmospheric pressure. This lasing is achieved because a much higher level of pulsed pumping power is ensured in the transverse discharge and, therefore, lasing occurs at various transitions, including those for which no gain can be obtained for other types of discharge. As a result, lasers with a high radiation energy and a high efficiency (1–10%) can be developed. In contrast to conventional pulsed longitudinal and transverse discharges, a pulsed transverse inductive discharge is formed due to the magnetic field induction produced by the pumping system without any electrodes in the active medium. The appropriate choice of the tube material ensures the purity of the active medium considerable endurance of lasers. The formation of such a discharge is not accompanied by the appearance of cathode spots on the surface of the electrodes, which are responsible for the instability and contraction of the discharge, deterioration of the homogeneity of the discharge, contamination of the gas mixture, quenching of lasing, and limitation of the pulse repetition rate. The application of the pulsed inductive discharge for excitation is a promising method for pumping not only gas lasers, but also metal vapor lasers. In addition, this method can be used to produce a plasma for obtaining radiation (including induced radiation) in any spectral range, especially that extending from 10 to 150 nm, which is of considerable interest for microelectronics and photolithography.

To demonstrate the possibility of developing an inductive laser, we chose transitions in neutral fluorine atoms excited by a pulsed transverse inductive discharge in a He:F_2 (NF_3) mixture, because inversion in these transitions is reached at comparatively low excitation levels in a wide pressure range. In this case, a high gain is achieved, which ensures the superluminescence regime in a low-Q resonator, and lasing takes place in the red spectral region and the transition from spontaneous emission to the lasing mode is easily detected.

0021-3640/05/8205-0259$26.00 © 2005 Pleiades Publishing, Inc.

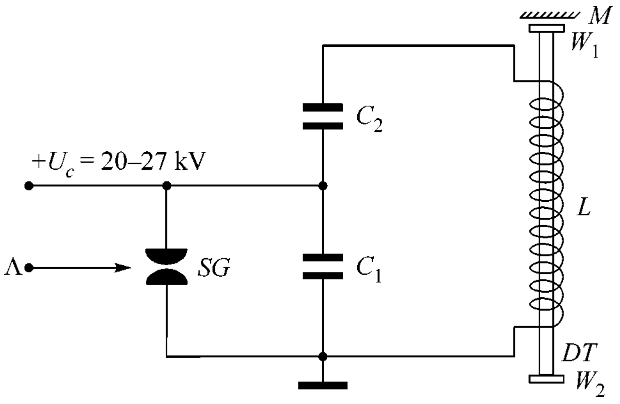

Fig. 1. Electric circuit of the system of excitation of a laser by a pulsed transverse inductive discharge: *SG* is an RU-65 standard spark gap, $C_1 = 50$ nF, $C_2 = 100$ nF, *DT* is the discharge tube, and *L* is the inductor.

There are many works on lasing on various transitions in fluorine atoms in a spectral range of 623–780 nm [5–16]. Lasing was observed on 17 lines. However, owing to different excitation conditions, the spectra obtained in different works differ in the number of lines with various wavelengths. Population inversion on atomic fluorine transitions was created using two methods of excitation, viz., a longitudinal electric discharge [5–9] in low-pressure (0.5–50 Torr) helium mixtures with fluorine-containing molecules and a transverse discharge [10, 12, 13, 15] ensuring lasing in the same mixtures in a wide pressure range up to 3 atm. At low pressures, HF, SF_6, CF_4, C_2F_6, NF_3, and F_2 molecules were used as fluorine donors, while only NF_3 and F_2 molecules were used for high pressures due to the homogeneity of the discharge achieved using the preliminary UV ionization of the discharge gap.

In most available experiments, lasing on transitions in fluorine atoms took place in the superluminescence regime. The duration of laser pulses in various experiments varied from a few microseconds (in a longitudinal discharge) to tens of nanoseconds (in a transverse discharge). The gas mixture forming the active medium of the laser usually consisted of helium and admixtures of fluorine-containing molecules in a ratio of 30 : 1 to 1000 : 1. Helium was required for creating inversion on transitions in fluorine atoms via excited states of helium atoms. The use of other inert gases (such as Ne or Ar) as the buffer gas did not lead to lasing. The above features of the operation of the FI laser indicate that it is a suitable device for obtaining lasing in a pulsed transverse inductive discharge.

To produce a pulsed transverse inductive discharge, we used the excitation system of an excimer laser, which was assembled as an L–C inverter circuit and was previously described in [17]. In this system, the peaking capacitor was removed and inductor *L* in the form of a 40–60-cm-long solenoid was connected (Fig. 1). The solenoid consisted of individual solenoids prepared in the form of parallel-connected sections wound on a glass tube into which gas mixtures were admitted. Each section contained 3 to 20 turns of a stranded insulated cable with a cross section from 1.5 to 4 mm^2. In experiments, inductor parameters such as the total inductance and resistance were varied to ensure the required values of the magnetic induction and electric field strength in the tube and, hence, the parameters of the inductive discharge. The experiments were carried out with glass tubes with an inner diameter of 1 to 4 cm and an active region length of 40–60 cm. At the ends of the tube, adjusting units with plane-parallel quartz or CaF_2 plates W_1 and W_2 were fixed. The plates were arranged perpendicularly to the tube axis and were used as sealing windows and optical cavity elements. On one side of the tube, a dense plane Al mirror or dielectric mirror *M* was placed.

We studied the intensity and duration of radiation emitted by the inductive discharge, as well as its spectral and energy characteristics under various excitation conditions. In our measurements, we used FEK-22 and FEK-15 coaxial photocells with a high time resolution, Tektronix TDS-220 and C1-104 oscilloscopes, an Ocean Optics HR 2000 spectrometer, and an Ophir Optronics pyroelectric laser radiation energy meter. The accuracy of measurements was 5%.

As the active medium for the laser, we chose He:F_2(NF_3) gas mixtures of various compositions under various pressures. Gas mixtures circulated in the tube with a low velocity. The charging voltage U_c across the reservoir capacitors C_1 and C_2 was varied from 20 to 27 kV. The best results were obtained in a tube with an inner diameter of 1.9 cm under the maximal voltage $U = 27$ kV; the total inductance of inductor *L* was equal to 60 nH in this case.

Under low pressures of the He:F_2 gas mixture in the pressure range from 1 to 4 Torr, the inductive discharge filled the tube almost uniformly over the cross section, but no lasing was achieved. An increase in pressure from 4 to 20 Torr led to a redistribution of the discharge from the center to the tube walls, and a ring-shaped discharge was observed.

Under pressures of the He:F_2 gas mixture from 20 to 350 Torr, lasing on transitions in fluorine atoms was obtained in the wavelength range 703–731 nm. Radiation was shaped in the form of a ring with an outer diameter of 1.9 cm and an inner diameter of about 1.7 cm. Thus, the active volume for a 40-cm-long solenoid was 22 cm^3.

Figure 2 shows the dependence of laser radiation intensity on the ratio of the mixture components. The optimal composition for our pumping conditions was He:F_2 (100 : 1). When F_2 was replaced by NF_3, lasing was also obtained, but with a lower intensity. For this reason, subsequent experiments were made on the He:F_2 (100 : 1) mixtures.

Figure 3 shows the dependence of laser radiation intensity on the total pressure in the He:F_2 (100 : 1)

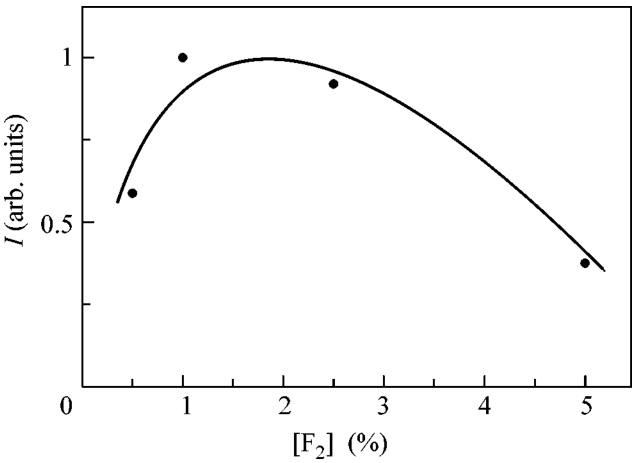

Fig. 2. Radiation intensity of the FI laser vs. the F_2 concentration in He under optimal pressure for $U_c = 27$ kV.

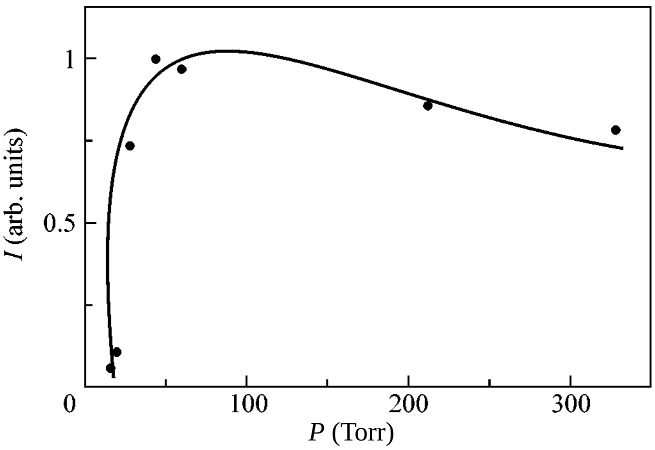

Fig. 3. Radiation intensity of the FI laser vs. the total pressure in the $He:F_2$ (100 : 1) mixture for $U_c = 27$ kV.

mixture. It can be seen that in the low-pressure range up to 60 Torr, the laser radiation intensity increases rapidly, reaches its peak value upon a further increase in pressure, and then decreases slowly. Such a dependence can be explained, on the one hand, by an increase in the gain in the medium with increasing pressure and, on the other hand, by the change in the electron parameters of the inductive discharge in the tube.

Analysis of the spectral composition of radiation shows that lasing occurs at three lines (703.7469, 712.7890, and 731.1019 nm), which correspond to the transitions $3p^2P^o_{3/2} \longrightarrow 3s^2P_{3/2}$, $3p^2P^o_{1/2} \longrightarrow 3s^2P_{1/2}$, and $3p^2S^o_{1/2} \longrightarrow 3s^2P_{3/2}$ [18].

It was found experimentally that the number of spectral lines in the radiation of the FI laser and the ratio of their intensities depend strongly on the total pressure in the gas mixture. Figure 4 shows the laser radiation spectrum in the pressure range from 28 to 328 Torr.

Figure 5 shows the oscillograms of voltage and spontaneous radiation under a pressure of 15 Torr, as well as oscillograms of laser radiation under a pressure of 250 Torr. The time dependence of the voltage across the inductor shows that it is of an oscillatory type, which indicates that the parameters of the excitation system were not properly matched to the parameters of the active medium in these preliminary experiments. Spontaneous radiation, as well as voltage, was of an oscillatory type, but with a period equal to half the period of voltage oscillations; in other words, radiation was emitted over the positive and negative half-periods of voltage oscillations. In contrast to spontaneous radiation, a laser radiation pulse appeared only at the beginning of the excitation pulse at the front of the first half-period and had a different shape with a much smaller duration. This is an indication of the transition to the amplification and lasing mode. Other evidence of the appearance of this mode is the spectral composition and directivity of radiation. When the lasing mode was achieved, an increase in pressure from 40 to 300 Torr shortened the duration τ of laser pulses (Fig. 6). Consequently, the pulse duration is a function of not only the

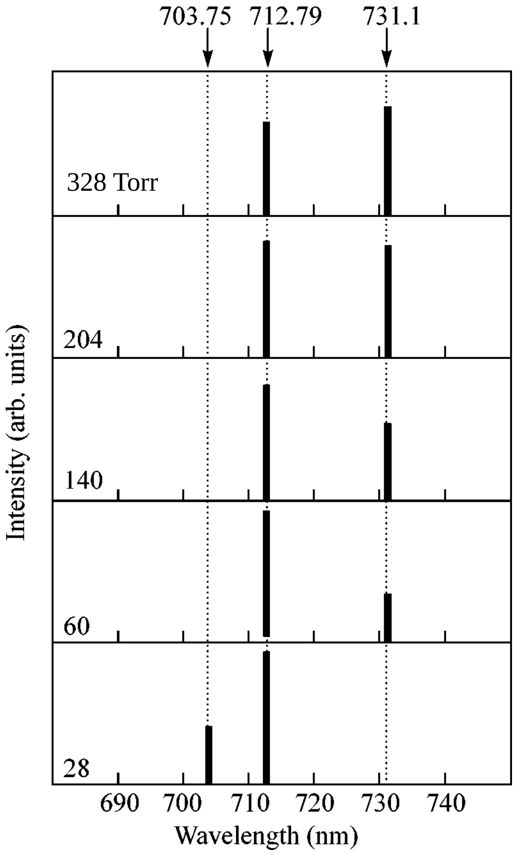

Fig. 4. Spectral composition of the radiation of the FI laser for various total pressures in the $He:F_2$ (100 : 1) mixture at $U_c = 27$ kV.

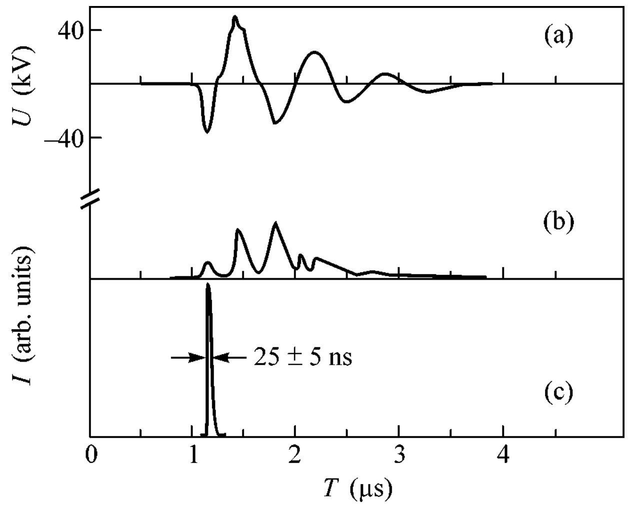

Fig. 5. Time dependence of (a) the voltage across the inductor *L*, (b) the spontaneous radiation of the inductive discharge in the He:F_2 (100:1) mixture under a pressure of 15 Torr, and (c) laser radiation intensity under a pressure of 250 Torr in the gas mixture.

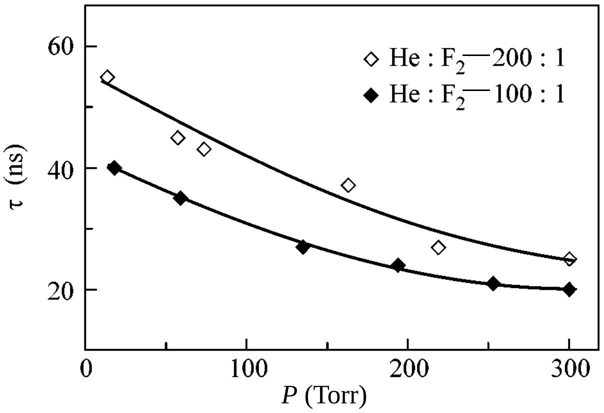

Fig. 6. Half-amplitude pulse duration of the FI laser vs. the total pressure of gas mixtures for two compositions, P = 250 Torr, and U_c = 27 kV.

total pressure but also of the ratio of the mixture components. Such behavior is typical of transverse discharge lasers characterized by short current pulses in gas mixtures [10, 12, 13, 15]. The minimum laser pulse duration in the He:F_2 (100 : 1) mixture under a pressure of 260 Torr and higher was 20 ± 2 ns. The maximum laser radiation energy was 0.12 mJ, which corresponded to a pulse power of 6 kW.

In our experiments, we measured the gain in the active medium using the cavity loss method. The maximum gain was about 0.025 cm^{-1}.

Thus, as a result of the experiments described above, the first laser excited by a pulsed transverse inductive discharge was created. Using transitions in the fluorine atom as an example, we demonstrated that population inversion can be created on electron transitions in atoms and molecules in an inductive electric discharge.

REFERENCES

1. W. E. Bell, Appl. Phys. Lett. **7**, 190 (1965).
2. J. P. Goldborough, E. B. Hodges, and W. E. Bell, Appl. Phys. Lett. **8**, 137 (1966).
3. L. I. Kiselevskiĭ, D. K. Skutov, and S. A. Sokolov, Zh. Prikl. Spektrosk. **21**, 951 (1974).
4. V. M. Mkhitaryan, Lazer Inform., Nos. 15–16, 18 (2004).
5. M. A. Kovacs and C. J. Ultee, Appl. Phys. Lett. **17**, 39 (1970).
6. W. Q. Jeffers and C. E. Wiswall, Appl. Phys. Lett. **17**, 444 (1970).
7. A. E. Florin and R. J. Jensen, IEEE J. Quantum Electron. **7**, 472 (1971).
8. J. R. English III, H. C. Gardner, and J. A. Merritt, IEEE J. Quantum Electron. **8**, 843 (1972).
9. D. G. Sutton, L. Galvan, P. R. Valenzuela, and S. N. Suchard, IEEE J. Quantum Electron. **11**, 54 (1975).
10. I. J. Bigio and R. F. Begley, Appl. Phys. Lett. **28**, 263 (1976).
11. L. O. Hocker and T. B. Phi, Appl. Phys. Lett. **29**, 493 (1976).
12. T. R. Loree and R. C. Sze, Opt. Commun. **21**, 255 (1977).
13. V. N. Lisitsyn and A. M. Razhev, Pis'ma Zh. Tekh. Fiz. **3**, 862 (1977) [Sov. Tech. Phys. Lett. **3**, 350 (1977)].
14. L. O. Hocker, J. Opt. Soc. Am. **68**, 262 (1978).
15. S. Sumida, M. Obara, and T. Fujioka, J. Appl. Phys. **50**, 3884 (1979).
16. J. E. Lawler, J. W. Parker, L. W. Anderson, and W. A. Fitzsimmons, IEEE J. Quantum Electron. **15**, 609 (1979).
17. A. M. Razhev, A. A. Zhupikov, and E. S. Kargapol'tsev, Kvantovaya Élektron. (Moscow) **34**, 95 (2004).
18. A. R. Striganov and G. A. Odintsova, *Tables of Spectral Lines of Atoms and Ions* (Énergoizdat, Moscow, 1982) [in Russian].

Translated by N. Wadhwa

JETP Letters, Vol. 82, No. 5, 2005, pp. 263–266. Translated from Pis'ma v Zhurnal Éksperimental'noĭ i Teoreticheskoĭ Fiziki, Vol. 82, No. 5, 2005, pp. 295–299.
Original Russian Text Copyright © 2005 by Reutova, Ul'maskulov, Sharypov, Shpak, Shunaĭlov, Yalandin, Belousov, Ginzburg, Denisov, Zotova, Rozental', Sergeev.

Experimental Observation of Superradiance in the Stimulated Scattering of an Intense Microwave Pump Wave by a Counterpropagating Subnanosecond High-Current Relativistic Electron Bunch

A. G. Reutova[a], M. R. Ul'maskulov[a], A. K. Sharypov[a], V. G. Shpak[a], S. A. Shunaĭlov[a],
M. I. Yalandin[a], V. I. Belousov[b], N. S. Ginzburg[b], G. G. Denisov[b], I. V. Zotova[b],
R. M. Rozental'[b], and A. S. Sergeev[b]

[a] *Institute of Electrophysics, Ural Division, Russian Academy of Sciences, ul. Amundsena 106, Yekaterinburg, 620016 Russia*
e-mail: yalandin@iep.uran.ru
[b] *Institute of Applied Physics, Russian Academy of Sciences, ul. Ul'yanova 46, Nizhni Novgorod, 603950 Russia*

Received May 19, 2005; in final form, July 12, 2005

The generation of ultrashort superradiant pulses in the stimulated scattering of an intense microwave (38 GHz) pump wave by a counterpropagating high-current relativistic electron bunch has been observed. Scattered radiation is a single ~200-ps pulse with a peak power of about 1 MW. Owing to the Doppler shift of the radiation frequency, frequencies up to 150 GHz are present in the spectrum of the scattered pulse. *© 2005 Pleiades Publishing, Inc.*

PACS numbers: 41.60.Cr, 52.59.Rz, 84.40.–x, 84.70.+p

1. Considerable attention is currently focused on theoretical and experimental investigations of the effects of superradiance of high-current relativistic electron bunches [1–7], which may be used to create fundamentally new sources of ultrashort superintense electromagnetic pulses. Superradiance is the coherent emission of a single electromagnetic pulse by an electron bunch with a length extended in the scale of the wavelength. Correspondingly, this process includes the development of self-bunching of particles, where in-phase emission from different parts of the bunch is ensured by the translation of the wave with respect to electrons due to the difference of the group velocity of the wave from the translational velocity of the particles. The superradiance of classical electron ensembles can be associated with various mechanisms of stimulated emission: cyclotron, Cherenkov, and undulator. To date, the generation of superradiant pulses through these mechanisms has been experimentally observed [5–7] in the centimeter and millimeter wavelength ranges.

The generation of ultrashort pulses in higher frequency ranges can be performed through a new superradiance mechanism that is realized in the process of the stimulated scattering of an intense electromagnetic pump wave by a moving electron bunch [2, 8]. When the pump wave with frequency ω_i propagates oppositely to the electron beam, owing to the Doppler effect, the scattered-radiation frequency ω_s is expected to be much higher than the pump frequency [9]:

$$\omega_s = \omega_i \frac{1 + V_{\parallel}/V_{\text{ph}.i}}{1 - V_{\parallel}/V_{\text{ph}.s}}, \tag{1}$$

where $V_{\parallel}$ is the translational velocity of the electrons and $V_{\text{ph}.i}$ and $V_{\text{ph}.s}$ are the phase velocity of the pump and scattered waves, respectively. In particular, when intense optical laser radiation is scattered by high-current beams with particle energies 1–2 MeV, the generation of superradiant pulses is possible in the UV range. The use of high-power relativistic electron microwave generators of the centimeter and millimeter ranges can provide the generation of submillimeter superradiant pulses.

The aim of this work is to carry out evaluation experiments for observation of the effect under discussion. The radiation of a high-power relativistic back wave oscillator of the 8-mm band was scattered by a high-current electron bunch with the moderately relativistic particle energy ($\gamma \sim 1.4$–1.6). The generation of subnanosecond superradiant pulses was detected in the short-wavelength part of the millimeter range. In order to compare with the experiment, a simple theoretical model is presented, where the waveguide character of the propagation of electromagnetic radiation, as well as the effect of the focusing magnetic field, is taken into account.

2. Let us consider the scattering of the electromagnetic pump wave by a counterpropagating electron

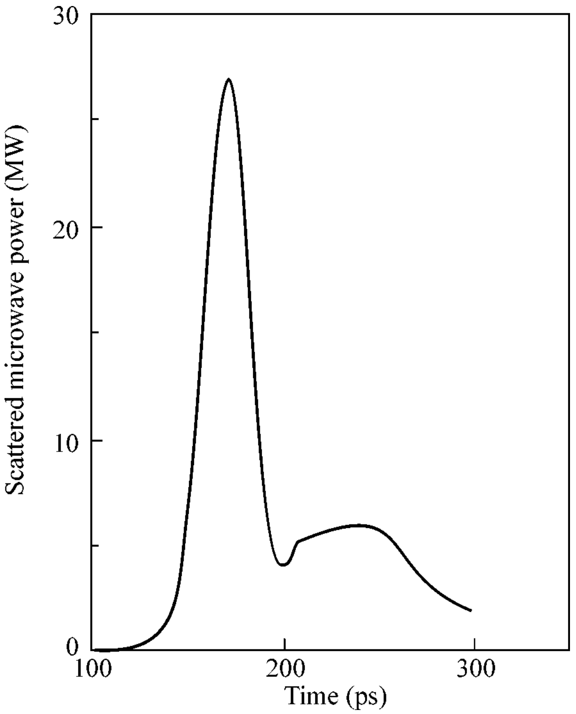

Fig. 1. Superradiant pulse formed due to the scattering of the pump wave by the relativistic electron bunch. The simulation parameters correspond to the experimental conditions.

bunch with duration Δt_b that moves through a smooth cylindrical waveguide with radius R along the uniform driving magnetic field $\mathbf{H}_0 = H_0\mathbf{z}_0$. In the approximation of the fixed pump-wave amplitude, the generation of short single pulses of scattered radiation (superradiant pulses) can be described by the system of equations including the time-dependent equation for the scattered-field amplitude and averaged equations of motion of electrons in the field of the combined wave

$$\frac{\partial a_s}{\partial \zeta} + \frac{\partial a_s}{\partial \tau} = i f(\tau) a_i \frac{1}{\pi}\int_0^{2\pi} e^{-i\theta} d\theta_0, \qquad (2)$$

$$\frac{\partial^2 \theta}{\partial \zeta^2} = \mu \operatorname{Im}\{a_s a_i g e^{-i\theta}\}.$$

Here, $\zeta = \omega_c z/c$; $\tau = \omega_c c(t - z/V_\parallel)(1/V_{gr} - 1/V_\parallel)^{-1}$; $a_{i,s} = eA_{i,s}/2m_0\gamma c^2$ are the normalized amplitudes of the (i) pump wave and (s) scattered radiation; $V_{\rm gr}$ is the group velocity of the scattered wave; $\theta = w_c t - k_c z$ is the phase of electrons with respect to the combination wave; $\omega_c = \omega_s - \omega_i$; $k_c = h_s + h_i$; h_i and h_s are the longitudinal wavenumbers of the pump wave and scattered wave, respectively; $\mu = \gamma_0^{-2}\beta_\parallel^{-3}$ is the bunching parameter; $I = (eJ_0/mc^3)(1/2\gamma_0 h_s k_c R^2 N_s)$; J_0 is the electron current; and N_s is the scattered-wave normalization constant. The parameter

$$g = J_{n_i - 1}(k_{\perp i}R_b)J_{n_s - 1}(k_{\perp s}R_b)\Omega/(\Omega - \omega_H) \qquad (3)$$

describes an increase in the amplitude of the oscillations of electrons in the pump field in the presence of the driving magnetic field near the cyclotron resonance, $\omega_H = eH_0/m_0c\gamma_0$ is the gyrofrequency, $\Omega = \omega_i + h_iV_\parallel$ is the frequency of the oscillations of electrons in the pump field, $J_n(x)$ is the Bessel function, $n_{i,s}$ is the azimuth index of the mode determining the transverse structure of the respective waves, R_0 is the electron injection radius, and $k_{\perp i,s}$ are the transverse wavenumbers. The function $f(\tau)$ specifies the profile of the electron bunch with normalized duration $\tau_b = \Delta t_b\omega_c c(1/V_{gr} - 1/V_\parallel)^{-1}$.

Equations (2) describe the joint action of the pump field and scattered wave on the electrons, which leads to the appearance of self-bunching of electrons. As a result, the amplitude of the scattered wave increases (exhaustion of the pump wave is negligible under the condition $\omega_s \gg \omega_i$ [9]). The slippage of the scattered wave with respect to the electrons, which is characteristic of superradiance, leads to the synchronization of emission from different parts of the extended bunch and the formation of scattered radiation in the form of a short pulse (see Fig. 1). It was assumed in numerical simulation that the small initial modulation of the electron density is the seed of radiation. The parameters of the pump wave and electron bunch are taken close to the experimental conditions. The pump wave with a power of 100 MW and a frequency of 38 GHz had the transverse structure of the TE_{11} mode. Scattering occurred to the same mode in a waveguide with a radius of 0.4 cm and a length of 20 cm by the electron bunch with a current of 1 kA and a particle energy of 200 keV that was focused by a magnetic field of 24 kOe. The calculated frequency of the scattered wave was equal to about 150 GHz. The bunch duration of 200 ps used in estimates corresponds to the plateau duration with a constant energy near the pulse peak of the accelerating voltage. As is seen in Fig. 1, a short electromagnetic pulse with a duration of about 50 ps is formed as a result of interaction. The peak power is approximately equal to 25 MW.

3. For experimental realization of the above mechanism of superradiance, a setup was created on the basis of two high-current RADAN-303 accelerators [10], which were synchronized with a subnanosecond accuracy and formed nanosecond and subnanosecond electron beams. The electron bunch from the first accelerator was used to generate a low-frequency pulse of the microwave pump wave, which then underwent scattering with an increase of the frequency by a counterpropagating subnanosecond beam formed in the second accelerator. Figure 2 shows the layout of the experimental setup.

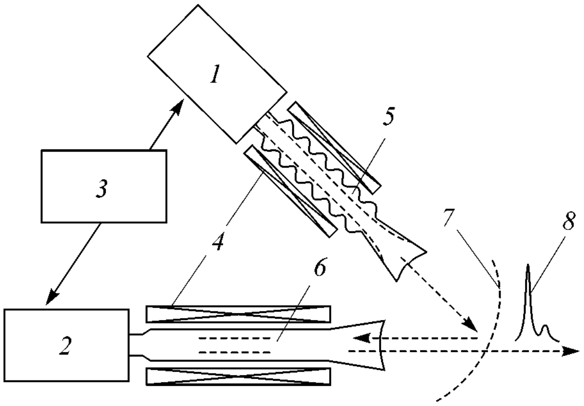

Fig. 2. Layout of the experiment on the observation of superradiance in the process of the scattering of the relativistic back wave oscillator by the counterpropagating high-current relativistic bunch: (*1*) the generator of a 4-ns electron beam, (*2*) the generator of a beam with duration less than 1 ns, (*3*) the generator of synchronizing voltage pulses, (*4*) pulsed solenoids, (*5*) the electrodynamic system of the relativistic inverse-wave 38-GHz lamp, (*6*) the scattering region, (*7*) the parabolic reflector, and (*8*) the superradiant pulse.

As a pump generator in the experiment, we used a relativistic back wave oscillator with a radiation frequency of 38 GHz [11]. Figure 3a shows the oscillogram of the pump pulse with a duration of about 4 ns and a power of 100 MW. The transfer of the TE_{11} pump wave to the scattering section and radiation extraction to the external space were performed by means of a quasi-optical parabolic mirror and a system of horn antennas. The mirror had high reflecting properties for the low-frequency pump wave: the mirror transmission coefficient at a frequency of 38 GHz was equal to about 95%. At the same time, the partial transparency of the mirror for microwave radiation with frequency above 60 GHz was ensured by means of an orthogonal lattice consisting of holes 3 mm in diameter with a step of 4 mm. Figure 3b shows the oscillogram of a signal from the hot-carrier microwave detector placed behind the quasi-optical mirror in the absence of the scattering beam. The pulse detected in this case was caused by the parasitic microwave radiation of the pump wave generator at the working-frequency harmonics.

In the scattering section, which is a section of the smooth waveguide with a length of about 40 cm, the pump wave propagating opposite to the subnanosecond (~600 ps at half maximum) high-current (250–300 keV, 1–1.5 kA) electron beam, which was formed by the second accelerator. In the absence of the pump wave, the noise radiation of the scattering beam was low and was not detected by the microwave detector placed behind the quasi-optical mirror. In the presence of the pump wave, a short high peak appears in the detected signal (see Fig. 3c), which can be treated as a superradiant pulse. With the inclusion of the voltage–power nonlinearity of the microwave detector used in the measurements, the FWHM of the superradiant pulse does not exceed 200 ps. Superradiant pulses were observed in a wide range of the rearrangement of the strength of the driving magnetic field. The highest power of superradiant pulses was obtained in the range 20–25 kOe, where, according to Eq. (3), the magnetic field noticeably affected the oscillation velocity of the particles.

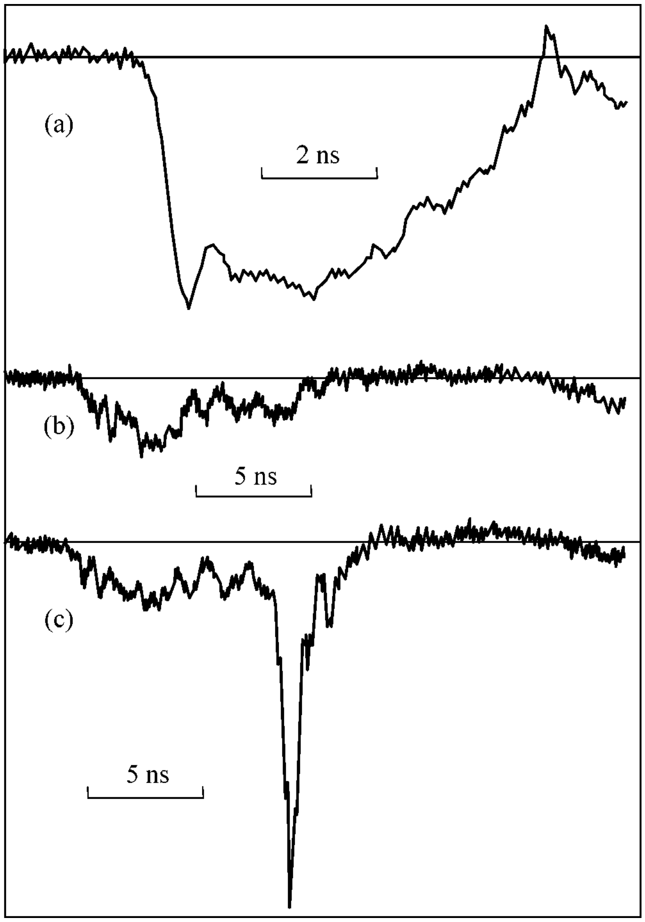

Fig. 3. (a) Typical pulse signal of the microwave detector recording the power envelop of the pump wave, (b) the microwave detector signal in the absence of the scattering electron bunch that is associated with the presence of multiple harmonics in the pump wave spectrum, and (c) the superradiant pulse recorded by the microwave detector in the presence of the scattering electron bunch.

In order to analyze the frequency content of the emitted pulse, calibrated waveguide low-frequency filters were placed to the detector channel. The relative amplitude of the detector responses governed by the signals passed through the microwave filters for various cutoff frequencies of the filters is shown in Fig. 4. The steps of the dashed line characterize the relative content of various spectral components in the microwave pulse. Thus, the main fraction of the radiation power is located in the range 3.5–4.2 mm. However, there are both lower and higher frequency components, including that with a wavelength of about 2 mm, close to the calculated

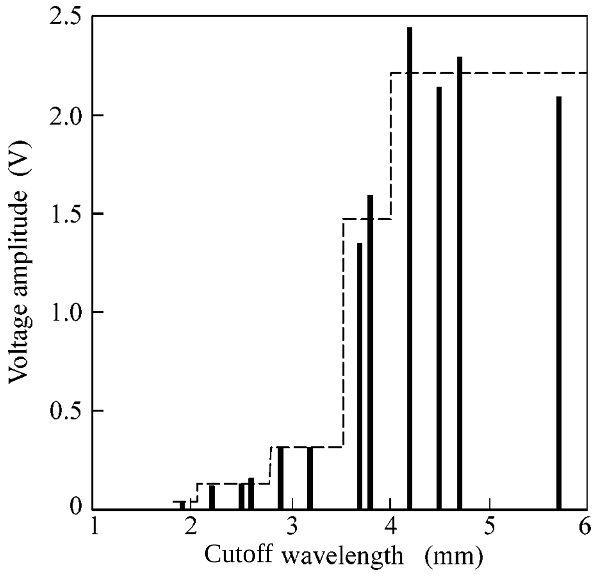

Fig. 4. Amplitude of the microwave detector signal vs. the cutoff wavelength of the low-frequency waveguide filters as a characteristic of the spectral content measured for scattered radiation.

value. It is worth noting that, owing to a decrease in the sensitivity of the detector with wavelength, the real decrease in the power for the short wavelength region should be much weaker than that seen in Fig. 4. The considerable broadening of the radiation spectrum compared to the initial theoretical model can be explained by the excitation of several waveguide modes corresponding to lower phase velocities and, correspondingly, lower frequencies of the scattered waves. Moreover, significant spread inevitably arises in the energy and velocity of electrons in an actual high-current bunch. These factors also lead to an increase in the duration of the superradiant pulse compared to the simulation results.

The spectrum-integrated power in the radiation peak is estimated as 1 MW. This value is determined from the power level recorded by the microwave detector with the inclusion of the aperture of the receiving antenna of the detector, the distance from the radiator, and the characteristic width of the directional radiation pattern. However, this estimate is approximate. On the one hand, the sensitivity of the hot-carrier detector, which was calibrated at a frequency of 38 GHz, decreases when detecting radiation of lower frequencies (to 150 GHz). On the other hand, the design and location of the parabolic quasioptical mirror were responsible for the complex interference pattern of radiation at the output of the setup, which makes it difficult to sum the detector records over the directivity pattern.

Thus, in the described experiments, the generation of short superradiant pulses was observed in the process of the stimulated scattering of the intense 38-GHz microwave pump wave by the counterpropagating high-current relativistic electron bunch. Scattered radiation is a single 200-ps pulse with a spectrum-integrated power up to 1 MW. Owing to the Doppler shift of the radiation frequency, frequencies up to 150 GHz are present in the spectrum of the scattered pulse. The above effect can be interpreted as the superradiance of the electron bunch, because radiation is generated in the absence of the external high-frequency signal and external resonators; i.e., it cannot be a result of the traditional mechanisms of amplification and autogeneration. In addition, owing to the development of a group of particles in the extended bunch, the power of the scattered signal is much higher than the power of noise spontaneous radiation in the pump field that is caused by bunch density fluctuations and the duration of the pulse is much shorter than the duration of this noise.

This work was supported by the Russian Foundation for Basic Research (project no. 05-02-17553-a).

REFERENCES

1. R. Bonifacio, N. Piovella, and B. W. J. McNeil, Phys. Rev. A **44**, 3441 (1991).
2. N. S. Ginzburg and A. S. Sergeev, Pis'ma Zh. Éksp. Teor. Fiz. **54**, 445 (1991) [JETP Lett. **54**, 446 (1991)].
3. L. A. Vaĭnshteĭn and A. I. Kleev, Dokl. Akad. Nauk SSSR **311**, 862 (1990) [Sov. Phys. Dokl. **35**, 359 (1990)].
4. N. S. Ginzburg, I. V. Zotova, and A. S. Sergeev, Pis'ma Zh. Éksp. Teor. Fiz. **60**, 501 (1994) [JETP Lett. **60**, 513 (1994)].
5. N. S. Ginzburg, I. V. Zotova, A. S. Sergeev, *et al.*, Phys. Rev. Lett. **78**, 2365 (1997).
6. V. G. Shpak, M. I. Yalandin, N. S. Ginzburg, *et al.*, Dokl. Akad. Nauk **365**, 50 (1999) [Dokl. Phys. **44**, 143 (1999)].
7. A. A. El'chaninov, S. D. Korovin, V. V. Rostov, *et al.*, Pis'ma Zh. Éksp. Teor. Fiz. **77**, 314 (2003) [JETP Lett. **77**, 266 (2003)].
8. N. S. Ginzburg, I. V. Zotova, A. S. Sergeev, *et al.*, Pis'ma Zh. Tekh. Fiz. **26** (17), 103 (2000) [Tech. Phys. Lett. **26**, 694 (2000)].
9. V. L. Bratman, N. S. Ginzburg, and M. I. Petelin, Zh. Éksp. Teor. Fiz. **76**, 930 (1979) [Sov. Phys. JETP **49**, 469 (1979)].
10. M. I. Yalandin and V. G. Shpak, Prib. Tekh. Éksp., No. 3, 5 (2001) [Instrum. Exp. Tech. **44**, 285 (2001)].
11. M. I. Yalandin, G. T. Smirnov, V. G. Shpak, *et al.*, in *Proceedings of the 9th IEEE International Pulsed Power Conference* (Albuquerque, USA, 1993), Vol. 1, p. 388.

Translated by R. Tyapaev

JETP Letters, Vol. 82, No. 5, 2005, pp. 267–272. Translated from Pis'ma v Zhurnal Éksperimental'noĭ i Teoreticheskoĭ Fiziki, Vol. 82, No. 5, 2005, pp. 300–305.
Original Russian Text Copyright © 2005 by Zimnyakov, Kuznetsova, Pravdin.

Anomalous Diffusion of Light in TiO_2-Powder Layers near the Absorption Edge

D. A. Zimnyakov, L. V. Kuznetsova, and A. B. Pravdin
Saratov State University, Saratov, 410012 Russia
e-mail: zimnykov@sgu.ru

Received July 12, 2005

The transfer of visible and near-IR radiation in layers of polydisperse TiO_2 (rutile) particles has been studied by measuring diffusion transmission and coherent backscattering in order to determine the optical parameters of the samples under investigation. An approach based on the coherent potential approximation is applied. It has been shown that, in the short-wavelength region of the visible range, anomalous diffusion of light occurs due to the effect of interference at mesoscopic scales on the transport characteristics of the scattering medium.
© 2005 Pleiades Publishing, Inc.

PACS numbers: 42.25.Dd, 42.70.Qs

At present, the effect of the localization of light in randomly inhomogeneous media is being actively analyzed both theoretically and experimentally. Interest in this phenomenon was initiated by the possibilities of creating new materials with unique optical properties (in particular, disperse laser media; see, e.g., [1–3]). The transition from the localized states of the light field in a scattering medium to the localization regime is determined by the Ioffe–Regel criterion $kl^* \leq 1$ [4], where k is the wavenumber of light in the medium and l^* is the transport length determined by the scale at which the wave vector of propagating radiation is randomized [5]. For most multiple scattering media, $kl^* \gg 1$ and radiation transfer is described using radiation-transport theory [5, 6]. In particular, analysis of the dependence of the transmittance T of the medium layer on the layer thickness L in the absence of absorption in the diffusion approximation of radiation-transport theory yields the known relation $T_{L \gg l^*} \propto l^*/L$ [5, 7, 8], which agrees well with experimental data. According to the current concept, interference at a characteristic scale ξ that exceeds l^* and increases as kl^* decreases affects radiation transfer for $kl^* \longrightarrow 1$. The contribution of interference to radiation transfer is responsible for the dependence of the transport characteristics of the medium (transport length and radiation diffusion coefficient) on the sizes of the scattering system and, correspondingly, in specific differences from the classical laws of radiation diffusion. In particular, the deviation of the dependence $T(L)$ from the diffusion law $T \propto L^{-1}$, as well as broadening and characteristic changes in the shape of the coherent backscattering peak, is expected to be observed in this case [9, 10]. At the localization threshold, $kl^* = 1$, $\xi \longrightarrow \infty$, and $l^* \longrightarrow 0$ and scaling localization theory [11] predicts the inverse square dependence $T \propto L^{-2}$. Below the threshold, $T \propto \exp(-L/\eta)$, where η is the scale depending on kl^* and is called the localization length. Thus, the transition from the radiation transfer regime in the layer $T \propto L^{-1}$ to the $T \propto L^{-2}$ regime is a characteristic criterion of the achievement of the threshold $kl^* = 1$. For this reason, analysis of experimental dependences $T(L)$ is often used to identify the threshold regime of radiation transfer in scattering media [12, 13].

In contrast to mesoscopic media with a regular structure (photon crystals), the conditions for the transition to localized states of the light field in randomly inhomogeneous media are restricted by a number of fundamental factors (effect of the self-absorption of the medium, nonmonotonic dependence of l^* on the volume fraction p of scattering centers, frequency-size constraints associated with the width of low-order Mie resonances, dispersion dependence of the scattering center material). There are only a few experimental works devoted to investigations of radiation transfer in disordered media near the localization threshold [12, 14–16]. In this work, we study the propagation of light (λ = 400–800 nm) in close-packed layers of polydisperse particles of titanium dioxide (rutile). The results show the features of the diffusion of radiation in the short-wavelength region of the visible range ($\lambda_0 \leq$ 500 nm), which can be interpreted in terms of the effect of interference on radiation transfer in scattering media. These features are attributed to the high refractive index of rutile in the visible range ($n \geq 2.4$). For such a scattering system, the localization parameter close to the critical value $kl^* = 1$ can be obtained at a certain relation between λ_0 and the parameters $\bar{a}$ and $\delta_a = \sqrt{\overline{(a-\bar{a})^2}}$ (a is the characteristic size of a randomly chosen scattering center).

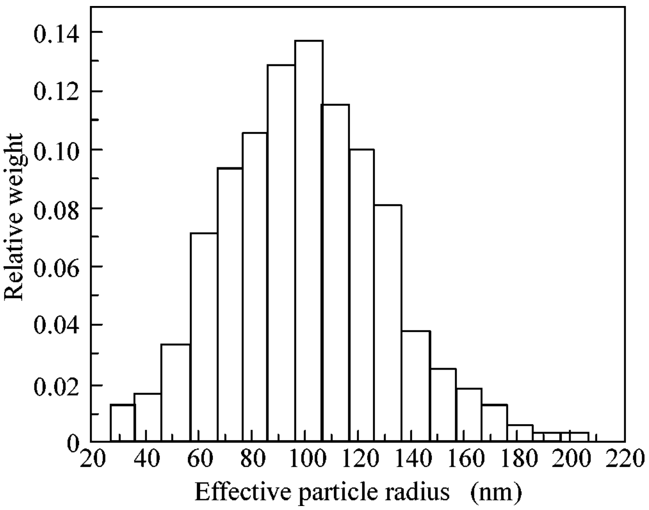

Fig. 1. Histogram of the effective radius of TiO_2-based pigment particles.

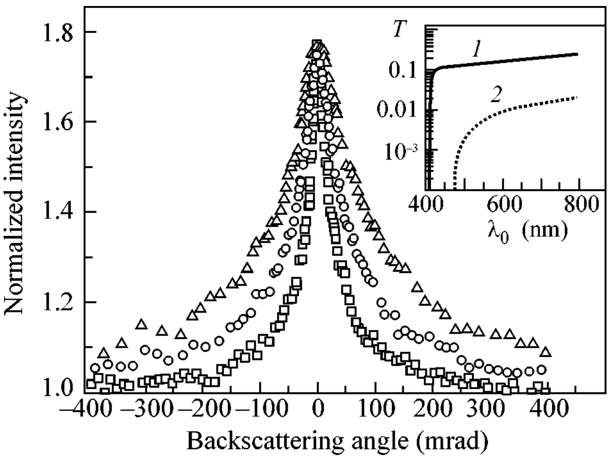

Fig. 2. Coherent backscattering peaks for the samples under investigation for (□) 633, (○) 532, and (△) 473 nm. The inset shows the diffusion-transmission spectra for the samples with L = (*1*) 17 and (*2*) 340 μm.

We analyze samples of the layers of polydisperse particles of titanium dioxide (rutile) obtained as a result of the participation of colloid suspensions of TiPure R900 (DuPoint Corp.) pigment in deionized water. Participation was performed on glass substrates with the subsequent slow evaporation of the liquid phase. The resulting layers with the volume fraction of scatterers $p = 0.35 \pm 0.03$ had a thickness of 15 to 350 μm. The thickness was measured by a scanning laser profilometer with an error of 1.5 μm. We selected samples with a layer thickness inhomogeneity of no more than 5% on an area of no less than 2 cm^2, which had no cracks, chips, etc. in the region under investigation. The sizes of the initial-material particles were analyzed using a scanning electron microscope (Hitachi with a magnification of 35 000). Figure 1 shows the histogram of the effective radius a of scatterers (with allowance for asphericity, it is determined as $a = \sqrt[3]{3V/4\pi}$, where V is the particle volume calculated from the electron-microscopy data).

The spectra of the diffusion transmission $T(\lambda_0)$ of the samples were obtained using a Cary-2145 spectrophotometer. Angular measurements of the coherent backscattering peaks were carried out for linearly polarized light with λ_0 = 633 nm (a He–Ne laser), λ_0 = 532 nm (the second harmonic of an YAG:Nd laser, λ_0 = 1064 nm), and λ_0 = 473 nm (the second harmonic of an YAG:Nd laser, λ_0 = 946 nm). The coherent backscattering peaks were measured using a goniophotometer based on a G-5 goniometer with a system for detecting backscattered radiation (a polarizer for the separation of the co-polarized component of scattered light and an objective with f = 80 mm). The face of a multimode light guide with a core diameter of 50 μm was placed in the focal plane of the objective for the collection of radiation backscattered at the angle θ and transmitted it to a photoreceiver (an HC-7468 Hamamatsu module). Figure 2 shows the coherent backscattering peaks for the samples under investigation. The inset shows the diffusion-transmission spectra for two samples with significantly different thicknesses.

The experimental data were analyzed using effective-medium theory—the coherent potential approximation [17–19]. In the framework of this approach, the characteristics of a real scattering medium (effective refractive index n_{eff}, scattering length l, transport length l^*, wavenumber k, and the effective phase speed of light) are determined from the complex refractive index $\tilde{n}_{\mathrm{eff}}$ of the homogeneous effective medium. The complex refractive index $\tilde{n}_{\mathrm{eff}}$ is determined from the minimization condition ($\langle\Sigma\rangle$) of the total cross section for a scattering center embedded into the effective medium. As the scattering center, we consider a sphere with radius a and the refractive index that is equal to either the refractive index n_{sc} of the scatterer material or the refractive index n_{bk} of the medium containing scatterers. In the framework of the classical coherent-potential approximation, minimization ($\langle\Sigma\rangle$) is reduced to the minimization of $\langle f(0, \tilde{n}_{\mathrm{eff}})\rangle = \langle p f_1(0, \tilde{n}_{\mathrm{eff}}) + (1-p) f_2(0, \tilde{n}_{\mathrm{eff}})\rangle$, where $f_{1,2}(0, \tilde{n}_{\mathrm{eff}})$ is the amplitude of the forward scattering of scattering centers with the refractive indices n_{sc} and n_{bk}, respectively, which is calculated using Mie theory for a spherical particle [20]. This procedure is reduced to the solution of the iterative equation

$$\tilde{q}_{i+1} = \tilde{q}_i + \frac{K}{\tilde{q}_i}\langle f(0, \tilde{n}^i_{\mathrm{eff}})\rangle, \qquad (1)$$

where $\tilde{q}_i = 2\pi\tilde{n}^i_{\mathrm{eff}}/\lambda_0$ is the complex wavenumber of light in the effective medium at the ith iteration step and K is the parameter chosen from the condition of the best convergence of the iteration procedure. For polydisperse scattering systems, $\langle f(0, \tilde{n}^i_{\text{eff}})\rangle$ is calculated by averaging over all possible a values. We used the modification of the coherent-potential approximation (coated CPA [17, 21]), where a sphere in a shell with the refractive index n_{bk} is considered as a scattering center in the effective medium. The radius of the inner sphere with the refractive index n_{sc} is equal to the radius of the scatterer, and the outer radius of the shell is calculated as $a' = az[p(z^3 - 1) + 1]^{-1/3}$, where $z \approx 1.65$. A homogeneous sphere with the radius $a'' = z(a^3 - pa'^3)^{1/3}$ is considered as a scattering center of the second type with the refractive index n_{bk}. This procedure makes it possible to take into account the effects of the correlation in the positions of scatterers for high packing densities more exactly than in the usual coherent-potential approximation.

In this approach, $\tilde{n}_{\text{eff}}$ is also calculated by solving iterative equation (1). After the completion of the iteration procedure, the parameters of the scattering system are determined as $l = \lambda_0/4\pi\,\text{Im}(\tilde{n}_{\text{eff}})$ and $n_{\text{eff}} = \text{Re}(\tilde{n}_{\text{eff}})$. For anisotropic scattering, radiation transfer is governed by the transport length $l^* \geq l$. The l^* value for a given n_{eff} value is determined using the iteration procedure minimizing $\langle\sigma_{\text{ext}}\rangle - \langle\sigma_{\text{asym}}\rangle$, where σ_{ext} and σ_{asym} are the cross sections for the extinction and asymmetry of the scattering center in the effective medium that are calculated using Mie theory for the sphere in the shell [20, 21].

We applied an original approach to determine l^* and n_{eff} for various λ_0 values in the case of the absence of a priori data on the optical characteristics of scatterers [$n_{\text{sc}}(\lambda_0)$ spectra]. Although information on the optical characteristics of chemically pure oxides is available [22, 23], the use of these data for calculating l^* and n_{eff} is doubtful because of the presence of impurities (e.g., SiO_2) in the TiPure R900 under consideration. For the known size distribution of scatterers (Fig. 1), the parametric dependence $l^*(n_{\text{sc}}) = \varphi_{\text{CPA}}(n_{\text{eff}}(n_{\text{sc}}))$ with n_{sc} as a parameter can be obtained using the coherent-potential approximation. The (n_{eff}, l^*) values corresponding to this dependence certainly minimize $\langle(0, \tilde{n}_{\text{eff}})\rangle$ and $\langle\sigma_{\text{ext}}\rangle - \langle\sigma_{\text{asym}}\rangle$ for given n_{sc} and λ_0 values. At the same time, in the diffusion approximation, the T value and width $\Omega_{0.5}$ of the coherent backscattering peak that are measured in the experiment for λ_0 can be represented by the expressions [8, 24]

$$T(n_{\text{eff}}, l^*) = \frac{\{1 + z_1(n_{\text{eff}})\}l^*}{L + \{z_1(n_{\text{eff}}) + z_2(n_{\text{eff}})\}l^*}, \tag{2}$$

$$\Omega_{0.5} \approx \frac{\lambda_0}{3\pi l^*}\Xi(n_{\text{eff}}), \tag{3}$$

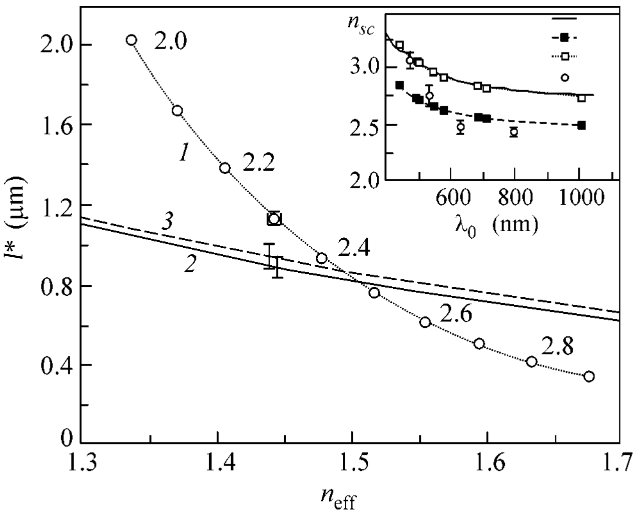

Fig. 3. Method for determining l^*, n_{eff}, and n_{sc} from experimental values of T and $\Omega_{0.5}$ with the coherent-potential approximation for λ_0 = 633 nm and $l^*(n_{\text{sc}})$ = (*1*) $\varphi_{\text{CPA}}(n_{\text{eff}}(n_{\text{sc}}))$, (*2*) $\psi_\Omega(n_{\text{eff}})$, and (*3*) $f_T(n_{\text{eff}})$. The inset shows n_{sc} vs. λ_0 according to (○) [22], (■) n_o [23], (□) n_e [23], and (lines) data obtained using the coherent-potential approximation.

where $z_{1,2}(n_{\text{eff}})l^*$ are the extrapolation-length values that are determined by the boundary conditions for the equation of the diffusion of light at the boundaries of the layer and depend on the reflectivities $R_{1,2}$ of the boundaries. The function $\Xi(n_{\text{eff}})$ describes the effect of the reflectivity of boundary *1* for the case $L \gg l^*$ on the coherent backscattering peak width, is equal to 1 for $R_1 = 0$, and decreases monotonically as R_1 increases. Using the results obtained in [25], we arrive at the expressions $z_{1,2} = 2\{1 + R(n_{\text{eff}}, n_{1,2})\}/3\{1 - R(n_{\text{eff}}, n_{1,2})\}$ and $\Xi(n_{\text{eff}}) = \{1 - R(n_{\text{eff}}, n_1)\}/\{1 - 0.2R(n_{\text{eff}}, n_1)\}$, where n_1 and n_2 is the refractive indices of the media surrounding the scattering layer. For the case under consideration, $n_1 = 1$ (free space) and $n_2 \approx 1.5$ (glass substrate). The function $R(n_{\text{eff}}, n_{1,2})$ is calculated by integrating the Fresnel reflection coefficients for unpolarized light over all possible angles of incidence of light on the boundary. For measured T and $\Omega_{0.5}$ values, the parametric dependences $l^* = f_T(n_{\text{eff}})$ and $l^* = \psi_\Omega(n_{\text{eff}})$ can be constructed using Eqs. (2) and (3). The conditions $\varphi_{\text{CPA}}\{n_{\text{eff}}(n_{\text{sc}})\} = f_T(n_{\text{eff}})$ and $\varphi_{\text{CPA}}\{n_{\text{eff}}(n_{\text{sc}})\} = \psi_\Omega(n_{\text{eff}})$ unambiguously determine the parameters n_{eff}, l^*, and n_{sc} of the scattering medium. Figure 3 illustrates the application of this approach to the T and $\Omega_{0.5}$ values for λ_0 = 633 nm. The confidence intervals correspond to measurement errors for T, $\Omega_{0.5}$, L, and p. The table presents the estimates obtained by this procedure for l^*, n_{eff}, n_{sc}, and kl^* for various λ_0 values. The inset in Fig. 3 shows the values obtained for n_{sc} in comparison with the spectral dependences taken from [22, 23] for the refractive indices n_o and n_e for chemically pure rutile. The insignificant divergence between n_{sc} and n_o can be

The l^*, n_{eff}, n_{sc}, and kl^* values for the samples under investigation as obtained from the experimental data

λ_0, nm	l^*, μm	n_{eff}	n_{sc}	kl^*	Data source
800	2.15 ± 0.30	1.45 ± 0.05	2.45 ± 0.05	24.4 ± 2.5	Measurements of T
633	0.86 ± 0.06	1.49 ± 0.06	2.45 ± 0.06	12.72 ± 0.34	Measurements of T
	0.82 ± 0.05	1.52 ± 0.06	2.49 ± 0.04	12.37 ± 0.30	Measurements of coherent backscattering
532	0.27 ± 0.04	1.67 ± 0.05	2.74 ± 0.11	5.30 ± 0.65	Measurements of T
	0.26 ± 0.04	1.69 ± 0.07	2.78 ± 0.08	5.10 ± 0.45	Measurements of coherent backscattering
473	$0.075 \le l^* \le 0.13$	$1.88 \le n_{\text{eff}} \le 2.0$	$3.00 \le n_{\text{sc}} \le 3.15$	$2.0 \le kl^* \le 3.2$	Measurements of coherent backscattering

attributed to the effect of impurities in the pigment under investigation.

Calculations of n_{eff} and l^* were performed for the scattering medium without absorption ($\text{Im}(n_{\text{sc}}) = 0$), which is justified for the samples under investigation in the range $\lambda_0 = 473$–800 nm. In this range for the samples under investigation, the minimum absorption length [5, 7, 8] $L_a = \sqrt{3l^*/\mu_a} \approx 45$ μm (μ_a is the absorption coefficient of the medium) for $\lambda_0 = 473$ nm is much larger than l^*. The n_{eff} and l^* values were determined for various L values from the T values for $\lambda_0 = 800$, 633, and 532 nm. For $\lambda_0 = 473$ nm, only $\Omega_{0.5}$ values are analyzed, because absorption that is ignored in the model under consideration significantly affects the diffusion transmission of samples with $L \ge L_a$. For smaller L values, systematic deviations of the experimental dependence $T(L)$ from dependence (2) are observed. In coherent backscattering experiment for $\lambda_0 = 473$ nm, a peak that is anomalously wide compared to that predicted by diffusion theory (3) is also observed. Owing to this behavior, the dependences $l^*(\psi_\Omega(n_{\text{eff}})$ and $l^*(n_{\text{sc}}) = \varphi_{\text{CPA}}(n_{\text{eff}}(n_{\text{sc}}))$ do not intersect each other. In this case, the difference between the parameters obtained in the coherent-potential approximation and diffusion approximation (4) in the region of the minimum difference between the dependences does not exceed 25–30% for l^* and 5–7% for n_{eff}. In addition, a small deviation (smoothing) of the shape of the observed coherent backscattering peak from the diffusion contour for nonabsorbing media is observed in the small-angle region. This effect cannot be attributed to the effect of the self-absorption of TiO_2 that increases in the short-wavelength region of the visible range, because the enhancement factor obtained for coherent backscattering at $\lambda_0 = 473$ nm is approximately equal to the values for $\lambda_0 = 532$ and 633 nm (Fig. 2), and the effect of absorption on the coherent backscattering peak is manifested in the smoothing of the peak with a simultaneous decrease in the amplification factor [26]. Moreover, for $\lambda_0 = 473$ nm, the relation $L_a \gg l^*$ is valid and, therefore, the effect of absorption on the shape and width of the coherent backscattering peak is negligibly small [26]. As was shown in theoretical work [10], effects similar to those observed in our experiment (smoothing and broadening of the peak) are expected near the localization threshold.

The sharp decrease in kl^* with λ_0 (see table), as well as anomalies observed in the coherent backscattering experiment for $\lambda_0 = 473$ nm, implies that interference at scales exceeding l^* contributes to radiation transfer in this case. According to the scaling theory of the renormalization of the scattering-medium parameters near the localization threshold [11], the transport length is represented as

$$\tilde{l}^* = l^{*2}\left(\frac{1}{\xi} + \frac{1}{L_a} + \frac{\chi}{L}\right), \tag{4}$$

where ξ is the interference scale in the medium and the parameter χ represents the effect of the sample geometry on radiation transfer. For a cubic sample with side L, $\chi = 1$, whereas for a layer with thickness L, $\chi < 1$ due to the contribution of the scattered-field components propagating in the layer in the transverse direction [8]. The parameter ξ is determined as $l^{*2}/(l^* - l_c^*)$, where $l_c^* = k^{-1}$ is the critical transport length. For $l^* \longrightarrow l_c^*$ in the nonabsorbing medium ($L_a = \infty$ and $L \gg l^*$), $\tilde{l}^* \longrightarrow 0$. This effect is manifested at the macroscopic level as a change in the dependence of T on L. Far from the localization threshold, $\tilde{l}^* \approx l^*$ and $T \propto L^{-1}$, whereas $T \propto L^{-2}$ at the threshold. For $\xi > l^*$, the renormalization effect on the "macroscopic" dependence $T = f(L)$ can be studied by analyzing the logarithmic derivative $\beta = d(\ln T)/d(\ln L)$. Substituting Eq. (4) into Eq. (2) and after some algebra, we arrive at the expression

$$\beta = -\left\{1 + \frac{l^{*2}}{L^2}(1 + \eta L)(z_{01} + z_{02})\right\}^{-1} - \left\{(1 + \eta L)\left[1 + \frac{l^{*2}}{L^2}(1 + \eta L)(z_{01} + z_{02})\right]\right\}^{-1}, \tag{5}$$

where $\eta = (1/\xi + 1/L_a)/\chi$. For a layer with $L \gg l^*$ and $L_a \longrightarrow \infty$, we obtain $\beta \longrightarrow -2$ for $\beta \longrightarrow 0$ ($l^* \longrightarrow l_c^*$), whereas $\beta \approx -1$ for large η values (classical radiation diffusion). The behavior of the parameter $\Delta\tilde{\beta}/\Delta\lambda\tilde{\beta}$ for the $T(\lambda_0)$ spectra is analyzed as a function of the layer thickness: for a given λ_0 value, $\tilde{\beta}$ is determined from the $T(\lambda_0)$ spectra for the samples with close L_1 and L_2 values ($L_1, L_2 \gg |L_1 - L_2|$) as $\tilde{\beta} = \ln(T_2/T_1)/\ln(L_2/L_1)$. The normalized spectral slope $\Delta\tilde{\beta}/\Delta\lambda\tilde{\beta}$ is determined for the narrow spectral interval $\Delta\lambda = 20$ nm near $\lambda_0 =$ 475 m. Figure 4 shows $|\Delta\tilde{\beta}/\Delta\lambda\tilde{\beta}|$ as a function of $\tilde{L} = (L_1 + L_2)/2$. This dependence illustrates the transitions between various regimes of radiation transfer in the layer with finite absorption and for $\xi > l^*$. According to Eq. (5), the interference effect on radiation transfer is noticeable for small L values and becomes insignificant as the layer thickness increases. For classical radiation diffusion ($T \propto L^{-1}$), $d\beta/\beta d\lambda = 0$. For $L > L_a$, absorption governs radiation transfer in the layer, $T \propto \exp(-L/L_a)$, and $d\beta/\beta d\lambda = dL_a/L_a d\lambda$ (is independent of L). The regions corresponding to various regimes of radiation transfer are separated in Fig. 4 as follows. Region *3* corresponds to the diffusion of light that is governed by absorption for $\tilde{L} > L_a$ (L_a for the samples under investigation and for $\lambda_0 = 475$ nm is estimated as 45 μm. Region *2* corresponds to the transition to the $T \propto L^{-1}$ regime of the classical diffusion of radiation for $\tilde{L} < L_a$. In our opinion, region *1* corresponds to the transition to scale-dependent diffusion for $\tilde{L} \sim \eta^{-1}$.

Using the results for $\lambda_0 = 473$–500 nm, the η value for $\lambda_0 = 475$ nm is estimated as 0.8 ± 0.4 μm^{-1}, which gives a value of 1.2 ± 0.6 μm for the interference scale in the scattering medium and corresponds to a fairly large renormalization factor ($\chi\xi$ is at least six times as large as l^*). It is useful to compare the result with the data of the pulse modulation measurements of the light diffusion coefficient in layers of anatase particles with $\bar{a} = 0.3$ μm and $p = 0.5$–0.7 [27]. The maximum renormalization factor ≈2.8 is obtained for $\lambda_0 = 514$ nm. As compared to the experimental results reported in [27], much higher efficiency of light scattering in the short-wavelength region (near low-order Mie resonances) is expected in our case due to a higher n_{sc} value for rutile as compared to anatase and a lower p value (the p value corresponding to the maximum l and l^* values for close packed media lies in the range 0.25–0.4 [21]).

Until recently, the main direction of achieving the localization threshold in randomly inhomogeneous media was the use of powder semiconductors (Si, Ge, GaAs, etc.) in the IR range far from the absorption bands of materials (see, e.g., [8, 12, 13, 28, 29]). In this case, low k values can be reached at a high efficiency of scattering due to high n_{sc} values. The results obtained above show that kl^* values close to the threshold value are reached in the short-wavelength region of the visible range (where k values are sufficiently high) near the absorption edge of the material of scattering particles (the maximum absorption for rutile corresponds to $\lambda_0 \approx$ 282 nm [22]). A sharp decrease in kl^* with λ_0 is caused by an increase in n_{sc} near the region of the anomalous dispersion of rutile (the maximum value $n_{\mathrm{TiO_2}} \approx 5.35$ is reached for $\lambda_0 \approx 322$ nm [22]). An increase in the scattering efficiency in the region of a sharp increase in n_{sc} can be provided by choosing the parameters of the size distribution of the particles ($\bar{a}$ and δ_a). It is worth noting that the effect of the scale-dependent diffusion of light, which is manifested for the samples under investigation in the short-wavelength region, is expected to significantly affect the formation of the transmission edge of scattering media based on TiO_2 particles.

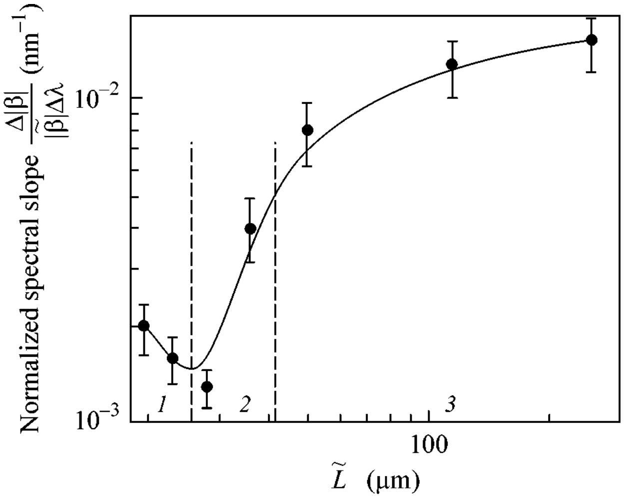

Fig. 4. Normalized spectral slope $|\Delta\tilde{\beta}/(\Delta\lambda\tilde{\beta}|$ vs. $\tilde{L}$. The solid line is the B-spline approximation of the data. For regions 1–3, see the text.

This work was supported by the Russian Foundation for Basic Research (project no. 04-02-16533). We are grateful to V.I. Kochubeĭ for assistance in spectral measurements.

REFERENCES

1. V. S. Letokhov, Zh. Éksp. Teor. Fiz. **53**, 1442 (1967) [Sov. Phys. JETP **26**, 835 (1968)].
2. N. M. Lawandy, R. M. Balachandaran, A. S. L. Gomes, and E. Sauvain, Nature **368**, 436 (1994).
3. C. Van Soest, F. J. Poelwijk, R. Sprik, and A. Lagendijk, Phys. Rev. Lett. **86**, 1522 (2001).
4. A. F. Ioffe and A. R. Regel, Prog. Semicond. **4**, 237 (1960).

5. A. Isimaru, *Wave Propagation and Scattering in Random Media* (Academic, New York, 1978; Mir, Moscow, 1981).
6. S. Chandrasekhar, *Radiative Transfer*, 2nd ed. (Dover, New York, 1960; Inostrannaya Literatura, Moscow, 1953).
7. N. Garcia, A. Z. Genack, and A. A. Lisyansky, Phys. Rev. B **46**, 14475 (1992).
8. J. G. Rivas, R. Sprik, A. Lagendijk, *et al.*, Phys. Rev. E **63**, 046613 (2001).
9. R. Berkovits and M. Kaveh, Phys. Rev. B **36**, 9322 (1987).
10. B. A. van Tiggelen, A. Lagendijk, and D. S. Wiersma, Phys. Rev. Lett. **84**, 4333 (2000).
11. E. Abrahams, P. W. Anderson, D. C. Licciardello, and T. V. Ramakrishnan, Phys. Rev. Lett. **42**, 673 (1979).
12. D. S. Wiersma, P. Bartolini, A. Lagendijk, and R. Righini, Nature **390**, 671 (1997).
13. F. Scheffold, R. Lenke, R. Tweer, and G. Maret, Nature **398**, 206 (1999).
14. A. Z. Genack and N. Garcia, Phys. Rev. Lett. **66**, 2064 (1991).
15. Z. Q. Zhang, C. C. Wong, K. K. Fung, *et al.*, Phys. Rev. Lett. **81**, 5540 (1998).
16. F. J. P. Schuurmans, M. Megens, D. Vanmaekelbergh, and A. Lagendijk, Phys. Rev. Lett. **83**, 2183 (1999).
17. C. M. Soukoulis, S. Datta, and E. N. Economou, Phys. Rev. B **49**, 3800 (1994).
18. K. Busch and C. M. Soukoulis, Phys. Rev. Lett. **75**, 3442 (1995).
19. K. Busch and C. M. Soukoulis, Phys. Rev. B **54**, 893 (1996).
20. C. F. Bohren and D. R. Huffman, *Absorption and Scattering of Light by Small Particles* (Wiley, New York, 1983; Mir, Moscow, 1986).
21. K. Busch, C. M. Soukoulis, and E. N. Economou, Phys. Rev. B **50**, 93 (1994).
22. http://www.ioffe.ru/SVA/NSM/nk/Oxides/Gif/tio2.gif.
23. http://www.almazoptics.com/TiO2.htm.
24. B. P. J. Bret and A. Lagendijk, Phys. Rev. E **70**, 036601 (2004).
25. J. X. Zhu, D. J. Pine, and D. A. Weitz, Phys. Rev. A **44**, 3948 (1991).
26. F. C. MacKintosh and S. John, Phys. Rev. B **37**, 1884 (1988).
27. J. M. Drake and A. Z. Genack, Phys. Rev. Lett. **63**, 259 (1989).
28. J. G. Rivas, R. Sprik, C. M. Soukoulis, *et al.*, Europhys. Lett. **48**, 22 (1999).
29. J. G. Rivas, R. Sprik, A. Lagendijk, *et al.*, Phys. Rev. E **62**, R4540 (2000).

Translated by R. Tyapaev

JETP Letters, Vol. 82, No. 5, 2005, pp. 273–278. From Pis'ma v Zhurnal Éksperimental'noĭ i Teoreticheskoĭ Fiziki, Vol. 82, No. 5, 2005, pp. 306–311.

Original English Text Copyright © 2005 by Brodsky, Klaptsov, Kagan, Combescot, Leyronas.

Bound States of Three and Four Resonantly Interacting Particles[¶]

I. V. Brodsky[a], A. V. Klaptsov[b], M. Yu. Kagan[a], R. Combescot[c], and X. Leyronas[c]
[a] *Kapitza Institute for Physical Problems, Russian Academy of Sciences, Moscow, 119334 Russia*
e-mail: kagan@kapitza.ras.ru
[b] *Russian Research Centre Kurchatov Institute, Moscow, 123182 Russia*
[c] *Laboratoire de Physique Statistique, Ecole Normale Superieure, 75231 Paris Cedex 05, France*

Received July 12, 2005

We present an exact diagrammatic approach for the problem of dimer–dimer scattering in 3D for dimers being a resonance bound state of two fermions in a spin-singlet state, with corresponding scattering length a_F. Applying this approach to the calculation of the dimmer–dimer scattering length a_B, we recover exactly the already known result $a_B = 0.6\,a_F$. We use the developed approach to obtain new results in 2D for fermions and bosons. Namely, we calculate bound state energies for three *bbb* and four *bbbb* resonantly interacting bosons in 2D. For the case of resonance interaction between fermions and bosons, we exactly calculate bound state energies of the following complexes: two bosons plus one fermion *bbf*, two bosons plus two fermions $bf_\uparrow bf_\downarrow$, and three bosons plus one fermion *bbbf*. *© 2005 Pleiades Publishing, Inc.*

PACS numbers: 61.72.Cc, 61.80.Az, 61.82.Ms

1. INTRODUCTION

The physics of ultracold Fermi gases has been the subject of intensive investigations in recent years. In particular, the possibility of experimental observation of the crossover from the BCS to BEC limit due to Feshbach resonance is being actively discussed. In the vicinity of the resonance, the scattering length is very large, being positive on one side of the resonance and negative on the other side. In the limit of the positive scattering length for two fermions, the formation of weakly bound dimers consisting of two different fermions becomes energetically favorable. Far from the resonance on the positive side, a weakly interacting gas of these composite bosons exists. In this paper, we present a diagrammatic approach to an exact solution for dimmer–dimer elastic scattering, assuming that the (positive) scattering length greatly exceeds the characteristic radius r_0 of interaction between atoms (the so-called resonance approximation). As was first shown by Skorniakov and Ter-Martirosian [1], in the case of the three-body fermionic problem, the scattering length of a fermion on a weakly bound dimer is determined by a single parameter, the two-body scattering length a_F, and is equal to $1.18a_F$ in the zero-range approximation for the interatomic potential. The same situation holds in the case of the fermionic four-body problem, where the dimmer–dimer scattering amplitude is fully determined by the value of a_F.

In the first study of the crossover problem by Haussmann [2], the scattering length of composite bosons a_B was found in the lowest order (Born approximation) and is equal to $2a_F$. Later, Pieri and Strinati [3], using a diagrammatic approach, greatly improved this result and found that in the ladder approximation the scattering length of composite bosons is approximately equal to $0.75a_F$. However, the ladder approximation, strictly speaking, is not valid, because it misses an infinite number of diagrams, which give a contribution of the same order of magnitude as those taken into account. Recently, Petrov, Salomon, and Shlyapnikov [4] have found the exact value of the scattering length of composite bosons $a_B = 0.6a_F$. They solved the Schrödinger equation using the well-known method of pseudopotentials. Below we show an exact solution of the scattering problem of two weakly bound dimers using the diagrammatic approach in the resonance approximation.

We use the developed approach to obtain new results for two different systems in the 2D case. Namely, we consider first a system of resonantly interacting bosons. We calculate exactly the three boson *bbb* and four boson *bbbb* bound state energies in this case. We also apply our approach to the 2D system of bosons resonantly interacting with fermions. Here we calculate exactly the bound state energies for the following complexes: two bosons plus one fermion *bbf*, two bosons plus two fermions $bf_\uparrow bf_\downarrow$, and three bosons plus one fermion *bbbf*.

This paper is a natural continuation of our previous results, where we predicted the possibility of two-fermion *ff* [5, 6] and two-boson *bb* [7] pairing, as well as composite fermion creation *fb* [8] in resonantly inter-

---

[¶] The text was submitted by the authors in English.

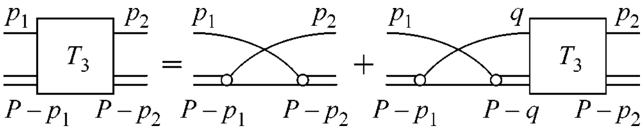

Fig. 1. Graphic representation of the equation for the full dimmer–fermion scattering vertex T_3.

acting ($a \gg r_0$) 2D Fermi–Bose gases and Fermi–Bose mixtures.

2. THREE-PARTICLE SCATTERING

As a preliminary exercise, we will rederive the result of Skorniakov and Ter-Martirosian for dimer–fermion scattering length using the diagrammatic method [9].

Following Skorniakov and Ter-Martirosian in the presence of the weakly bound resonance level $-|E_b|$ in a two-particle cross section, we can limit ourselves to the zero-range interaction potential between fermions. A two-fermion vertex can be approximated by a simple one-pole structure, which reflects the presence of the s-wave resonance level in a spin-singlet state:

$$\begin{aligned} T_{2\alpha\beta;\,\gamma\delta}(P) &= T_2(P)(\delta_{\alpha,\gamma}\delta_{\beta,\delta}-\delta_{\alpha,\delta}\delta_{\beta,\gamma}) \\ &= T_2(P)\chi(\alpha,\beta)\chi(\gamma,\delta), \end{aligned} \quad (1)$$

$$T_2(P) = \frac{4\pi}{m^{3/2}}\frac{\sqrt{|E_B|}+\sqrt{\mathbf{P}^2/4m-E}}{E-\mathbf{P}^2/4m+|E_B|},$$

where $P = \{E, \mathbf{P}\}$, E is the total energy and $\mathbf{P}$ is the total momentum of incoming particles, m is the fermionic mass, $|E_B| = 1/ma_F^2$. Indices α, β and γ, δ denote spin states of incoming and outgoing particles. The function $\chi(\alpha,\beta)$ stands for the spin singlet state, $\chi(\alpha,\beta) = \delta_{\alpha,\uparrow}\delta_{\beta,\downarrow}-\delta_{\alpha,\downarrow}\delta_{\beta,\uparrow}$.

The simplest process that contributes to dimer–fermion interaction is the exchange of a fermion. We will denote it as Δ_3. Its analytical expression is

$$\Delta_{3\alpha,\beta}(p_1, p_2; P) = -\delta_{\alpha,\beta}G(P-p_1-p_2), \quad (2)$$

where $G(p) = 1/(\omega - \mathbf{p}^2/2m + i0)$ is a bare fermion Green's function. The minus sign on the right hand side of Eq. (2) comes from the permutation of two fermions. In order to obtain a full dimer–fermion scattering vertex T_3, we need to build a ladder from Δ_3 blocks. One can easily verify that the spin projection is conserved in every order of T_3 and thus $T_{3\alpha,\beta} = \delta_{\alpha,\beta}T_3$. An equation for T_3 will have the diagrammatic representation shown in Fig. 1, and in analytical form it is written as

$$\begin{aligned} T_3(p_1, p_2; P) &= -G(P-p_1-p_2) \\ &-i\sum_q G(P-p_1-q)G(q)T_2(P-q)T_3(q, p_2; P), \end{aligned} \quad (3)$$

where $\sum_q \equiv \int d^3q\,d\Omega/(2\pi)^4$. We can integrate out the frequency Ω in Eq. (3) by closing the integration contour in the lower half-plane, since both $T_2(P-q)$ and $T_3(q, p_2; P)$ are analytical functions in this region. Moreover, if we are interested in the low-energy s-wave dimmer–fermion scattering length a_3, we can safely put $P = \{E, \mathbf{P}\} = \{-|E_b|, 0\}$ and $p_2 = 0$. The full vertex T_3 is connected with a_3 by the following relation:

$$\left(\frac{8\pi}{m^2a_F}\right)T_3(0, 0; -|E_b|) = \frac{3\pi}{m}a_3. \quad (4)$$

Introducing a new function $a_3(\mathbf{k})$ according to the formula

$$\left(\frac{8\pi}{m^2a_F}\right)T_3(\{k^2/2m, \mathbf{k}\}, 0; -|E_b|) = \frac{3\pi}{m}a_3(\mathbf{k}) \quad (5)$$

and substituting it in Eq. (3), we obtain the Skorniakov–Ter-Martirosian equation for the scattering amplitude:

$$\begin{aligned} \frac{3/4a_3(\mathbf{k})}{\sqrt{m|E_B|}+\sqrt{3k^2/4+m|E_B|}} &= \frac{1}{k^2+m|E_b|} \\ &-4\pi\int\frac{a_3(\mathbf{q})}{q^2(k^2+q^2+\mathbf{kq}+m|E_b|)}\frac{d^3q}{(2\pi)^3}. \end{aligned} \quad (6)$$

Solving this equation, one obtains the well-known result for dimer–fermion scattering length $a_3 = a_3(0) = 1.18a_F$.

3. DIMER–DIMER SCATTERING

Now we can proceed to the problem of dimer–dimer scattering. This problem was previously solved by Petrov *et al.* [4] by studying the Shrödinger equation for a 4-fermion wave function.

Inspired by the work of Petrov *et al.* [4] we are looking for a special vertex, which describes an interaction of two fermions constituting a first dimer with a second dimer as a single object. An obvious candidate for this vertex would be the sum of all diagrams with two fermionic and one dimer incoming line. It would be natural to suppose that these diagrams should have the same set of outgoing lines—two fermionic and one dimmer. However, in this case there will be a whole set of disconnected diagrams contributing to our sum that describes the interaction of a dimer with only one fermion. As was pointed out by Weinberg [10], one can construct a good integral equation of the Lippmann–Schwinger type only for a connected class of diagrams. Thus far, we have been forced to give attention to the vertex $\Phi_{\alpha\beta}(q_1, q_2; p_2, P)$ corresponding to the sum of all diagrams with one incoming dimer line, two incoming fermionic lines, and two outgoing dimer lines (see Fig. 2). This vertex $\Phi_{\alpha\beta}(q_1, q_2; p_2, P)$ is rather straight-

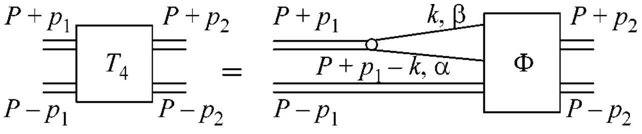

Fig. 2. Vertex Φ represents the full dimer–dimer scattering matrix T_4 with one dimer line being cut.

forwardly related to the standard dimer–dimer scattering vertex $T_4(p_1, p_2; P)$:

$$T_4(p_1, p_2; P) = \frac{i}{2}\sum_{k;\,\alpha,\,\beta}\chi(\alpha, \beta)G(P+p_1-k) \times G(k)\Phi_{\alpha\beta}(P+p_1-k, k;\, p_2, P). \qquad (7)$$

Note that, by definition, in any order of interaction Φ contains only connected diagrams.

The spin part of the vertex $\Phi_{\alpha,\,\beta}$ has the simple form $\Phi_{\alpha,\,\beta}(q_1, q_2; P, p_2) = \chi(\alpha, \beta)\Phi(q_1, q_2; P, p_2)$. A diagrammatic representation of the equation on Φ is given in Fig. 3. One can assign some a physical meaning to the processes described by these diagrams. The diagram of Fig. 3a represents the simplest exchange process in dimmer–dimer interaction. The diagram of Fig. 3b accounts for the more complicated nature of a "bare" (irreducible by two dimer lines) dimmer–dimer interaction. Finally, the diagram in Fig. 3c allows for multiple dimer–dimer scattering via a bare interaction. The last term in Fig. 3 means that we should add another three diagrams analogous to Figs. 3a, 3b, and 3c, but with two incoming fermions (q_1 and q_2) exchanged. The analytical equation for the vertex Φ can be written as

$$\begin{aligned}\Phi(q_1, q_2;\, p_2, P) &= -G(P-q_1+p_2)G(P-q_2-p_2)\\ &-i\sum_k G(k)G(2P-q_1-q_2-k)T_2(2P-q_1-k)\\ &\times\Phi(q_1, k;\, p_2, P) + \frac{1}{2}\sum_{Q,\,k} G(Q-q_1)G(2P-Q-q_2)\\ &\times T_2(2P-Q)T_2(Q)G(k)G(Q-k)\Phi(k, Q-k;\, p_2, P)\\ &+ (q_1 \longleftrightarrow q_2).\end{aligned} \qquad (8)$$

Since we are looking for s-wave scattering length, we can put $p_2 = 0$ and $P = \{0, -|E_B|\}$. At this point we have a single closed equation on the vertex Φ in the momentum representation, which, we believe, is analogous to the equation of Petrov *et al.* in the coordinate representation. To make this analogy more prominent, we have to exclude frequencies from the equation. However, this exclusion is rather cumbersome and we leave it for a more extended publication.

The dimer–dimer scattering length is proportional to the full symmetrized vertex $T_4(p_1, p_2; P)$:

$$\left(\frac{8\pi}{m^2 a_F}\right)^2 T_4(0, 0; -2|E_b|, 0) = \frac{2\pi(2a_B)}{m}. \qquad (9)$$

If one skips the second term in Eq. (8), i.e., omits the diagram in Fig. 3b, one arrives at the ladder approximation of Fieri and Strinati. The exact equation (8) corresponds to the summation of all diagrams. We have calculated the scattering length in the ladder approximation and the scattering length derived from the exact equation and obtained $0.78a_F$ and $0.6a_F$, respectively. Thus, our results in the ladder approximation are in agreement with the results of Pieri *et al.* [3] and in the general form with the results of Petrov *et al.* [4]. Note also that our approach allows one to find the dimmer–dimer scattering length in the 2D case (this problem was previously solved by Petrov *et al.* [11]).

Finally, we would like to mention that our results allow one to find the fermionic Green's function, chemical potential, and sound velocity as a function of a_F in the case of the dilute superfluid bose gas of dimers at low temperatures. The problem of dilute superfluid bose gas of di-fermionic molecules was solved by Popov [12] and later deeply investigated by Keldysh and Kozlov [13]. Those authors managed to reduce the gas problem to a dimer–dimer scattering problem in vacuum but were unable to express the dimmer–dimer scattering amplitude in a single two-fermion parameter. A direct combination of our results with those ones of Popov, Keldysh, and Kozlov allows one to get all the thermodynamic values of a dilute superfluid resonance gas of composite bosons. However, a more interesting subject for the application of our results is the high-temperature expansion for the thermodynamic potential and sound velocity in the temperature region $T \sim T_* \sim |E_B|$, where composite bosons start to appear.

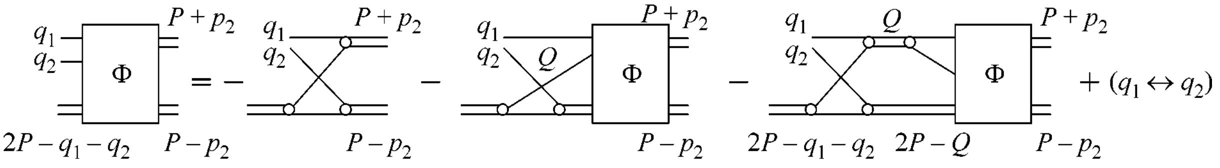

(a) (b) (c)

Fig. 3. Graphic representation of the equation on function Φ describing dimer–dimer scattering.

4. NEW RESULTS IN THE 2D CASE

As was first shown by Danilov [14] (see also the paper of Minlos and Fadeev [15]) in the 3D case, the problem of three resonantly interacting bosons cannot be solved in the resonance approximation. This statement stems from the fact that in the case of identical bosons the homogeneous part of Skorniakov–Ter-Martirosian equation (6) has a nonzero solution at any negative energies. The physical meaning of this mathematical artifact was elucidated by Efimov, who showed that a two-particle interaction leads to the appearance of an attractive $1/r^2$ interaction in a three-body system. Since, in the attractive $1/r^2$ potential in 3D, a particle falls to the center, short-range physics is important and one cannot replace the exact pair interaction by its resonance approximation.

In contrast, in the case of the 2D problem, the phenomenon of the particle falling to the center is absent, and one can utilize the resonance approximation [16]. Therefore, it is possible to describe three- and four-particle processes in terms of the two-particle binding energy $|E_B| = 1/ma^2$ only (below, for simplicity we will assume that all particles under consideration have the same mass m). We will omit the problem of composite particles\ scattering and will mainly concentrate on the problem of the binding energies of the complexes of three and four particles.

As in the 3D case, the cornerstone in the diagrammatic technique is the two-particle resonance scattering vertex T_2. For two resonantly interacting particles with total mass $2m$, it can be written in 2D as

$$T_2(P) = -\frac{4\pi}{m}\frac{\alpha}{\ln(\{\mathbf{P}^2/4m - E\}/|E_B|)}, \qquad (10)$$

where we introduce the factor $\alpha = \{1, 2\}$ in order to take into account whether or not two particles are indistinguishable. It is $\alpha = 2$ for the case of resonance interaction between identical bosons and $\alpha = 1$ for the case of resonance interaction between fermion and boson or for the case of two distinguishable bosons.

4.1. Three Particles in 2D

We start with a system of three resonantly interacting identical bosons—*bbb*—in 2D. The equation for the dimmer–boson scattering vertex T_3, which describes interaction of three bosons, has the same diagrammatic form as shown in the Fig. 1; however the rules of its analytical notation are changed. It can be written as

$$T_3(p_1, p_2; P) = G(P - p_1 - p_2) + i\sum_q G(P - p_1 - q) \times G(q)T_2(P - q)T_3(q, p_2; P), \qquad (11)$$

where $\sum_q \equiv \int d^3q d\Omega/(2\pi)^3$, $P = \{0, E\}$, and one should put $\alpha = 2$ for the two-particle vertex T_2 in Eq. (10). The opposite signs in Eq. (3) for fermions and Eq. (11) for bosons are due to the permutational properties of the particles involved: an exchange of fermions results in a minus sign, while an analogous exchange of bosons brings no extra minus. Finally we note that the three-particle s-wave (s-wave channel of boson–dimer scattering) binding energies E_3 correspond to the poles in $T_3(0, 0; -|E_3|)$ and, consequently, at energies $E = E_3$ the homogeneous part of Eq. (11) has a nontrivial solution. Solving Eq. (11), we find that a complex of three identical bosons has two s-wave bound states $E_3 = 16.52E_B$ and $E_3 = 1.267E_B$ in accordance with the previous results of Bruch and Tjon [16, 17].

Let us now consider a complex—*fbb*—consisting of one fermion and two bosons. As noted above, we consider bosons and fermions with equal masses $m_b = m_f = m$. We assume that a fermion–boson interaction U_{fb}, characterized by the radius of interaction r_{fb}, yields a resonance two-body bound state with an energy $E = -|E_B|$. At the same time, a boson–boson interaction U_{bb}, characterized by the interaction radius r_{bb} does not yield a resonance. Hence, if we are interested in low-energy physics, the only relevant interaction is U_{fb}, and we can ignore the boson–boson interaction U_{bb}, the latter would give small corrections on the order of $|E_B|mr_{bb}^2 \ll 1$ at low energies. In order to determine three-particle bound states, one has to find poles in the dimmer–boson scattering vertex T_3. Since we neglect boson–boson interaction U_{bb}, the vertex T_3 is described by the same diagrammatic equation of Fig. 1 as in the problems of three bosons. The analytical form of this equation also coincides with Eq. (11), with the minor correction that the resonance scattering vertex T_2 now corresponds to the interaction between a boson and a fermion and, therefore, we should put $\alpha = 1$ in Eq. (10) for T_2. Solving the equation for T_3, we find that the *fbb* complex has only one s-wave bound state with the energy $E_3 = 2.39E_B$.

Note that a complex—*bff*—consisting of a boson and two spinless identical fermions (or a complex $bf_\uparrow f_\downarrow$ of a boson and spin ↑ and spin ↓ fermions) with the resonance interaction U_{fb} does not have any three-particle bound states.

4.2. Four Particles in 2D

After solving the above three-particle problems, we may proceed to complexes consisting of four particles. First we will consider four identical resonantly interacting bosons *bbbb* [18]. Any two bosons would form a stable dimer with a binding energy $E = -|E_B|$. We are going to find a four-particle binding energy as the energy of an s-wave bound state of two dimers. Generally speaking, bound states could emerge in channels with larger orbital momenta; however, this question will be the subject of further investigations. To find the binding energy, we should examine the analytical structure of the dimer–dimer scattering vertex T_4 and find its poles. The set of equations for T_4 has the same diagrammatic structure as those shown in Figs. 2 and 3. The analytical expression of the first equation can be written as

$$\begin{gathered} T_4(p_1, p_2; P) = \frac{i}{\alpha}\sum_k G(P+p_1-k)G(k) \\ \times \Phi(P+p_1-k, k; p_2, P), \end{gathered} \tag{12}$$

and the equation for the vertex Φ is

$$\begin{gathered} \Phi(q_1, q_2; p_2, P) = G(P-q_1+p_2)G(P-q_2-p_2) \\ + i\sum_k G(k)G(2P-q_1-q_2-k)T_2(2P-q_1-k) \\ \times \Phi(q_1, k; p_2, P) \\ - \frac{1}{2\alpha}\sum_{Q,k} G(Q-q_1)G(2P-Q-q_2) \\ \times T_2(2P-Q)T_2(Q)G(k)G(Q-k)\Phi(k, Q-k; p_2, P) \\ + (q_1 \longleftrightarrow q_2), \end{gathered} \tag{13}$$

where T_2 should be taken from Eq. (10) and one should put $\alpha = 2$ for the case of identical resonantly interacting bosons. Solving the above equations for the poles of T_4 as a function of the variable $P = \{0, E\}$, we found 2 bound states for the *bbbb* complex (see table). Certainly, for the validity of our approximation we should have $|E_4| \ll 1/mr_0^2$. For the case of four bosons *bbbb*, this means that $194|E_b| \ll 1/mr_0^2$ and, hence, $a/r_0 \gg \sqrt{194}$. This case can still be realized in the Feshbach resonance scheme.

The case of a four-particle complex $bf_\uparrow bf_\downarrow$ consisting of resonantly interacting bosons and fermions is described by the same equations (12, 13) but with the parameter $\alpha = 1$. In this case, we found two bound states; they are also listed in the table.

In order to obtain bound states of the *fbbb* complex, one has to find energies $P = \{0, E\}$ corresponding to nontrivial solutions of the following homogeneous equation:

$$\begin{gathered} \Phi(q_1, q_2; p_2, P) = i\sum_k G(k)G(2P-q_1-q_2-k) \\ \times T_2(2P-q_1-k)\Phi(q_1, k; p_2, P) + (q_1 \longleftrightarrow q_2). \end{gathered} \tag{14}$$

This equation corresponds to the diagrams of Fig. 3b. We found a bound state of the *fbbb* complex with energy $E_4 = 4.10E_B$.

Bound states of resonantly interacting particles in 2D

System	Relative[1] interaction	Number of bound states	Energy (in E_B)[2]	α[3]
bbb	U_{bb}	2	1.267, 16.52	2
fbb	U_{fb}	1	2.39	1
fbbb	U_{fb}	1	4.10	1
$bf_\uparrow bf_\downarrow$	U_{fb}	2	2.84, 10.64	1
bbbb	U_{bb}	2	24, 194	2

[1] Interaction that yields resonance scattering. All other interactions are negligible.

[2] $m = m_b = m_f$.

[3] The indistinguishability parameter in Eq. (10).

Finally, we summarize the results concerning binding energies of three and four resonantly interacting particles in 2D in the table. Note that all our calculations correspond to the case of particles with equal masses $m_f = m_b = m$, though they can be easily generalized to the case of different masses.

5. CONCLUSIONS

For the problem of resonantly interacting fermions in 3D, we developed an exact diagrammatic approach that allows the dimmer–dimer scattering length to be found. We apply the developed approach to obtain new results in the 2D case. Namely, we exactly calculate the binding energies of the following complexes: three bosons *bbb*, two bosons plus one fermion *bbf*, three bosons plus one fermion *bbbf*, two bosons plus two fermions $bf_\uparrow bf_\downarrow$, and four bosons *bbbb*.

Our investigations enrich the phase diagram of ultracold Fermi–Bose gases with resonance interaction. They serve as an important step for future calculations of the thermodynainic properties and the spectrum of collective excitations in different temperature and density regimes. Note that, in purely bosonic models in 2D or in the Fermi–Bose mixtures in the case of prevailing density of bosons $n_B > n_F$, creation of larger complexes consisting of 5, 6, or more particles is also possible. In fact, here we are dealing with the macroscopic phase separation (with the creation of large droplets). The radius of this droplet R_N for N bosons in 2D is estimated in [18] on the basis of a variational approach. Note that even for $N = 5$ the exact calculation of the bound state energies requires huge computational capability, which is why it was not performed by us.

This work was supported by the Russian Foundation for Basic Research (project no. 04-02-16050), the US Civilian Research and Development Foundation (grant no. RP2-2355-MO-02), and a grant of the Russian Ministry of Science and Education. We are grateful to A.F. Andreev, I.A. Fomin, P. Fulde, Yu. Kagan, L.V. Keldysh, Yu.E. Lozovik, S.V. Maleev, B.E. Meierovich, A.Ya. Parshin, P. Pieri, L.P. Pitaevskii, T.M. Rice, V.N. Ryzhov, G.V. Shlyapnikov, G.C. Strinati, V.B. Timofeev, D. Volhardt, and P. Wölfle for fruitful discussions. M.Yu.K. is grateful to the University Pierre and Marie Curie for hospitality during the first stage of this work.

REFERENCES

1. G. V. Skorniakov and K. A. Ter-Martirosian, Zh. Éksp. Teor. Phys. **31**, 775 (1956) [Sov. Phys. JETP **4**, 648 (1957)].
2. R. Haussmann, Z. Phys. B: Condens. Matter **91**, 291 (1993).
3. P. Pieri and G. C. Strinati, Phys. Rev. B **61**, 15370 (2000).
4. D. S. Petrov, C. Salomon, and G. V. Shlyapnikov, Phys. Rev. Lett. **93**, 090 404 (2004).
5. M. Yu. Kagan and T. M. Rice, J. Phys.: Condens. Matter **6**, 3771 (1994).
6. M. Yu. Kagan, R. Fresard, M. Capezzali, and H. Beck, Phys. Rev. B **57**, 5995 (1998).
7. M. Yu. Kagan and D. V. Efremov, Phys. Rev. B **65**, 195103 (2002).
8. M. Yu. Kagan, I. V. Brodsky, D. V. Efremov, and A. V. Klaptsov, Phys. Rev. A **70**, 023607 (2004).
9. P. F. Bedaque and U. van Kolck, Phys. Lett. B **428**, 221 (1998).
10. S. Weinberg, Phys. Rev. B **133**, 232 (1964).
11. D. S. Petrov, M. A. Baranov, and G. V. Shlyapnikov, Phys. Rev. A **67**, 031601(R) (2003).
12. V. N. Popov, Zh. Éksp. Teor. Fiz. **50**, 1550 (1966) [Sov. Phys. JETP **23**, 1034 (1966)].
13. L. V. Keldysh and A. N. Kozlov, Zh. Éksp. Teor. Fiz. **54**, 978 (1968) [Sov. Phys. JETP **27**, 521 (1968)].
14. G. S. Danilov, Zh. Éksp. Teor. Fiz. **40**, 498 (1961) [Sov. Phys. JETP **13**, 349 (1961)].
15. R. Minlos and L. D. Fadeev, Zh. Éksp. Teor. Fiz. **41**, 1850 (1961) [Sov. Phys. JETP **14**, 1315 (1962)].
16. A. S. Jensen, K. Riisager, D. V. Fedorov, and E. Garrido, Rev. Mod. Phys. **76**, 215 (2004).
17. L. W. Bruch and J. A. Tjon, Phys. Rev. A **19**, 425 (1979).
18. H. Hammer and D. T. Son, Phys. Rev. Lett. **93**, 250408 (2004).

JETP Letters, Vol. 82, No. 5, 2005, pp. 279–283. From Pis'ma v Zhurnal Éksperimental'noĭ i Teoreticheskoĭ Fiziki, Vol. 82, No. 5, 2005, pp. 312–316.
Original English Text Copyright © 2005 by Arseyev, Maslova, Panov, Savinov, Van Haesendonck.

Identifying the Electronic Properties of the Ge(111)–(2 × 1) Surface by Low-Temperature Scanning Tunneling Microscopy[¶]

P. I. Arseyev[a], N. S. Maslova[b], V. I. Panov[b], S. V. Savinov[b], and C. Van Haesendonck[c]
[a] *Lebedev Physical Institute, Russian Academy of Sciences, Moscow, 119991 Russia*
[b] *Faculty of Physics, Moscow State University, Moscow, 119992 Russia*
e-mail: SavinovSV@mail.ru
[c] *Laboratory of Solid-State Physics and Magnetism, K.U. Leuven, B-3001 Leuven, Belgium*

Received July 6, 2005

We present the results of our low-temperature scanning tunneling microscopy (STM) investigation of the clean Ge(111) surface. Our experiments enable, for the first time, STM observation of one-dimensional surface screening around surface defects. We identify the dominating role of surface states in the low-temperature STM imaging as well as the important influence of nonequilibrium kinetics on the measured tunneling spectra.
© 2005 Pleiades Publishing, Inc.

PACS numbers: 68.35.Dv, 68.37.Ef, 73.20.At

The (111) surface of Ge is among the most widely studied elementary semiconductor surfaces. Some features of this surface are presently well established, e.g., the (2 × 1) surface reconstruction corresponding to a π-bonded chain model with buckling [1–3]. On the other hand, some properties still remain to be clarified. There is no clear understanding of the (2 × 1) reconstructed surface electronic properties, which should somehow reveal a one-dimensional (1D) character. In this work we present the results of our low-temperature scanning tunneling microscopy (STM) investigation of clean Ge(111)–(2 × 1) surfaces [4]. The samples under investigation were cut from heavily doped (resistivity 1 mΩ cm) Ge single crystals with *n*-type bulk conductivity. The doping element was phosphorus, which is a shallow impurity with an ionization energy of 13 meV, while the doping concentration was rather high, around 8×10^{18} cm^{-3}. The samples were $1.5 \times 1.5 \times 3.0$ mm^3 slabs with the long axis aligned along the [111] direction. Samples are cleaved *in situ* after the low-temperature STM instrument is cooled down to liquid-helium temperature. The details of the cleaving procedure and the experimental STM setup are described elsewhere [4]. After cleavage, the high-quality Ge(111) surface with pronounced optical reflectivity (mirror) is exposed to the STM tip for imaging and spectroscopy.

According to the commonly accepted point of view, the Ge(111) surface with (2 × 1) reconstruction is terminated by π-bonded chains with Ge atoms running along the $[01\bar{1}]$ direction [2], and only every second atomic chain is imaged as a protrusion by STM. The surface unit cell contains two atoms, both having one dangling bond, and these bonds are responsible for π bonding along zigzag rows. One atom (*up* atom) is shifted out of the surface, while the other atom (*down* atom) is shifted towards the surface. Consequently, the bonding surface states band π_{VB} derived from the *up*-atom orbital is filled, while the antibonding surface state band π^*_{CB} derived from the *down*-atom orbital is empty. At sufficiently high doping concentration, the anti-bonding surface states band π^*_{CB} is partially populated, and at the surface the Fermi level lies above the bottom of the π^*_{CB} band. The band structure for a heavily doped *n*-type Ge(111)–(2 × 1) surface, which is consistent with first-principles calculations [5], photoemission measurements [6], and our local tunneling spectroscopy data (see below), is illustrated in Fig. 1. Here we would like to mention some numbers characteristic of the Ge(111)–(2 × 1) surface. The widths of antibonding π^*_{CB} and bonding π_{VB} surface state bands which can be derived from both theoretical [5] and experimental [6] data are approximately equal to 1.2 and 0.8 eV, respectively. The value of the band gap on the E_{GS} surface measured by means of scanning tunneling spectroscopy at low temperature [7] is about 0.5 eV. The bulk band gap [8] equals 0.74 eV at liquid-helium temperature (4.2 K).

Typical STM images of the Ge(111)–(2 × 1) surface are presented in Fig. 2 for different values of the tunneling bias voltage applied to the sample (tip is grounded), which implies that filled (empty) state images are taken at negative (positive) bias. The first two images in

---

[¶] The text was submitted by the authors in English.

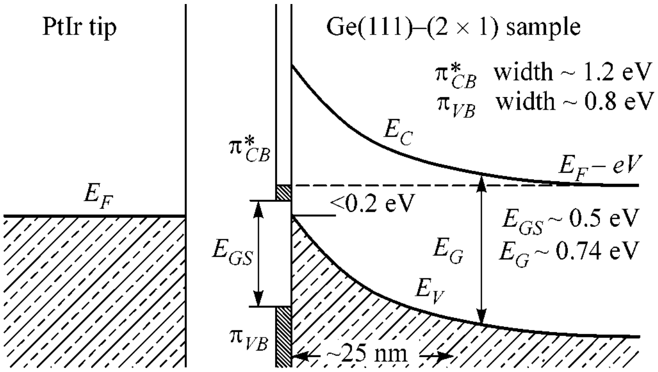

Fig. 1. Band structure of the metal tip—Ge(111)–(2 × 1) tunneling junction. π_{VB} and π^*_{CB} denote the bonding and antibonding surface states band, respectively. The partially filled surface-state antibonding (conduction) band is responsible for Fermi level pinning in the vicinity of the valence band maximum. The surface (E_{GS}) and bulk (E_G) band gaps are indicated. The figure is not to scale.

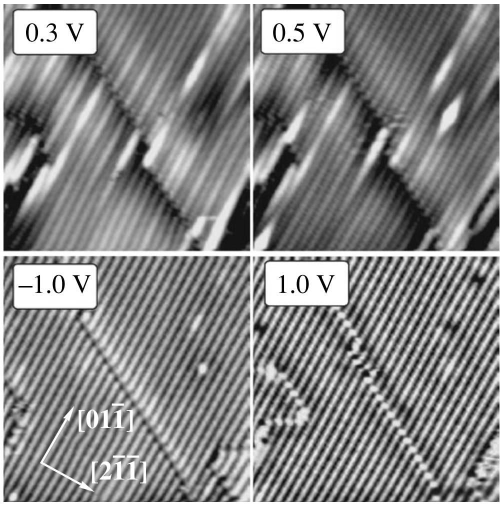

Fig. 2. STM images of the Ge(111)–(2 × 1) surface for different sample bias voltages. The set point for the tunneling current is 20 pA. The image size is 14 nm × 14 nm.

Fig. 2 were acquired with a bias voltage corresponding to the band gap region. All images reveal an ordered, chainlike surface structure. For the Ge(111) surface, such a chainlike structure has been attributed to a (2 × 1) surface reconstruction with π-bonded chains [2]. The images in Fig. 2 reveal the presence of surface defects, including the presence of ad-atoms on the surface.

We now turn to some remarkable features appearing in the Ge(111)–(2 × 1) surface STM images shown in Fig. 2. First, the images taken with a bias voltage corresponding to the band gap reveal the presence of screening of localized surface charges. The streaks observed in the STM images reflect the perturbation of the local density of states by the scattering on surface imperfections of electrons with 1D confinement along the π-bonded chain rows. STM images of all surface defects (impurities, ad-atoms, atomic size elements of domain boundaries) have a pronounced 1D shape. The areas around the defects appear as stripes with length up to 60 Å along the direction of the π-bonded chain rows ($[01\bar{1}]$ direction), while their width is approximately equal to the period of the surface reconstruction in the $[2\bar{1}\bar{1}]$ direction (about 7 Å). For an asymmetric defect such as a single atomic size element of a domain boundary, the stripe, which reflects the screening in the STM image, is asymmetric along the chain rows. While the screening cloud is localized mainly next to the defect, it smoothly decays in one direction with increasing distance from the domain boundary, but in the opposite direction it abruptly ends at the domain boundary. For symmetric defects such as individual surface impurity atoms or ad-atoms, the screening cloud has a symmetric shape along the chain row. We would like to stress that the contrast of the empty states STM images (positive sample bias voltages) is higher than for the filled states STM images (negative sample bias voltages). This can be accounted for by the different screening for empty and filled states, respectively (see below). It is also important to note that the low-temperature STM images of the Ge(111)–(2 × 1) surface become completely dominated by the density of surface electronic states for the range of bias voltages corresponding to the surface band gap.

We also experimentally probed the local density of electronic states. The results of scanning tunneling spectroscopy (STS) measurements are presented in Fig. 3. The normalized tunneling conductivity spectra were obtained by averaging the experimental data collected above a square surface area containing four π-bonded zigzag rows. The details of the data treatment procedure are described elsewhere [9]. The overall energy resolution for the present experiments is estimated to be 20 meV due to our numerical method of differentiation and subsequent averaging. This value is sufficiently small for reliable tunneling spectroscopy on semiconductors.

Let us now discuss the important features of the spectroscopic measurements on the Ge(111)–(2 × 1) atomically flat surface at low temperature. The presence of a band gap can be observed in the spectrum with bottom and top located at –0.07 V and +0.5 V, respectively. The Fermi level (0 V on the *V*-axis) is positioned in the spectrum slightly above the valence band maximum, although our samples are heavily doped and have *n*-type bulk conductivity. This can be accounted for by Fermi level pinning at the surface in the case of the Ge(111)–(2 × 1) surface (see Fig. 1). It is interesting to note that, for the Ge(111)–(2 × 1) surface, the position of the Fermi level in the tunneling spectra remains the same, independent of the type of doping of the bulk semiconductor, i.e., *p*-type or *n*-type bulk conductivity

[10]. According to photoemission data, the position is independent of the bulk doping concentration, as well [6]. The main source of the difference in tunneling spectra for the p-type and n-type Ge(111)–(2 × 1) surface is the difference in surface band bending. While for a n-type sample surface, band bending almost exceeds the bulk band gap value (Fig. 1), bands remain nearly flat near a p-type sample surface.

The tunneling current inside the bang gap is not negligible (see inset in Fig. 3). With our choice of the set point for the tunneling current ($I_t = 20$ pA), a comparable value of the tunneling current was detected throughout the band gap, except for a narrow region ($|V| <$ 0.1 V) around the Fermi level. This implies that the surface states are able to carry a current up to ~10^9 electrons per second. Hence, the tunneling rate through surface states is comparable to the relaxation rate of nonequilibrium electrons due to the eiectron–phonon interaction at low temperature (10^8 s^{-1} [11]). A local nonequilibrium charge can then be accumulated on the surface states, causing local band bending. This bending alters the ratio of the tunneling rates from surface states to the bulk semiconductor and to the metallic tip, respectively, and consequently alters the *measured* tunneling spectrum.

As can be seen in Fig. 3, the tunneling conductivity curve reaches an absolute minimum about 0.2 V above the Fermi level. Two other local minima followed by peaks are located on both sides of the surface band gap. A relatively weak peak is centered at –0.15 V near the valence band maximum. A strong peak with two shoulders on the high energy side can be found at 0.6 V, just below the conduction band minimum. The dips appearing at the band gap edges are characteristic for our experiments and are highly reproducible.

In order to understand the obtained experimental results, we rely on a model of resonant tunneling through surface state bands. The details of this model can be found in [12]. When the bias voltage is in the voltage range corresponding to the band gap, the coupling between surface and bulk states is very weak. As indicated in Fig. 1, a 250-Å-wide depletion layer separates the surface and bulk states. This depletion layer is formed because of charging of the surface states, which results in strong band bending near the surface. For heavy doping the Ge(111)–(2 × 1) surface band bending almost exceeds the band gap value (see Fig. 1). Consequently, correct modeling of tunneling processes through surface states requires that the STM junction be treated as a double barrier structure, and tunneling through the depletion layer needs to be taken into account.

Using the nonequilibrium Keldysh Green's function formalism, the local tunneling current can be determined [12]:

$$I(V, \mathbf{r}) = \int d\varepsilon \nu(\varepsilon, \mathbf{r})[n_t^0(\varepsilon) - n_b^0(\varepsilon)]\frac{\gamma_t(\varepsilon)\gamma_b(\varepsilon)}{\gamma_t(\varepsilon) + \gamma_b(\varepsilon)},$$

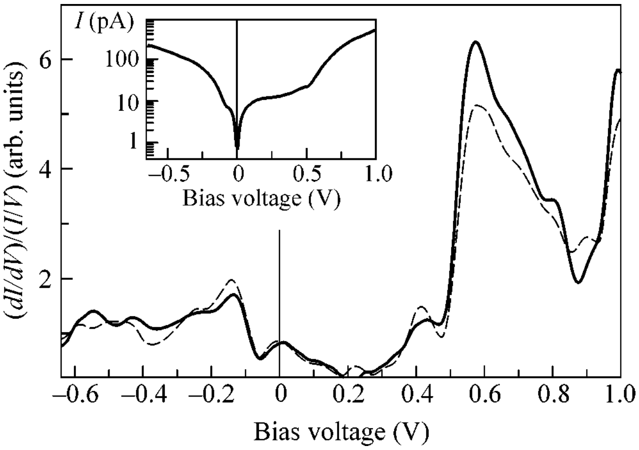

Fig. 3. $(dI/dV)/(I/V)$ normalized tunneling conductivity measured above two different defect free areas of the Ge(111)–(2 × 1) surface as a function of the applied bias voltage. The inset shows the logarithm of the current–voltage characteristic $I(V)$. The current set point for the measurements is $I_t = 20$ pA, while the voltage for the approach is $V_t = 0.3$ V.

where γ_t and γ_b are the tunneling rates from the surface states band to the metallic tip and to the bulk semiconductor, respectively. n_t^0 and n_b^0 are the equilibrium filling numbers of the metallic tip and the semiconductor, respectively, and $\nu(\varepsilon, \mathbf{r})$ is the local density of surface states. It is important to note that $\nu(\varepsilon, \mathbf{r})$ *is not* the density of defect-free surface states but includes contributions from surface defects of all kinds (impurity atoms, lattice vacancies, etc.).

We now turn in more detail to specific features of the tunneling current in the vicinity of a defect or individual impurity atom for small positive sample bias voltages. Because the empty surface state π_{CB}^* band is partially filled, the impurity potential is screened by surface electrons:

$$W_{\text{imp}}(\mathbf{q}) = \frac{W_0(\mathbf{q})}{\varepsilon(\mathbf{q}, 0)},$$

where $\varepsilon(\mathbf{q}, 0)$ is the dielectric function of the semiconductor surface states band. The density of empty surface states is changed by this screened potential. $\varepsilon(\mathbf{q}, 0)$ has a logarithmic singularity at $q = 2k_F$. When the Fermi level falls inside the empty surface states band π_{CB}^*, the screening effects become more pronounced within the range of positive sample bias when compared to the cases of low doped n-type and p-type surfaces for which the π_{CB}^* band is completely empty. Consequently, the empty-state STM images of highly doped n-type samples reveal details caused by local screening, in contrast to STM images of p-type samples, where empty-state STM images are less informative than filled-state images.

Because of the spatial localization of surface states in the π-bonded chains, screening occurs in the direction of π-bonded atomic rows, and consequently it is a quasi-1D process. The additional contribution to the local surface density of states due to screening of the impurity potential can be expressed as

$$\delta\nu = \frac{W\nu_0^2}{1 - W\nu_0}\sin(2\mathbf{k}(\varepsilon)\cdot\mathbf{r} + \delta),$$

where ν_0 is the unperturbed density of surface states, δ is the phase shift determined by the exact shape of the potential, and $\mathbf{k}(\varepsilon)$ is the quasi-1D wave vector corresponding to the energy value ε. The additional term for the tunneling current at small positive bias voltage can then be written as

$$I(V, r) = \frac{e^2}{\hbar}V\frac{W\nu_0^2}{1 - W\nu_0}\frac{\gamma_t(\varepsilon_F)\gamma_b(\varepsilon_F)}{\gamma_t(\varepsilon_F) + \gamma_b(\varepsilon_F)}\frac{\cos(2k_F r + \delta)}{k_F r},$$

where e is the electron charge and $\hbar$ is Plank's constant. In the effective mass approximation, the Fermi level position is determined by the expression

$$\varepsilon_F = \frac{\hbar^2 k_F^2}{2m_{\text{eff}}}.$$

As can be inferred from the experimental observations presented in Fig. 2, the typical spatial extent of the area with enhanced tunneling current near a defect is about 50 Å. We suppose that it is reasonable to use the bulk value of electron effective mass: $m_{\text{eff}} = 0.063m$ with m the free electron mass. In this case the degree of occupation for the empty surface states band can be estimated from the value of the Fermi wavelength $k_F^{-1} \sim$ 100 Å, and we then find that the Fermi level ε_F is approximately 4 meV *above* the bottom of the π_{CB}^* band, which is close to the value of 0.5% band filling obtained in [13].

We argue that specific features of the surface electronic structure do not dramatically affect the general shape of the tunneling spectrum. For instance, our experimental tunneling conductivity spectrum for the Ge(111)–(2 × 1) surface is very similar to the tunneling spectrum for the Ge(111)–c(2 × 8) surface [14]; i.e., the exact type of surface reconstruction *does not* dominate the tunneling spectrum. When the applied bias voltage approaches the conduction band from below, the tunneling rate from surface states to semiconductor bulk states increases (Fig. 1) due to a decrease of the depletion layer width. At a certain voltage this tunneling rate becomes comparable to the tunneling rate from surface states to the metallic tip. The weakest link of the STM junction, which is caused by tunneling from surface states to the bulk semiconductor, will then disappear. One may expect in this specific range of bias voltages the appearance of a peak in the tunneling conductivity versus bias voltage dependence [15]. Because the onset of the peak is located *inside* the surface band gap, the value of the surface band gap measured by tunneling spectroscopy is smaller than its real value.

The difference between tunneling spectroscopy on Ge(111)–(2 × 1) and Ge(111)–c(2 × 8) surfaces is due to the difference in the physics of depletion-layer formation. In the case of *n*-type Ge(111)–(2 × 1), strong band bending is present at the surface due to charging of the surface states. On the other hand, tip-induced band bending is responsible for the creation of the depletion layer at the Ge(111)–c(2 × 8) surface [14].

The bulk band gap value for the Ge(111)–(2 × 1) surface is 0.74 eV [8]. Due to the gap narrowing described above, the surface band gap value derived from our experimental tunneling conductivity spectra is about 0.6 eV (see Fig. 1). This value corresponds to the reduced bulk band gap value and not to the separation between the surface-state related bands. We would like to point out once more that, in spite of the dominating role of surface states in low-temperature STM imaging of the (111) surface of elemental semiconductors, the STS spectra always reflect the electronic structure of bulk states.

The intense peak appearing in the tunneling conductivity spectra near the conduction band edge is a characteristic feature of spectroscopy on the (111) surface of Ge and Si that is not strongly affected by the exact type of reconstruction (2 × 1, 2 × 8) [14, 16].

In conclusion, the Ge(111)–(2 × 1) surface obtained by *in situ* sample cleavage was investigated by means of low-temperature STM and STS. The dominating influence of surface states on the STM image formation was revealed. It was shown that perturbations of the local density of states around surface defects are confined along the π-bonded chain rows, directly reflecting the quasi-1D spatial distribution of the surface states. The surface band structure for the heavily doped *n*-type Ge(111)–(2 × 1) surface was clarified, and the degree of occupation of the empty surface state band π_{CB}^* was estimated from the typical spatial extent of the area with enhanced tunneling current. It was demonstrated that the tunneling spectrum is determined not only by the local density of states but also by the nonequilibrium kinetics of the tunneling processes.

The authors are grateful to A. Ezhov for technical assistance. This research was supported in part by the Russian Foundation for Basic Research, project nos. 03-02-16807 and 04-02-19957, and by a Leading Scientific Schools, grant no. 1604-2003-2. Support from the Samsung Corporation is also gratefully acknowledged. C.V.H. would like to thank the Fund for Scientific Research—Flanders (Belgium), as well as the Belgian Interuniversity Attraction Poles (IAP) and the Flemish Concerted Action (GOA) research programs, for additional financial support.

REFERENCES

1. R. M. Tromp, L. Smith, and J. F. van der Veen, Phys. Rev. B **30**, 6235 (1984).
2. K. C. Pandey, Phys. Rev. Lett. **47**, 1913 (1981).
3. N. Takeuchi, A. Selloni, A. I. Shkrebtii, and E. Tosatti, Phys. Rev. B **44**, 13 611 (1991).
4. S. I. Vasilev, S. I. Oreshkin, V. I. Panov, *et al.*, Instrum. Exp. Tech. **40**, 566 (1997).
5. M. Rohlfing, M. Palummo, G. Onida, and R. Del Sole, Phys. Rev. Lett. **85**, 5440 (2000).
6. J. N. Nicholls and B. Reihl, Surf. Sci. **218**, 237 (1989).
7. R. M. Feenstra, G. Meyer, F. Moresco, and K. H. Rieder, Phys. Rev. B **64**, 081306 (2001).
8. C. S. Wang and B. M. Klein, Phys. Rev. B **24**, 3393 (1981).
9. C. Van Haesendonck, N. S. Maslova, V. I. Panov, *et al.*, Int. J. Nanosci. **2**, 575 (2003).
10. D. E. Eastman and J. L. Freeouf, Phys. Rev. Lett. **33**, 1601 (1974).
11. O. Agam, N. S. Wingreen, B. L. Altshuler, *et al.*, Phys. Rev. Lett. **78**, 1956 (1997).
12. P. I. Arseyev, N. S. Maslova, and S. V. Savinov, JETP Lett. **68**, 320 (1998).
13. J. N. Nicholls, P. Mårtensson, and G. V. Hansson, Phys. Rev. Lett. **54**, 2363 (1985).
14. R. M. Feenstra, S. Gaan, G. Meyer, and K. H. Rieder, Phys. Rev. B **71**, 125316 (2005).
15. A. Depuydt, C. Van Haesendonck, N. S. Maslova, *et al.*, Phys. Rev. B **60**, 2619 (1999).
16. J. K. Garleff, M. Wenderoth, K. Sauthoff, *et al.*, Phys. Rev. B **70**, 245424 (2004).

JETP Letters, Vol. 82, No. 5, 2005, pp. 284–286. Translated from Pis'ma v Zhurnal Éksperimental'noĭ i Teoreticheskoĭ Fiziki, Vol. 82, No. 5, 2005, pp. 317–319.
Original Russian Text Copyright © 2005 by Trunin, Boriskov, Belov, Bykov, Il'kaev, Simakov, Urlin, Shuĭkin.

Shock-Wave Compression of Hydrogen to Pressures of 65 GPa

R. F. Trunin*, G. V. Boriskov, S. I. Belov, A. I. Bykov, R. I. Il'kaev, G. V. Simakov,
V. D. Urlin, and A. N. Shuĭkin
Russian Federal Nuclear Center VNIIÉF, pr. Mira 37, Sarov, Nizhni Novgorod region, 607190 Russia
** e-mail: root@gdd.vniief.ru*
Received July 8, 2005

The results of experiments on determining the shock-wave compression of initially solid hydrogen (protium) in the pressure range from 17 to 66 GPa are reported. The data have been obtained by using spherical explosive charges. Pressure in samples is created by the impact of a steel striker accelerated to maximum velocities of 23 km/s. Gaseous protium is converted to the solid state using a special cryogenic cooling system. *© 2005 Pleiades Publishing, Inc.*

PACS numbers: 51.35.+a, 52.35.Tc

The behavior of initially solid hydrogen (protium) under high pressures and temperatures is of interest due to a number of circumstances. First of all, it is associated with the study of the structure of stars and the giant planets of the Solar System, as well as with problems involving controlled nuclear fusion and obtaining metallic hydrogen and many applied problems. However, investigations of shock-wave compression of protium in Russia have not yet been carried out for some reason. Experiments on shock-wave compression of liquid (in the initial state) protium to pressures of 15 GPa were performed in the United States [1–3]. In these experiments, explosive-based measuring systems and two-stage light-gas guns were used.

Being a substance with the simplest single-electron structure, hydrogen allows ab initio analysis of high-density and high-temperature plasma states without employing semiempirical approaches. Unfortunately, theoretical results obtained by different researchers differ considerably, primarily due to the difficulty of the correct inclusion of the strong interaction between particles under such conditions. For this reason, obtaining reliable experimental data on hydrogen compression in the unexplored range of states must not only serve an impetus for performing a deeper theoretical analysis of this problem, but also provide a test material for verifying theoretical premises.

Let us also recall the results of recent experiments on the compressibility of liquid deuterium [4, 5], in which anomalously high densities of this material were obtained. Numerous doubts as to the authenticity of these data called for a series of new experiments [6–9], which ultimately refuted the results obtained in [4, 5]. This work is a continuation of these experiments. Finally, we mention the opportunity of studying dissociation of molecules and ionization of atoms in the high-temperature states realized under the action of megabar-amplitude shock waves on the samples using hydrogen isotopes as examples.

The main aim of this work is to reach pressures substantially exceeding those achieved so far [1–3]. The fact that our measurements were made with solid protium (in the initial state), in contrast to the American experiments, which were carried out with a liquid substance, is immaterial, because these phases are close in properties. Moreover, the results allow mutual recalculations. It is worth noting that we do not know of publications on shock-wave compression of solid protium.

These experiments began in 2002 at the Russian Federal Nuclear Center VNIIÉF (Sarov) and were carried out simultaneously with analogous experiments on liquid and solid deuterium [7, 9]. Intense shock waves were produced by a hemispherical explosive charge detonated simultaneously on the entire outer spherical surface [10]. The explosion products of a converging detonation wave accelerate a steel striker separated by a small air gap from the inner cavity of the explosive towards the center of the system. The velocity of the striker at the impact radius varies from 9 to 23 km/s depending on the chosen measuring instrument and the range of measurements (the range in which the samples are arranged). Three runs of measurements were conducted, differing in the geometry of measuring instruments (radii of explosives and strikers, their thickness, and the radii of location of the samples and the hemispherical aluminum screens shielding them). The thickness ΔR of protium samples was the same (4 mm) and the thickness of the screens was 4–5 mm. Each run consisted of four independent experiments with three independent measurements of the wave velocity in each experiment.

In these experiments, we determined the time $\Delta\tau$ of the propagation of shock waves through the sample thickness ΔR. The time was monitored using electric-contact sensors; time intervals were recorded on TDS and HP54645 oscilloscopes with an accuracy of 2 ns. As a result of measurements, we determined the averaged velocity $D = \Delta R/\Delta\tau$ of a shock wave in a given run of measurements.

To determine the mass velocities, we used the reflection method [11]. In this method, known states in the Al screen (which were determined in a preliminary run of measurements) and the experimentally obtained average wave velocity D_{av} are used to find the shock-wave compression pressure P and the mass velocity U of the substance behind the shock wave front from the point of intersection of the wave ray $\rho_0 D_{av}$ and the expansion isentrope of Al from the states on its shock adiabat (in this case, the adiabat of "cold" Al at $T \sim 10$ K). This isentrope was calculated from the equation of state for aluminum that was considered in [12, 13] and fitted to the results obtained in [14]. The advantage of this equation in describing the available experimental data on aluminum (and pertaining to the pressure interval of interest) over other available equations of states was demonstrated preliminarily. The energy and density of shock compression were determined from the relations following from conservation laws.

The initial state of the sample was monitored from the data of semiconductor thermometers mounted in the region of location of the samples, where the condensation of hydrogen occurred. This region was cooled by helium vapor or directly by liquid helium supplied via a special system of pipes. The system ensured the supply of a measured (and controlled) amount of helium to the cell being cooled, which contained initially gaseous protium [7, 9]. When the liquefaction temperature of protium (24 K) was reached, it condensed, which was indicated by the abrupt decrease in the volume of the gasholder containing the initial gas. After holding protium in the liquid state for 5–10 min, the temperature of the sample being cooled was further reduced to convert it to the solid state (at a temperature below 19 K). After 5–10 min, the experimental cell was detonated.

The converging shock wave on the screen and in the sample under investigation is not steady. For this reason, small (≤1%) corrections to the wave velocity must be introduced to determine the parameters of compression. The final results are given in the table.

The initial density of solid protium is $\rho_0 = 0.088$ g/cm^3. The error in the wave velocity corresponds to the standard deviation of the arithmetic mean, while the error in the mass velocity corresponds to the maximum error in the U value obtained from the intersection of expansion isentrope for aluminum with two rim rays of the wave in protium, which correspond to the errors in the D value. The corresponding errors in pressure, density, and compression are determined in terms of the errors in the kinematic parameters.

Table

Shock wave velocity D, km/s	Mass velocity U, km/s	Pressure P, GPa	Density ρ, g/cm^3
31.30 ± 0.30	23.82 ± 0.30	65.6 ± 1.0	0.368 ± 0.030
22.20 ± 0.50	16.43 ± 0.30	32.1 ± 0.9	0.339 ± 0.030
16.67 ± 0.30	11.59 ± 0.20	17.0 ± 0.3	0.289 ± 0.020

Figure 1 shows our results in the D vs. U coordinates. Naturally, these results differ from those obtained in [1–3] for initially liquid protium. For their appropriate comparison, we recalculate the results obtained here to the initial density of liquid (0.071 g/cm^3). To this end, we assume that the $D(\rho_0)$ dependence in protium and deuterium in each of the three devices used here is linear. According to analysis of the data on the compression of metallic elements, such an assumption is reasonable under strictly controlled experimental conditions (which are in fact satisfied). The corresponding position of the recalculated points is shown in Fig. 1. It is seen that the results of our measurements and American experiments are in satisfactory agreement. Thus, the upper limit of investigated pressures for protium has been increased sixfold.

The following circumstance is worth noting. The slopes of the adiabats of both solid and liquid hydrogen phases in the velocity range $D > 20$ km/s ($P \approx 30$ GPa) are close and amount to $s = dD/dU \approx 1.26$. Therefore, the limiting compression is $\rho_{lim}/\rho_0 = s/(s-1) \approx 4.85$, which corresponds to a reasonable value of the adiabatic exponent for an ideal monatomic gas. This is probably an indication that dissociation processes occurring under the shock-wave compression of diatomic protium are completed under these pressures.

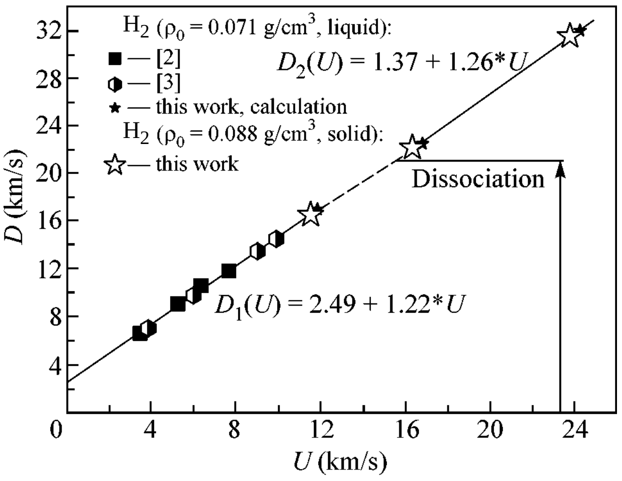

Fig. 1. Results for protium in the D vs. U coordinates.

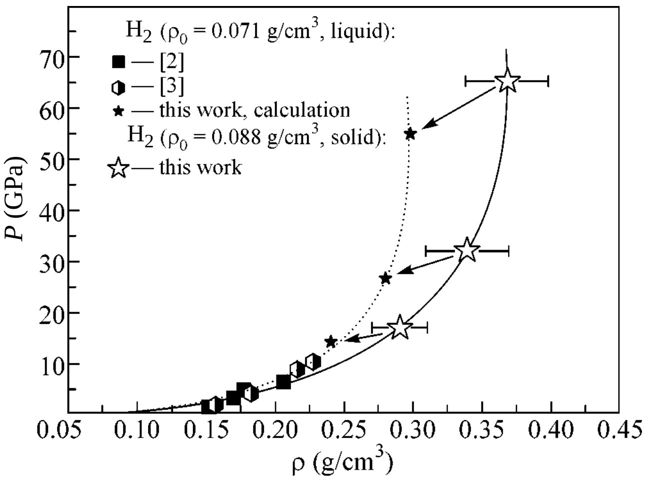

Fig. 2. Results for protium in the P vs. ρ coordinates.

Figure 2 shows the results in P vs. ρ coordinates. The steep region of the adiabat for protium is close in compression to the limiting states and, as the data obtained in [6–9], do not lead to an anomalously large density of shock-wave compression detected in experiments with liquid deuterium [4, 5].

REFERENCES

1. L. M. van Thiel and J. Alder, Mol. Phys. **10**, 427 (1966).
2. R. D. Dick and G. I. Kerley, J. Chem. Phys. **73**, 5264 (1980).
3. W. J. Nellis, A. C. Mitchell, M. van Thiel, *et al.*, J. Chem. Phys. **79**, 1480 (1983).
4. L. B. Da Silva, P. Celliers, G. W. Collins, *et al.*, Phys. Rev. Lett. **78**, 483 (1997).
5. G. W. Collins, P. Celliers, L. B. Da Silva, *et al.*, Phys. Plasmas **5**, 1864 (1998).
6. M. D. Knudson, D. L. Hanson, J. E. Bailey, *et al.*, Phys. Rev. Lett. **87**, 225 501 (2001).
7. S. I. Belov, G. V. Boriskov, A. I. Bykov, *et al.*, Dokl. Akad. Nauk **392**, 755 (2003) [Dokl. Phys. **48**, 553 (2003)].
8. M. D. Knudson, D. L. Hanson, J. E. Bailey, *et al.*, Phys. Rev. B **69**, 144 209 (2004).
9. S. I. Belov, G. V. Boriskov, A. I. Bykov, *et al.*, Pis'ma Zh. Éksp. Teor. Fiz. **76**, 508 (2002) [JETP Lett. **76**, 433 (2002)].
10. L. V. Al'tshuler, R. F. Trunin, K. K. Krupnikov, and N. V. Panov, Usp. Fiz. Nauk **166**, 575 (1996) [Phys. Usp. **39**, 539 (1996)].
11. L. V. Al'tshuler, R. F. Trunin, K. K. Krupnikov, and N. V. Panov, Zh. Éksp. Teor. Fiz. **34**, 886 (1958) [Sov. Phys. JETP **7**, 614 (1958)].
12. S. B. Kormer, A. I. Funtikov, V. D. Urlin, and A. N. Kolesnikova, Zh. Éksp. Teor. Fiz. **42**, 686 (1962) [Sov. Phys. JETP **15**, 477 (1962)].
13. V. D. Urlin, Zh. Éksp. Teor. Fiz. **49**, 485 (1965) [Sov. Phys. JETP **22**, 341 (1966)].
14. R. F. Trunin, L. F. Gudarenko, M. V. Zhernokletov, and G. V. Simakov, *Experimental Data on Shock-Wave Compression and Adiabatic Expansion of Condensed Substances*, Ed. by R. F. Trunin (RFYaTs–VNIIÉF, Sarov, 2001) [in Russian].

Translated by N. Wadhwa

JETP Letters, Vol. 82, No. 5, 2005, pp. 287–291. Translated from Pis'ma v Zhurnal Éksperimental'noĭ i Teoreticheskoĭ Fiziki, Vol. 82, No. 5, 2005, pp. 320–325.
Original Russian Text Copyright © 2005 by Gusev, Lipatnikov.

Ordering in the ζ-Ta_4C_{3-x} Carbide Phase

A. I. Gusev and V. N. Lipatnikov
Institute of Solid State Chemistry, Ural Division, Russian Academy of Sciences,
ul. Pervomaĭskaya 91, Yekaterinburg, 620219 Russia
e-mail: gusev@ihim.uran.ru

Received July 11, 2005

The structure of the ζ-Ta_4C_{3-x} nonstoichiometric trigonal (rhombohedral) carbide, which is formed in the tantalum–carbon system, has been analyzed by neutron diffraction, x-ray diffraction, and metallography. The ordered distributions of carbon atoms and structure vacancies have been experimentally determined and the distribution function of carbon atoms over the nonmetallic-sublattice sites, where ordering occurs, has been calculated. The parameters of the unit cell of the ζ-Ta_4C_{3-x} ($TaC_{0.67}$) trigonal (space group $R\bar{3}m$) carbide are found to be $a_H = 0.3123$ nm and $c_H = 3.0053$ nm. It has been shown that the metallic close packed sublattice of the ζ-Ta_4C_{3-x} carbide is formed by alternating blocks, where metal atoms are located both in the fcc and hcp sublattices of the TaC_y cubic and Ta_2C hexagonal carbides, respectively. *© 2005 Pleiades Publishing, Inc.*

PACS numbers: 61.12.Gz, 61.50.Ks, 61.66.Fn, 61.72.Dd, 64.70.Kb, 81.30.–t

A feature of MC_y ($MC_y\square_{1-y}$, $0.65–0.70 \le y \le 0.88–1.00$) cubic, $M_2C_{y'}$ ($MC_{y'/2}\square_{0.5-y'/2}$, $0.70 \le y' \le 1.00$) hexagonal, and ζ-M_4C_{3-x} ($M_4C_{3-x}\square_{1+x}$, or $MC_{(3-x)/4}\square_{(1+x)/4}$, $0.20 < x < 0.56$) trigonal (rhombohedral) carbides formed in M–C binary systems (M = V, Nb, or Ta) consisting of a Group V transition metal and carbon is a strong nonstoichiometry of the nonmetallic sublattice. The content of structure vacancies □ in the carbon sublattice of the indicated carbides may reach several tens of at %. For this reason, they are classified among the group of strongly nonstoichiometric compounds [1, 2]. A high concentration of vacancies in strongly nonstoichiometric carbides with base cubic, hexagonal, and trigonal lattices is a background for atomic–vacancy ordering in these compounds. Ordering in the MC_y cubic and $M_2C_{y'}$ hexagonal carbides was studied in detail both experimentally and theoretically [1–3], whereas only assumptions are available for ordering in trigonal carbides, known as ζ-M_4C_{3-x} phases. In order to fill this gap, the structure of the ζ-Ta_4C_{3-x} trigonal (rhombohedral) carbide is analyzed by the neutron diffraction method.

The ζ-Ta_4C_{3-x} phase is infamous in publications. Its synthesis is difficult, and information on it is scarce. The ζ phase in the Ta–C system has been found in two- and three-phase samples with compositions between $TaC_{0.52}$ hexagonal and $TaC_{0.73}$ cubic carbides [4]. The samples were obtained by solid-state sintering of Ta and C powders at 2070–2370 K. The maximum amount of the ζ phase was contained in $TaC_{0.59–0.64}$ carbides. The heating of the $TaC_{0.64}$ carbide at 2070 K for 26 h resulted in an increase in the relative content of the ζ phase, although the sample remained three-phase. Heating at a higher temperature resulted in a decrease in the amount of this phase and was accompanied by the spreading of the reflections of the ζ phase in an x-ray diffraction pattern. X-ray analysis of the ζ phases of vanadium, niobium, and tantalum [5] shows that they have trigonal symmetry (space group $R\bar{3}m$) and their composition including the structure can be represented as M_4C_{3-x}. According to electron-diffraction data [6], the ζ-Ta_4C_{3-x} phase belongs to the Sn_2P_3 structure type (space group $R\bar{3}m$) and is close in composition to $TaC_{0.67}$. This composition is realized due to the high concentration of carbon vacancies with respect to the stoichiometric composition Ta_4C_3: x in ζ-Ta_4C_{3-x} may reach 0.5. Using electron microscopy analysis of $TaC_{0.70–0.80}$ carbides, Rowcliffe and Thomas [7] hypothesized that the formation of the ζ phase from the TaC_y nonstoichiometric cubic carbide is a result of the elimination of every fourth $(111)_{B1}$ carbon plane and the corresponding shift of $(111)_{B1}$ metallic atomic planes. The elimination of the $(111)_{B1}$ carbon plane occurs due to the sink of structure vacancies and the shift of a neighboring $(111)_{B1}$ metallic plane is ensured due to the sink of dislocations. According to [8–10], the ζ phase of tantalum carbide is thermodynamically stable only for $T > 1400$ K and disappears when heated at 1200–1300 K. The authors of [8, 11] state that the milling of a bulk sample containing the ζ phase also leads to its disappearance. However, the conclusion made in [8–10] that the range of thermodynamic stability of ζ-Ta_4C_{3-x} is limited contradicts the data reported in [12, 13], according to which this phase is stable when annealing in vacuum or in argon atmosphere in the

0021-3640/05/8205-0287$26.00 © 2005 Pleiades Publishing, Inc.

wide temperature range 300–3170 K. The available data on the intensities of the diffraction reflections of the ζ phase are strongly different. For this reason, its structure has not yet been determined exactly. Markhasev *et al.* [8] believe that the ζ-Ta_4C_{3-x} carbide is an ordered phase of the TaC_y nonstoichiometric cubic (with the *B*1 structure) tantalum carbide. However, the ζ-Ta_4C_{3-x} trigonal carbide and the TaC_y disordered cubic carbide have metallic sublattices with different symmetries, whereas the symmetry of the metallic sublattice of the ordered phase in disorder–order transitions in nonstoichiometric compounds is necessarily the same as in the disordered base phase.

A high concentration (from 25 to 33–35 at %) of structure vacancies in the carbon sublattice of the ζ-$Ta_4C_{3-x}\square_{1+x}$ phase is a background for atomic–vacancy ordering. However, there is no experimental evidence of the disordered (statistical) or ordered distribution of carbon atoms and vacancies. The ζ-M_4C_{3-x} carbide phases (M = V, Nb, or Ta) have the trigonal structure (space group $R\bar{3}m$), where 12 metal atoms doubly occupy the 6(*c*) sites, whereas the sites of the nonmetallic sublattice are the 3(*a*), 3(*b*), and 6(*c*) sites with the coordinates (0 0 0), (0 0 1/2), and (0 0 ~5/12), respectively (hereinafter, the coordinates of atoms and the unit-cell parameters are given in the hexagonal axes). One quarter of all sites of the nonmetallic sublattice in the ζ-$Ta_4C_{3-x}\square_{1+x}$ phase are vacant even at $x = 0$. It is known that carbon atoms occupy all the 6(*c*) sites. For this reason, the remaining carbon atoms and structure vacancies occupy the 3(*a*) and 3(*b*) sites statistically or regularly. In the statistical distribution, carbon atoms occupy the 3(*a*) and 3(*b*) sites of the nonmetallic sublattice with the same probability $(1 - x)/2$. Ordered distribution is possible in two variants. In the first variant, carbon atoms occupy the 3(*a*) sites with the probability $(1 - x)$ and the 3(*b*) sites are vacant. In the second variant, carbon atoms are located at the 3(*b*) sites with the probability $(1 - x)$ and vacancies are at the sites 3(*a*). Since new crystallographic positions do not appear in such ordering, the lattice conserves its symmetry. Therefore, it is expected that reflection intensities are only redistributed in the diffraction spectrum and additional reflections do not arise. The amplitude of the x-ray scattering by carbon atoms is much lower than that by tantalum atoms. For this reason, in x-ray diffraction experiment with the ζ-Ta_4C_{3-x} phase, the relative change in the reflection intensities due to the redistribution of carbon atoms is very small. If a sample contains impurity carbide phases and is textured (both properties are characteristic of samples with the ζ phase), it is really impossible to reveal the disordered or ordered distribution of carbon atoms and structure vacancies by the x-ray diffraction method. The distribution of carbon atoms and vacancies $\square$ in ζ-Ta_4C_{3-x} can be experimentally determined using neutron diffraction, but this method has not yet been applied to analyze ζ-Ta_4C_{3-x}. In this work, the distribution of carbon atoms and vacancies $\square$ in the ζ-Ta_4C_{3-x} lattice is experimentally determined using the structure neutron diffraction method together with accurate x-ray diffraction and metallography.

We synthesized samples of the $TaC_{0.68–0.78}$ tantalum carbide by sintering powder mixtures in 0.0013-Pa vacuum in three temperature regimes: (i) sintering $TaC_{0.975}$ and Ta for 6 h at 2270 K with intermediate milling of the products after 3 h, (ii) sintering $TaC_{0.75}$ and C for 6 h at 2200–2400 K with intermediate milling after 3 h, (iii) sintering $TaC_{0.75}$ and C for 20 h at 2200–2400 K with intermediate milling after 10 h. The composition of the samples was determined by the chemical method and the composition of the surface of sintered samples was additionally controlled by x-ray fluorescence spectroscopy (energy dispersive x-ray spectroscopy). The $TaC_{0.685}$ sample synthesized in the first regime contained a large amount of ζ-Ta_4C_{3-x}. The ζ phase was absent in the samples freshly synthesized in the second and third regimes and they were additionally annealed. The samples synthesized in the second regime were annealed at 1470 K for 100 h and then annealing was performed with a decrease in temperature to 570 K with a rate of 0.25 K/min. The samples synthesized in the third regime were annealed at 1570 K for 35 h, then the annealing temperature was decreased to 1170 K for 120 h, and a further decrease in temperature to 570 K was performed at a rate of 0.25 K/min. The x-ray patterns of annealed $TaC_{0.70}$ and $TaC_{0.72}$ bulk samples include intense reflections of the ζ-Ta_4C_{3-x} phase. The authors of [8, 11] reported that the ζ phase disappeared after the milling of bulk samples, but we did not find this effect in this work: the reflections of the ζ phase did not disappear in the x-ray patterns of powders obtained by milling the $TaC_{0.685}$, $TaC_{0.70}$, and $TaC_{0.72}$ bulk samples.

X-ray diffraction was measured by the Bragg–Brentano method in Cu$K\alpha_{1,2}$ radiation in the angular range $2\theta = 5°–120°$ with the step $\Delta(2\theta) = 0.02°$ and by the modified Guinier method in Cu$K\alpha_1$ radiation using an STADI-P autodiffractometer with transmission geometry. Neutron diffraction ($\lambda = 0.1532$ nm) was measured in the angular range $2\theta = 10°–125°$ in the step scanning regime with the step $\Delta(2\theta) = 0.1°$ and a signal accumulation time of 1.0 min in each point.

A feature of experimental x-ray and neutron diffraction patterns obtained by the Bragg–Brentano method from both bulk and powder samples is a high intensity of the (0 0 12) and (0 0 24) reflections, which is much higher than their theoretical intensity. The strong enhancement of these reflections is caused by the uniaxial texture of the samples in the (0 0 1) direction, i.e., along the *c* axis of the ζ-Ta_4C_{3-x} phase. Indeed, analysis of the microstructure of bulk tantalum carbide samples reveals the pronounced characteristic plate fragments of the ζ phase (Fig. 1). The noticeable effect of the texture of ζ-Ta_4C_{3-x} samples on the intensity of x-ray reflections was mentioned in [11, 13]. The existence of a certain texture is the cause of significant differences in the relative intensities of the diffraction lines of the ζ phase that were measured in [4, 8, 11, 13]. In order to eliminate the effect of texture on the intensity of reflections, special diffraction experiments were carried out such that x-ray patterns were obtained in transmission geometry by the modified Guinier method. The measurements were conducted with strong accumulation of a signal at each point. Owing to the high-precision measurements with low background, the signal-to-noise ratio was very high and reached 30–40 even for moderate-intensity reflections and 70–80 for intense reflections (when the same TaC_y samples were investigated by the Bragg–Brentano method, the signal-to-noise ratio for moderate-intensity lines did not exceed 20). The use of $CuK\alpha_1$ radiation made it possible to eliminate double reflections and to additionally increase the measurement accuracy. Analysis shows that all tantalum carbide samples with the ζ phase also contain the TaC_y carbide and a small amount of the Ta_2C hexagonal carbide. Figure 2 shows the x-ray patterns of $TaC_{0.685}$ tantalum carbide with a high content of the ζ phase. Their analysis shows that the set of the diffraction reflections of the ζ-Ta_4C_{3-x} phase that are observed in x-ray and neutron diffraction patterns of the samples under investigation correspond to a trigonal unit cell (space group $R\bar{3}m$). A hexagonal unit cell of the ζ phase (Fig. 3) contains three Ta_4C_{3-x} formula units.

The accurate determination of the unit-cell parameters of the observed phases and the phase composition of the $TaC_{0.685}$ sample was performed from the x-ray pattern that was obtained by the Guinier method and excluded the effect of texture on the intensity of diffraction reflections. The parameters of the unit cell of the ζ-Ta_4C_{3-x} trigonal phase (space group $R\bar{3}m$) are a_H = 0.3123 nm and c_H = 3.0053 nm in hexagonal axes (a_{tr} = 1.0179 nm and α_{tr} = 17.65° in trigonal axes). The relative contents of the TaC_y cubic carbide, Ta_2C lowest hexagonal carbide, and ζ phase in the $TaC_{0.695}$ sample are equal to ~18, 1, and 80–81 vol %, respectively. The period of the cubic phase (space group $Fm\bar{3}m$) is a_{B1} ~ 0.4418 nm and corresponds to ~$TaC_{0.76}$ carbide. The periods of the Ta_2C hexagonal carbide (space group $P6_3/mmc$) are a = 0.3119 nm and c = 0.4934 nm. Taking into account the composition of the sample and the content of the $TaC_{0.76}$ cubic and $TaC_{0.50}$ (Ta_2C) hexagonal carbides, we conclude that the ζ phase has a composition of ~$TaC_{0.67}$ ($TaC_{2/3}$) or Ta_4C_{3-x} with $x = 1/3$.

The ratio of the intensities of the observed x-ray diffraction reflections of the ζ phase corresponds to ether the statistical (disordered) distribution of carbon atoms over the 3(a) and 3(b) sites of the nonmetallic sublattice or the ordered distribution of carbon atoms and vacancies over the 3(a) and 3(b) sites, respectively. Another ordering variant, when carbon atoms are located at the 3(b) sites and vacancies, at the 3(a) sites, is inconsistent with experiment. Indirect information on the distribution of carbon atoms and vacancies was obtained by determining the coordinates including the displacements of atoms.

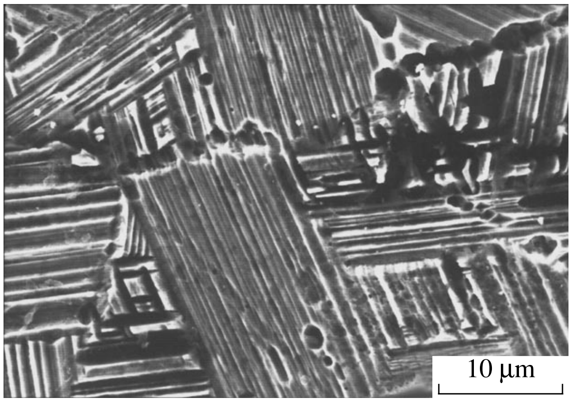

Fig. 1. Microstructure of the sintered $TaC_{0.685}$ sample with plate fragments of the ζ-Ta_4C_{3-x} phase. The sample is strongly textured. Such a microstructure is characteristic of all tantalum carbide samples containing the ζ phase.

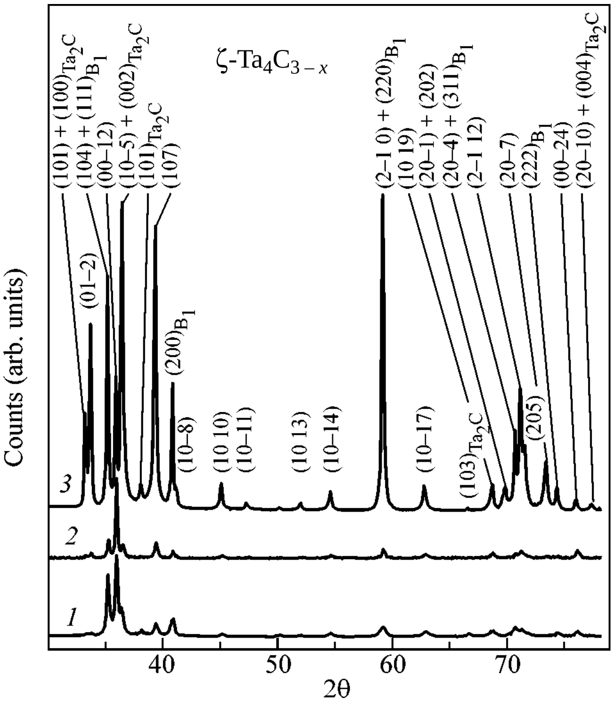

Fig. 2. X-ray patterns of the $TaC_{0.685}$ tantalum carbide containing ~80 vol % of the ζ-Ta_4C_{3-x} phase. The intensities of the (0 0 12) and (0 0 24) reflections obtained by the Bragg–Brentano method from (*1*) the surface of a bulk sample and (*2*) the powder sample are noticeably higher than the theoretical values due to the axial texturing. Pattern *3* is obtained from the powder sample by the modified Guinier method with transmission geometry, which makes it possible to eliminate the effect of texture on the intensity of diffraction reflections.

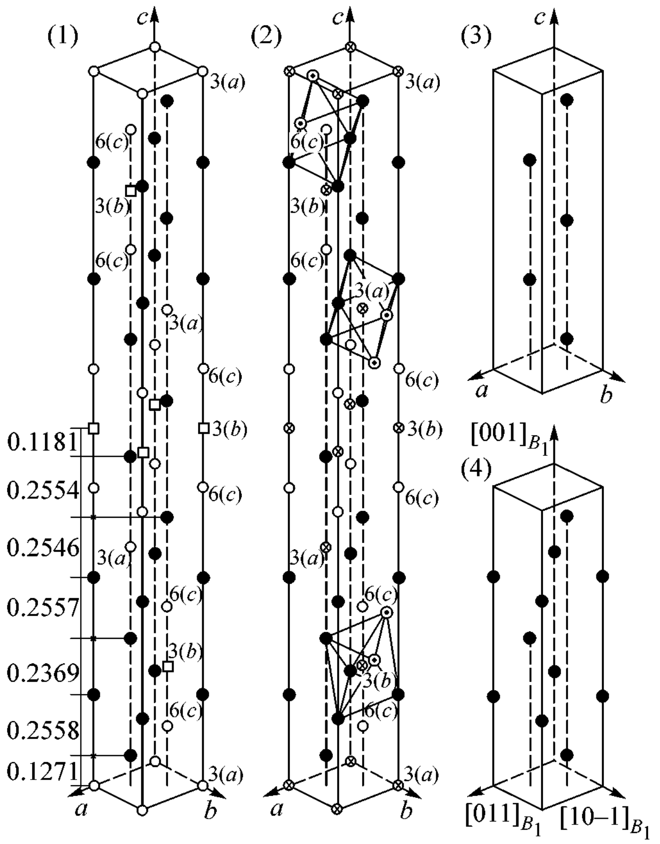

Fig. 3. Distribution of atoms in the unit cell of the ζ-Ta_4C_{3-x} trigonal (space group $R\bar{3}m$) phase (cell is shown in the hexagonal axes and the interplanar spacings along the *c* axis are given in nanometers): (1) the ordered distribution of carbon atoms over the 3(*a*) sites and structure vacancies □ over the 3(*b*) sites, (2) the disordered distribution of carbon atoms and vacancies with a probability of $(1 - x)/2$ over the 3(*a*) and 3(*b*) sites of the nonmetallic sublattice, and (3) and (4) the distribution of Ta atoms in the lattices of the Ta_2C lowest hexagonal carbide and TaC_y cubic carbide (with the *B*1 structure), respectively. For the ζ-Ta_4C_{3-x} phase, the 3(*a*), 3(*b*), and 6(*c*) sites of the nonmetallic sublattice and their octahedral surrounding by tantalum atoms are shown for the disordered phase. Tantalum atoms are shown by ●, tantalum atoms located outside the unit cell are shown by ⊙, carbon atoms are shown by ○, structure vacancies are shown by □, and the 3(*a*) and 3(*b*) sites of the nonmetallic sublattice that are statistically occupied by carbon atoms with a probability of $(1 - x)/2$ are shown by C.

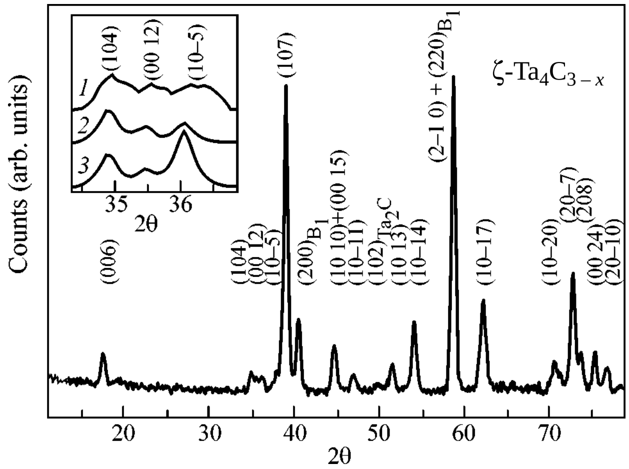

Fig. 4. Neutron diffraction pattern (λ = 0.1532 nm) of the $TaC_{0.685}$ tantalum carbide containing ~80 vol % of ζ-Ta_4C_{3-x} ($TaC_{0.67}$). The inset shows (*1*) the fragment of the measured neutron diffraction pattern in comparison with the theoretical neutron diffraction patterns of the ζ-Ta_4C_{3-x} ($TaC_{0.67}$) phase with the (*2*) ordered and (*3*) disordered distributions of carbon atoms and vacancies over the 3(*a*) and 3(*b*) sites of the nonmetallic sublattice.

In the unit cell of the ζ-Ta_4C_{3-x} phase, 12 Ta atoms doubly occupy the 6(*c*) sites with the coordinates (0 0 0.1274) and (0 0 0.291), the 6(*c*) sites with the coordinates (0 0 0.417) are occupied by carbon atoms, and the 3(*a*) and 3(*b*) sites with the coordinates (0 0 0) and (0 0 1/2), respectively, are lattice sites at which carbon atoms may be located disorderedly or regularly (Fig. 3). Thus, carbon atoms in the ζ-Ta_4C_{3-x} phase are located at the octahedral interstitial sites of the close-packed metallic sublattice. Tantalum atoms occupying the 6(*c*) sites with the coordinates (0 0 0.1274) on the planes perpendicular to the *c* axis of the unit cell are shifted to the carbon-sublattice planes formed by the 3(*b*) sites and from the carbon-sublattice planes formed by the 3(*a*) sites. The existence of such displacements indirectly indicates different populations of the 3(*a*) and 3(*b*) sites by carbon atoms, i.e., their possible ordering. Interplanar spacings along the *c* axis are necessarily identical in the ζ-Ta_4C_{3-x} disordered carbide.

As is seen in Fig. 3, the ζ-Ta_4C_{3-x} phase has a close-packed metallic sublattice. However, the distribution of metal atoms in it differs from the distributions of metal atoms in the fcc and hcp sublattices of the TaC_y cubic carbide and Ta_2C lowest hexagonal carbide, respectively. The metallic sublattice of the ζ-Ta_4C_{3-x} phase consists of alternating blocks, where metal atoms are located in the fcc and hcp sublattices of the TaC_y cubic and Ta_2C hexagonal carbides, respectively, and is transient between these two sublattices.

Figure 4 shows the neutron diffraction pattern of the $TaC_{0.685}$ carbide containing ~80 vol % of ζ-Ta_4C_{3-x}. The neutron diffraction pattern is analyzed using the model of the trigonal unit cell (space group $R\bar{3}m$) with the parameters determined from the x-ray diffraction spectrum. The ratio of the neighboring reflections (1 0 4), (0 0 12), (1 0 –5), and (1 0 7) is characteristic evidence of the ordering in ζ-Ta_4C_{3-x}. The intensity *I* of the (1 0 4) reflection is the same for the disordered and ordered phases. In units of the $I_{(1\,0\,4)}$ intensity, the intensities are $I_{(0\,0\,12)} \approx 0.4$, $I_{(1\,0\,-5)} \approx 0.6$, and $I_{(1\,0\,7)} \approx 19$ for the ordered ζ phase and $I_{(0\,0\,12)} \approx 0.4$, $I_{(1\,0\,-5)} \approx 1.6$, and

$I_{(1\,0\,7)} \approx 15$ for the disordered phase. In the experiment, the intensity $I_{(1\,0\,-5)}$ is higher than the intensity $I_{(0\,0\,12)}$ by a factor of 1.5 (Fig. 4), which is characteristic of the ordered phase. On the whole, calculations show that the experimental neutron diffraction pattern corresponds to the ordered ζ-Ta_4C_{3-x} ($TaC_{0.67}$) phase with the distribution of carbon atoms over the 3(*a*) sites and completely vacant 3(*b*) sites.

Taking into account the ordered distribution of carbon atoms and vacancies □ over the 3(*a*) and 3(*b*) sites, the structure formula of the ζ phase is represented as $Ta_4C_2C_{1-x}\square_{1+x}$. Let the distribution of carbon atoms and vacancies over the 3(*a*) and 3(*b*) sites be characterized by the long-range order parameter η. Ideal ordering with the long-range order parameter $\eta_{\max} = 1$ is achieved for $x = 0$, when all the 3(*a*) sites are occupied by carbon atoms and the 3(*b*) sites are vacant. As *x*, i.e., the vacancy concentration, increases, the maximum long-range order parameter $\eta_{\max}$ decreases, because vacancies appear at the 3(*a*) sites. The maximum long-range order parameter depends on the content of the ζ phase as $\eta_{\max}(x) = (1 - x)$. In the disordered ζ phase, $3(1 - x)$ carbon atoms are equiprobably located at the 3(*a*) and 3(*b*) sites. Therefore, the relative concentration of carbon atoms involved in ordering is equal to $(1 - x)/2$. Thus, the distribution of carbon atoms over the 3(*a*) and 3(*b*) sites of the nonmetallic sublattice of the ζ phase is described by the function

$$n(\mathbf{r}) = (1-x)/2 + (\eta/2)\cos 6\pi z_h, \qquad (1)$$

where $\mathbf{r} = (x_h\, y_h\, z_h)$ is a 3(*a*) or (3(*b*) site of the nonmetallic sublattice (coordinates are given in hexagonal axes). Distribution function (1) is the probability of the location of a carbon atom at sites **r** belonging to the 3(*a*) and 3(*b*) sites of the nonmetallic sublattice of the ζ-Ta_4C_{3-x} phase. For the maximum long-range order parameter $\eta_{\max}(x) = (1 - x)$, function (1) is equal to $1 - x$ and 0 at all the 3(*a*) and 3(*b*) sites, respectively. In other words, for the maximum long-range order parameter, the probability of the location of a carbon atom at the 3(*a*) and 3(*b*) sites is equal to $1 - x$ and 0, respectively. In the absence of order, when $\eta = 0$, the distribution function has the form $n(\mathbf{r}) = (1 - x)/2$ at all the 3(*a*) or (3(*b*) sites of the nonmetallic sublattice.

In principle, for $x > 0$, the distribution of carbon atoms and vacancies occupying the 3(*a*) sites can also be disordered or ordered. In the case of ordering, the neutron diffraction pattern necessarily exhibits additional superstructure reflections in the small-angle range $2\theta < 30°$. Such additional reflections were not observed in the experiment. Therefore, the statistical distribution of carbon atoms and vacancies □ over the 3(*a*) sites is suggested in the ζ-Ta_4C_{3-x} ($TaC_{0.67}$) phase under investigation.

On the whole, the above investigation shows that the ζ-Ta_4C_{3-x} carbide is an independent nonstoichiometric compound of the Ta–C system in addition to two other nonstoichiometric compounds—the $Ta_2C_{y'}$ hexagonal and TaC_y cubic carbides. The ζ-Ta_4C_{3-x} carbide is stable in the compact and disperse states in a wide temperature range from 300 to ~2400 K. Conclusions made in [8–11, 14] that the ζ-Ta_4C_{3-x} phase is metastable are likely associated with the fact that the ζ phase was obtained in those works in the nonequilibrium state and, therefore, the annealing or milling of the samples resulted in the transformation of this phase into the TaC_y cubic carbide. The ζ-Ta_4C_{3-x} carbide has trigonal symmetry (space group $R\bar{3}m$) with order in the nonmetallic sublattice: for $x = 0$ and the maximum long-range order parameter, carbon atoms occupy all the 3(*a*) sites, whereas all the 3(*b*) sites are vacant; for $x > 0$ and the maximum long-range order parameter, carbon atoms occupy some 3(*a*) sites and vacancies occupy all the 3(*b*) sites and some 3(*a*) sites. The close-packed metallic sublattice of the ζ-Ta_4C_{3-x} phase is transient between the metallic sublattices of the TaC_y cubic and Ta_2C hexagonal carbides.

We are grateful to V.G. Zubkov, I.F. Berger, and A.P. Tyutyunnik for assistance in experiment. This work was supported by the Russian Foundation for Basic Research (project no. 03-03-32031a).

REFERENCES

1. A. I. Gusev, A. A. Rempel, and A. J. Magerl, *Disorder and Order in Strongly Nonstoichiometric Compounds: Transition Metal Carbides, Nitrides, and Oxides* (Springer, Berlin, 2001).
2. A. I. Gusev and A. A. Rempel', *Nonstoichiometry, Disorder, and Order in Solids* (Ural. Otd. Ross. Akad. Nauk, Yekaterinburg, 2001) [in Russian].
3. A. I. Gusev and A. A. Rempel', *Structural Phase Transitions in Nonstoichiometric Compounds* (Nauka, Moscow, 1988) [in Russian].
4. R. Lesser and G. Brauer, Z. Metallkd. **49**, 622 (1958).
5. K. Yvon and E. Parthe, Acta Crystallogr. B **26**, 149 (1970).
6. J. L. Martin, A. Rocher, B. Jouffrey, and P. Costa, Philos. Mag. **24**, 1355 (1971).
7. D. J. Rowcliffe and G. Thomas, Mater. Sci. Eng. **18**, 231 (1975).
8. B. I. Markhasev, N. I. Pioro, V. V. Klyugvant, *et al.*, Izv. Akad. Nauk SSSR, Neorg. Mater. **18**, 2001 (1982).
9. B. I. Markhasev, N. I. Pioro, V. V. Klyugvant, *et al.*, Izv. Akad. Nauk SSSR, Neorg. Mater. **19**, 1997 (1983).
10. H. Wiesenberger, W. Lengauer, and P. Ettmayer, Acta Mater. **46**, 651 (1998).
11. I. Zaplatinsky, J. Am. Ceram. Soc. **49**, 109 (1966).
12. G. M. Demyashev, M. A. Khusainov, and R. K. Chuzhko, Izv. Akad. Nauk SSSR, Ser. Fiz. **48**, 1693 (1984).
13. M. A. Khusainov and D. M. Umidov, Izv. Akad. Nauk SSSR, Neorg. Mater. **21**, 147 (1985).
14. W. F. Brizes and J. M. Tobin, J. Am. Ceram. Soc. **50**, 115 (1967).

Translated by R. Tyapaev

JETP Letters, Vol. 82, No. 5, 2005, pp. 292–296. Translated from Pis'ma v Zhurnal Éksperimental'noĭ i Teoreticheskoĭ Fiziki, Vol. 82, No. 5, 2005, pp. 326–330.
Original Russian Text Copyright © 2005 by Sabinina, Gutakovskiĭ, Sidorov, Yakushev, Varavin, Latyshev.

Observation of Antiphase Domains in $Cd_xHg_{1-x}Te$ Films on Silicon by the Phase Contrast Method in Atomic Force Microscopy

I. V. Sabinina[a], **A. K. Gutakovskiĭ**[a], **Yu. G. Sidorov**[a], **M. V. Yakushev**[a],
V. S. Varavin[a], **and A. V. Latyshev**[a, b]
[a] *Institute of Semiconductor Physics, Siberian Division, Russian Academy of Sciences, Novosibirsk, 630090 Russia*
e-mail: sabinina@isp.nsc.ru
[b] *Novosibirsk State University, Novosibirsk, 630090 Russia*

Received July 11, 2005

It has been shown that phase contrast in atomic force microscopy (AFM) can be used to obtain adequate information on the density and distribution of antiphase domains on the surface of CdHgTe films grown by molecular beam epitaxy on a Si(301) substrate. By comparing the AFM phase images of the film surface with TEM images of structural defects in the near-surface region, the relation between microstructure and micromorphology of the films is revealed. *© 2005 Pleiades Publishing, Inc.*

PACS numbers: 68.37.–d, 68.47.Fg, 68.55.–a

Antiphase domains are structural defects of binary compounds or two-component ordered solid solutions whose crystal lattice can be considered as a superposition of two identical sublattices embedded into each other. For example, each compound of the A_3B_5 or A_2B_6 types has a sphalerite-type crystal lattice, which can be considered as a superposition of two face-centered sublattices. In such a structure, the A-type atoms occupy the nodes of one of the sublattices while the B-type atoms represent the nodes of the other sublattice. If, in some region of the crystal, the A and B atoms are interchanged, a so-called antiphase domain bounded by antiphase boundaries is formed. Inside the domain, all the chemical bonds and atomic positions correspond to a perfect structure. The structural defect is precisely the antiphase boundary, at which the interelement chemical bond is violated. Such defects may be distributed over the whole volume of a heteroepitaxial film and, hence, may strongly deteriorate the electrophysical and optical properties of the material and the instruments made on its basis. To eliminate these defects from the operating part of the material, it is necessary to investigate the basic laws and mechanisms of their formation. The first step in solving this problem is the development of an adequate express method for the detection and observation of antiphase boundaries in heteroepitaxial films.

According to experimental studies, antiphase boundaries can be observed in heteroepitaxy of binary semiconductor compounds on an elementary semiconductor: GaAs–Ge [1], GaP–Si [2], CdTe–Si [3], etc. In these studies, the main method used to observe the antiphase boundaries was transmission electron microscopy (TEM). The TEM technique provides maximum information on structural defects, including those on the atomic scale. At the same time, this technique is destructive and cannot be used as an express method in contrast to, e.g., atomic force microscopy (AFM). In our previous paper [4] devoted to studying the nature of V-shaped defects in CdHgTe films on GaAs(301), it was shown that a simultaneous application of TEM and AFM techniques makes it possible to determine the unique relationship between the micromorphological features of the growth surface of the film in the region of V-shaped defects and the internal structure of these defects. This information was used to reveal the mechanisms of the nucleation of V-shaped defects and served as the basis for the interpretation of the subsequent AFM data without any further use of TEM analysis.

This work is devoted to determining the relation between the micromorphology of the surface of $Cd_xHg_{1-x}Te$ films grown on Si(301) and the internal structure of these films. The purpose of this study is to reveal the characteristic features of the growth surface relief that are caused by the presence of antiphase domains in the film volume. To investigate the effect of antiphase domains on the electrophysical properties of the films, local electrophysical measurements were carried out in the regions of domain accumulations.

The samples were $Cd_xHg_{1-x}Te$ films grown by molecular beam epitaxy (MBE) on Si substrates with (301) orientation. The heteroepitaxial structure included a ZnTe buffer layer with a thickness of 100 nm, a CdTe buffer layer with a thickness of 6–8 μm, and a $Cd_{0.22}Hg_{0.78}Te$ film with a thickness of 10 μm. The MBE procedure used for growing heteroepitaxial structures on Si substrates was described in [5]. The micromorphology of the growth surface was studied by AFM with a Solver P-47H (Nt-MDT) microscope, and the defects in the film volume were studied by TEM with a JEM-4000EX (JEOL) electron microscope. For the TEM studies, the samples were prepared in the form of both thin foils parallel to the growth surface and transverse sections [6].

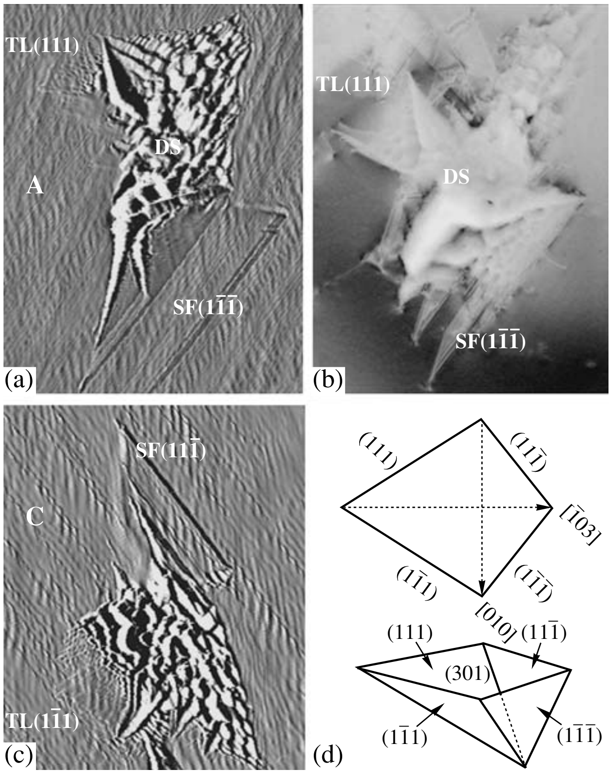

Fig. 1. Typical (a, c) 12 × 12 μm AFM images and (b) a TEM image of a V-shaped defect consisting of stacking faults (SF), twinning lamellas (TL), and a damaged structure region (DS) on the (301) surface of a CdHgTe film. Surface images of two antiphase domains: (a) A and (c) C. (d) The pyramid formed by the {111} planes and the quadrangle formed as a result of the intersection of this pyramid by the (301) surface.

To obtain thin foils that are transparent for an electron beam and lie in the plane parallel to the film surface, we developed an original method. We placed a Si/ZnTe/CdTe/CdHgTe heterostructure in a hot 30% KOH solution and waited until the silicon substrate was completely dissolved. Then, the remaining ZnTe/CdTe/CdHgTe film was washed and thinned by etching in a 1.5% solution of bromine in methanol.

The surface morphology was analyzed by AFM in the topographic and phase contrast modes simultaneously. The topographic mode provided the images of the three-dimensional surface relief, and the phase contrast allowed us to visualize the boundaries of antiphase domains and the stacking faults [7]. The phase contrast in AFM is associated with the frequency shift of natural oscillations of the tip (cantilever) touching the surface in the tapping mode [8]. Although the physical mechanism responsible for the phase shift has not yet been uniquely interpreted, tapping-mode AFM has received wide acceptance in studying surface inhomogeneities [9, 10].

According to AFM and TEM data, all of the CdHgTe films grown on Si(301) contain V-shaped defects similar to those observed in films of the same composition that were grown on GaAs(301). From the comprehensive analysis of these defects [4], it follows that V-shaped defects are complex objects containing damaged structure regions, twinning lamellas, and stacking faults. Figure 1 shows typical (a, c) AFM and (b) TEM images of V-shaped defects on the surface of a CdHgTe film grown on a Si(301) substrate. A comparison of these images allows us to determine the relation between the characteristic features of the relief in the region of the defect and the structure of the latter. Since the {111} planes play an important role in the formation of defects in A_2B_6 compounds, in Fig. 1d we schematically represent the pyramid that is formed by the {111} planes inclined to the (301) growth surface and the quadrangle that is formed by the traces of the intersections of the {111} planes with the (301) plane. In both AFM and TEM images, one can clearly see the characteristic elements of a V-shaped defect: the stacking faults, the twinning lamellas, and the damaged structure regions [4]. The stacking faults and the twinning lamellas grow from the central region (the damaged structure region) of a V-shaped defect along the tilted {111} planes. From the comparison of the defect images shown in Figs. 1a and 1b with the schematic diagram, it follows that these are the $(1\bar{1}\bar{1})$ planes, which form an angle of 68.58° with the (301) plane, and the (111) planes, which form an angle of 43.09° with the (301) plane. The TEM studies of transverse sections showed that almost all stacking faults observed in $Cd_xHg_{1-x}Te$ films lie in the planes intersecting the (301) surface at an angle of 68.58° and grow from the buffer layer. The stacking faults that lie in the planes making an angle of 43.09° with the (301) surface only occur in the region of a V-shaped defect.

Unlike the case of epitaxy on GaAs(301), for CdHgTe films grown on Si(301), the AFM data reveal two types of growth surface relief (Figs. 1a, 1c). The two images differ in the positions of V-shaped defects and stacking faults with respect to the base cut of the silicon crystal. The base cut coincides with the (100) plane, which intersects the (301) surface along the $[\bar{1}03]$ direction along which the scanning was performed. It should be noted that the position of the sample and the scanning direction were the same for each of the experiments. Multiple stacking faults that are denoted as $(1\bar{1}\bar{1})$ stacking faults in Fig. 1a lie in the $(1\bar{1}\bar{1})$ planes, while the $(11\bar{1})$ stacking faults in Fig. 1c

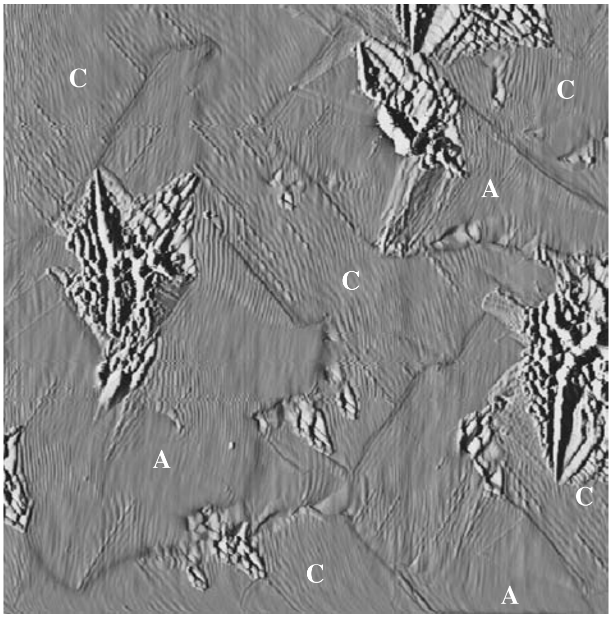

Fig. 2. 30 × 30 μm AFM image of the CdHgTe(301) surface containing antiphase domains of A and C types.

lie in the $(11\bar{1})$ planes. These kinds of stacking faults predominate in the films, whereas the (111) and $(1\bar{1}1)$ stacking faults only occur near a V-shaped defect, as one can see from Figs. 1a and 1c, respectively. In the tetrahedron formed by the {111} planes in Fig. 1d, the $(11\bar{1})$ and $(1\bar{1}\bar{1})$ planes are neighboring faces of different polarity. Does this mean that the stacking faults shown in Figs. 1a and 1c are of different polarity? The subsequent study of a great number of films gave a negative response to this question. It was found that a single film surface may simultaneously contain regions with morphological features characteristic of the films shown in Figs. 1a and 1c. We will call these regions domains. Figure 2 shows an AFM image of the surface of a $Cd_xHg_{1-x}Te$ film with domains. The surface morphology of domains denoted by A and C corresponds to the surface morphology of the films shown in Figs. 1a and 1c, respectively. This is confirmed by the direction of the stacking faults and the geometry of V-shaped defects. Thus, for the ZnTe/CdTe/CdHgTe heterostructure on the Si surface, two positions (two types of domains), shown in Figs. 1a and 1c, are possible. According to AFM data, when the heterostructure is grown on a GaAs(301) substrate, it can occupy only one position, which corresponds to Fig. 1c. It should be noted that, if we rotate the surface image shown in Fig. 1a about the $(\bar{1}03)$ axis through 180°, we obtain the surface image shown in Fig. 1c. This symmetry operation relates the antiphase domains.

The crystallographic relation between domains of A and C types can be determined with the use of TEM. For the TEM observation of antiphase domains, it is convenient to use CdTe/ZnTe/Si films, because they contain no V-shaped defects, which hinder the preparation of thin foils along the growth surface.

Figure 3 shows the TEM images of the near-surface region of a CdTe film with domains, which were obtained at the (100) pole. Microdiffraction patterns obtained from domain types A and C completely coincide, which testifies to the absence of rotations of the crystal lattices in the corresponding regions. From the TEM image shown in Fig. 3c with high magnification,

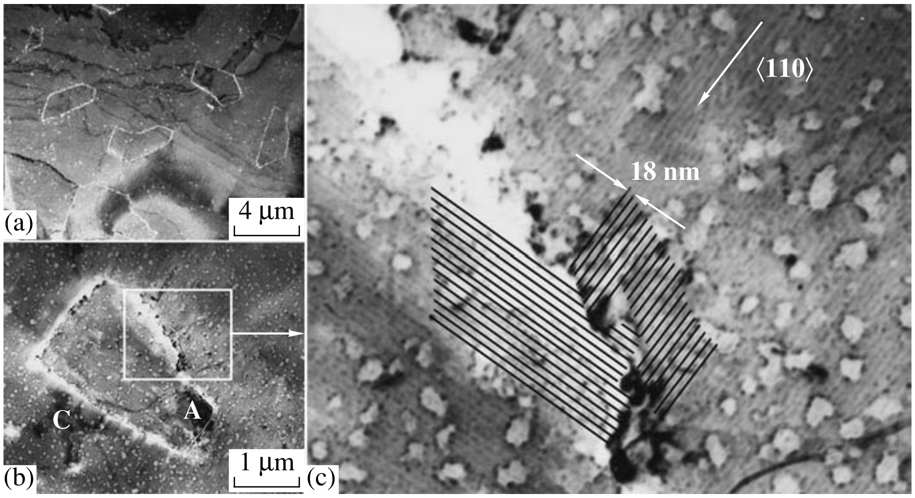

Fig. 3. (a, b) TEM images of the near-surface region of a CdTe film containing antiphase domains of A and C types, respectively; the images are obtained at the (100) pole. (c) Linear inhomogeneities along the ⟨110⟩ direction at the boundary between two domains.

one can see that, in neighboring domains, mutually perpendicular fringes occur along the ⟨110⟩ directions with a period of about 18 nm. The dotted contrast observed along the fringes may be caused by the decoration of the most active growth areas of the CdTe film surface. The nature of the separated linear inhomogeneities and the nature of the decorating particles are not discussed in this paper. The analysis of the surface images obtained at the (301) and (100) poles suggests that the direction of the separated lines coincides with the traces of the intersections of the (110) planes with the film surface. Since, in the course of MBE growth, the surface of CdTe is usually terminated by a single sort of atom, the fact that the separated lines in the domains are mutually perpendicular (when observed at the (100) pole) means that the domains are antiphase. According to [1], in similar heterosystems, antiphase domains are formed in the case of the layer-by-layer growth on a substrate whose surface contains steps equal to an odd number of atoms in height. A fault in the periodic series of ordered atomic planes gives rise to an antiphase boundary. As the film grows, the antiphase boundary may transform into an interlayer with a damaged structure, which stimulates the nucleation of V-shaped defects under nonoptimal conditions of epitaxial growth. Figure 2 illustrates the initial stage of the V-shaped defect nucleation: the formation of regions with damaged structure along the antiphase boundaries.

The fact that antiphase boundaries actually are damaged structure interlayers with an excess Te content was used by us to reveal the antiphase domains by chemical etching in a selective etchant. The procedure is as follows. The sample is first heated in a KOH solution during 10–15 min. Then, the sample is washed in water and placed in the 1.5% Br + HBr solution for several seconds. After such a processing, the observation of antiphase domains becomes possible with an optical microscope (Fig. 4). From studying a great number of samples, we found that the film parts containing antiphase domains with a density corresponding to that in Fig. 4 are visualized as mat areas on CdHgTe film surfaces.

The possibility to visualize specific structural defects in atomic force and optical microscopes allows us to obtain the information on the density of these defects and on their distribution over the epitaxial film surface. This makes it possible to perform local electrophysical measurements in the regions with high defect density or in the defect-free regions. From local Hall measurements, we found that, in the film areas where the density of antiphase domains was 10^6 cm^{-2}, the mobility of charge carriers was an order of magnitude lower than the mobility observed in the domain-free parts of the same film. This testifies to the scattering of charge carriers by the antiphase boundaries. At the same time, the measurements of electrophysical parameters performed for a great number of samples showed the absence of explicit dependences of the concentration, mobility, and lifetime of carriers on the domain type (A or C in Fig. 2) and on the density of stacking faults within 10^6–10^8 cm^{-2}.

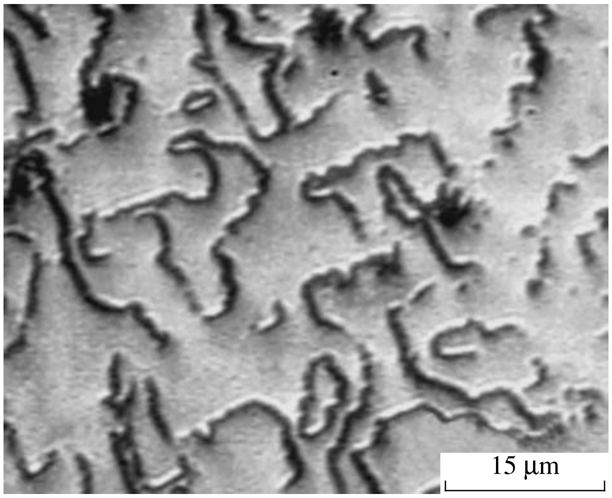

Fig. 4. Antiphase boundary image obtained with an optical microscope after chemical processing.

Thus, the combined observation of the same defects by AFM and TEM allowed us to determine the relation between the micromorphology and microstructure of $Cd_xHg_{1-x}Te$ films on Si substrates with the (301) orientation. We demonstrated the possibility of using the phase contrast in AFM for obtaining adequate information on the density and the character of distribution of antiphase domains, stacking faults, and V-shaped defects on the surface of an epitaxial film. We found that a ZnTe/CdTe/CdHgTe heteroepitaxial film can lie on the Si surface in two positions corresponding to two antiphase domains. The ZnTe/CdTe/CdHgTe heterostructure may occupy the position of one of the antiphase domains or may form a combination of different antiphase domains. The size of antiphase domains may vary from 1 μm to several hundreds of microns. We presented original methods for preparing thin foils suitable for TEM studies and methods for revealing antiphase boundaries by selective etching to make them observable with an optical microscope. The possibility to visualize antiphase domains by both optical and atomic force microscopes allowed us to investigate the effect of antiphase boundaries on the electrophysical properties of the samples. It was found that the concentration, mobility, and lifetime of charge carriers do not depend on the type of antiphase domains and on the density of stacking faults within 5×10^6–10^8 cm^{-2}. The appearance of antiphase domains with a density of 10^6 cm^{-2} reduces the mobility of charge carriers by an order of magnitude.

We are grateful to D.V. Shcheglov for assistance in the AFM studies.

REFERENCES

1. A. K. Gutakovsky, A. V. Katkov, M. I. Katkov, *et al.*, J. Cryst. Growth **201/202**, 232 (1999).
2. V. Narayanan, S. Mahajan, K. J. Bachmann, *et al.*, Acta Mater. **50**, 1275 (2002).
3. D. J. Smith, S.-C. Y. Tsen, D. Chandrasekhar, *et al.*, Mater. Sci. Eng. B **77**, 93 (2000).
4. I. V. Sabinina, A. K. Gutakovskii, Yu. G. Sidorov, and A. V. Latyshev, J. Cryst. Growth **274**, 339 (2005).
5. Yu. G. Sidorov, M. V. Yakushev, D. N. Pridachin, *et al.*, Thin Solid Films **367**, 203 (2000).
6. I. V. Sabinina and A. K. Gutakovsky, Ultramicroscopy **45**, 411 (1992).
7. A. V. Latyshev, D. V. Sheglov, S. S. Kosolobov, and E. E. Rodyakina, Microsc. Anal. **5** (2005) (in press).
8. Q. Zhong, D. Inniss, and V. B. Elings, Surf. Sci. **290**, L688 (1993).
9. J. P. Cleveland, B. Anczykowski, E. Schmid, and V. Elings, Appl. Phys. Lett. **73**, 2926 (1998).
10. B. Anczykowski, B. Gotsmann, H. Fuchs, *et al.*, Appl. Surf. Sci. **140**, 376 (1999).

Translated by E. Golyamina

JETP Letters, Vol. 82, No. 5, 2005, pp. 297–301. From Pis'ma v Zhurnal Éksperimental'noĭ i Teoreticheskoĭ Fiziki, Vol. 82, No. 5, 2005, pp. 331–335.
Original English Text Copyright © 2005 by Arseyev, Maslova.

Effects of Electron–Phonon Interaction in Tunneling Processes in Nanostructures[¶]

P. I. Arseyev[a] and N. S. Maslova[b]
[a] *Lebedev Physical Institute, Russian Academy of Sciences, Moscow, 119991 Russia*
e-mail: ars@lpi.ru
[b] *Faculty of Physics, Moscow State University, Moscow, 119992 Russia*

Received July 12, 2005

Tunneling through a system with two discrete electron levels coupled by electron–phonon interaction is considered. The interplay between elastic and inelastic tunneling channels is analyzed not only for weak electron–phonon coupling but also for strong coupling in the resonant case. It is shown that the intensity and width of peaks in the tunneling conductivity is strongly influenced by nonequilibrium effects. *© 2005 Pleiades Publishing, Inc.*

PACS numbers: 73.40.Gk, 73.63.–b

Recently, much attention has been given to both experimental and theoretical investigations of kinetic processes in nanostructures, in connection with the possible fabrication of ultrasmall electronic devices. The electron–phonon interaction is one of the important effects which influence the transport properties of various nanostructures, including structures with a quantum dot or a single molecule placed in tunneling contact between the leads. On the other hand, scanning tunneling microscopy (STM) investigation of single molecules on a surface is a powerful method of diagnostics of electron structure changes of adsorbed molecules [1]. One of the important characteristics of these changes is the modification of the vibrational modes of an adsorbed molecule. Thus, inelastic tunneling measurements can give information about the type of molecule bonding to the surface. Electron–phonon interaction is also very important in STM experiments concerning the problem of a single atomic (molecular) switch, in which atoms or molecules are transferred from one state to another by a tunneling current [2]. The development of a theoretical description should clarify the role of the electron–phonon interaction in kinetic processes in nanostructures and help to further progress in this field.

In a number of papers, electron–phonon interaction in tunneling structures is described within the most simple model for an intermediate system with a single electron level coupled with a phonon mode ([3–5]). If interaction with the leads is omitted, then this model has an exact solution [6]. But this model cannot be derived consistently from the many-body theory of condensed matter (see, e.g., [7]) and thus seems to be unrealistic.

We discuss a different model, which can be argued to be more physically justified for various systems, with electron transitions between two levels, accompanied by emission or absorption of a phonon (vibrational quantum). This model allows one to describe the interplay between two tunneling channels coupled by the electron–phonon interaction. The influence of such interplay on the tunneling spectra of semiconductor structures with 2D electron layers has been revealed in recent experiments [8]. It was found that tunneling spectra essentially change their shape when the intersubband electron transition energy was close to the LO phonon frequency.

In the present paper, we consider the simplest system of this kind, which is described by a Hamiltonian of the following type:

$$\hat{H} = \hat{H}_{\text{dot}} + \hat{H}_{\text{tun}} + \hat{H}_0. \tag{1}$$

The part $\hat{H}_{\text{dot}}$ corresponds to the intermediate subsystem in which we take into account two localized states and interaction transitions induced by electron–phonon between these two states:

$$\hat{H}_{\text{dot}} = \sum_{i=1,2} \varepsilon_i a_i^+ a_i + g(a_1^+ a_2 + a_2^+ a_1)(b + b^+) + \omega_0 b^+ b, \tag{2}$$

where ε_i corresponds to discrete levels in a quantum dot (or two-electron states in a molecule), ω_0 is the optical phonon frequency (or molecular vibrational mode), and g is the electron–phonon coupling constant. Tunneling

---

[¶] The text was submitted by the authors in English.

transitions from the intermediate system are included in

$$\hat{H}_{\text{tun}} = \sum_{\mathbf{p},\, i\,=\,1,\,2} T_{\mathbf{p},\,i}(c_{\mathbf{p}}^{+}a_i + \text{h.c.}) + \sum_{\mathbf{k},\, i\,=\,1,\,2} T_{\mathbf{k},\,i}(c_{\mathbf{k}}^{+}a_i + \text{h.c.}). \tag{3}$$

The free-electron spectrum in the left and right electrodes (**k** and **p**) includes the applied bias V:

$$\hat{H}_0 = \sum_{\mathbf{k}}(\varepsilon_k - \mu)c_{\mathbf{k}}^{+}c_{\mathbf{k}} + \sum_{\mathbf{p}}(\varepsilon_p - \mu - eV)c_{\mathbf{p}}^{+}c_{\mathbf{p}}. \tag{4}$$

The operators $c_{\mathbf{k}}$ and $c_{\mathbf{p}}$ correspond to electrons in the leads, and a_i, to electrons at the localized states of the intermediate system with energy ε_i.

By means of the Keldysh diagram technique, the tunneling current through such a structure is determined as

$$I(V) = \sum_{\mathbf{k},\, i\,=\,1,\,2} \int d\omega T_{\mathbf{k}i}(G^{<}_{i\mathbf{k}} - G^{<}_{\mathbf{k}i}). \tag{5}$$

The expression for the tunneling current can be rewritten in a form containing only Green's functions of the intermediate subsystem [9, 10]:

$$I(V) = 2\sum_{i\,=\,1,\,2} \gamma_i^k \int [2\operatorname{Im}G_i^R(\omega)n_k^0(\omega) - iG_{ii}^{<}(\omega)]d\omega, \tag{6}$$

where $\gamma_i^k = T_{\mathbf{k}i}T_{i\mathbf{k}}\nu_{\mathbf{k}}(\omega)$, $\nu_{\mathbf{k}}(\omega)$ is the density of states in the left electrode and $n_k^0(\omega)$ is the equilibrium filling number in the left electrode.

The main problem is to calculate the Green's functions for the intermediate system in the presence of both the tunneling coupling and electron–phonon interaction. The equations for $G_{i,\,j}^{R,\,A}$ are now coupled with the equations for $G_{i,\,j}^{<}$ due to electron–phonon interaction. The equations for $G_{i,\,j}^{R,\,A}$ as usual describe the modifications of electron spectral functions (density of states), but in this case they depend on electron filling numbers, determined by the kinetic processes. For an arbitrary ratio of the electron–phonon coupling constant g to the tunneling rates γ, this is a strongly correlated system which cannot be solved exactly. The situation is analogous to the widely discussed Hubbard-Anderson model.

The theory can be developed in two limiting cases: $g \ll \gamma$ and $g \gg \gamma$. In the present work, we shall not discuss nonequilibrium phonon effects and suppose that the phonon subsystem remains unperturbed by tunneling processes.

In the limit of weak electron–phonon interaction, $g \ll \gamma$, we can calculate $\operatorname{Im}G_i^R(\omega)$ and $G_{ii}^{<}(\omega)$ as perturbation series in g. The first term is

$$\begin{aligned} G_{11}^{<}(\omega) &= G_1^R(\omega)\Sigma_{11}^R(\omega)G_1^{<}(\omega) \\ &- G_1^R(\omega)\Sigma_{11}^{<}(\omega)G_1^A(\omega) + G_1^{<}(\omega)\Sigma_{11}^A(\omega)G_1^A(\omega), \end{aligned} \tag{7}$$

$$G_{11}^R(\omega) = G_1^R(\omega)\Sigma^R(\omega)G_1^R(\omega). \tag{8}$$

All the Green's function are calculated for the tunneling problem without electron–phonon interaction:

$$\begin{aligned} G_i^R(\omega) &= \frac{1}{\omega - \varepsilon_i + i(\gamma_i^p + \gamma_i^k)}, \\ G_i^{<}(\omega) &= -2in_i(\omega)\operatorname{Im}G_i^R(\omega), \end{aligned} \tag{9}$$

where the nonequilibrium filling number $n_i(\omega) = (\gamma_i^p n_p^0(\omega) + \gamma_i^k n_k^0(\omega))/(\gamma_i^p + \gamma_i^k)$, and $\Sigma(\omega)$ is the simplest self-energy part due to the electron–phonon interaction:

$$\begin{aligned} \Sigma_{11}^R(\omega) &= ig^2\int[D^R(\omega')G_2^{<}(\omega - \omega') \\ &+ D^{>}(\omega')G_2^R(\omega - \omega')]d\omega', \end{aligned} \tag{10}$$

$$\Sigma_{11}^{<}(\omega) = -ig^2\int D^{<}(\omega')G_2^{<}(\omega - \omega')d\omega'. \tag{11}$$

The first-order contribution to the tunneling current can be divided into two different parts: $I = I_1 + I_2$. The first corresponds to small changes in electron density of states due to electron–phonon interaction and is described simply by some corrections to G_{ii}^R:

$$\begin{aligned} I_1 &= \int\left[\frac{\gamma_1^k\gamma_1^p}{(\gamma_1^p + \gamma_1^k)}2\operatorname{Im}G_{11}^{(1)R}(\omega)\right. \\ &+ \left.\frac{\gamma_2^k\gamma_2^p}{(\gamma_2^p + \gamma_2^k)}2\operatorname{Im}G_{22}^{(1)R}(\omega)\right](n_k^0(\omega) - n_p^0(\omega))d\omega. \end{aligned} \tag{12}$$

The second contribution is more interesting, because it describes inelastic tunneling processes with emission or absorption of a phonon:

$$\begin{aligned} I_2 &= 4\pi g^2\frac{\gamma_1^k\gamma_2^p - \gamma_2^k\gamma_1^p}{(\gamma_1^p + \gamma_1^k)^2(\gamma_2^p + \gamma_2^k)^2} \\ &\times\int d\omega\operatorname{Im}G_{11}^R(\omega)(n_k^0(\omega) - n_p^0(\omega)) \\ &\times[\operatorname{Im}G_{22}^R(\omega + \omega_0)(\gamma_1^k\gamma_2^p n_p^0(\omega + \omega_0) \\ &- \gamma_2^k\gamma_1^p n_k^0(\omega + \omega_0) + (\gamma_1^k\gamma_2^p - \gamma_2^k\gamma_1^p)N(\omega_0)) \\ &- \operatorname{Im}G_{22}^R(\omega - \omega_0)(\gamma_1^k\gamma_2^p n_p^0(\omega - \omega_0) \\ &- \gamma_2^k\gamma_1^p n_k^0(\omega - \omega_0) + (\gamma_1^k\gamma_2^p - \gamma_2^k\gamma_1^p)N(-\omega_0))]. \end{aligned} \tag{13}$$

The sign of this additional correction to the total current depends on the ratio between the four tunneling rates γ_1^k, γ_1^p, γ_2^k, γ_2^p. The physical reason why the electron–phonon interaction can either increase or decrease the tunneling current is connected with interference effects between direct and indirect tunneling channels. It becomes more obvious if we notice that

$$\frac{\gamma_1^k\gamma_2^p - \gamma_2^k\gamma_1^p}{(\gamma_1^p + \gamma_1^k)(\gamma_2^p + \gamma_2^k)}(n_k^0(\omega) - n_p^0(\omega)) = n_1(\omega) - n_2(\omega).$$

Thus, the inelastic processes increase the total current if the inverse population of our two-level system appears due to elastic tunneling. Two examples which demonstrate enhancement and suppression effects in the tunneling conductivity are shown in Fig. 1.

In the limit of small tunneling coupling to the leads so that all $\gamma \ll g$, we use a perturbation treatment of tunneling processes in small parameter γ/g. For the most interesting case, when phonon frequency is close to the resonance with electron transition energy $\varepsilon_1 - \varepsilon_2 \simeq \omega_0$, we can retain in the Hamiltonian only the following interactions as the most important (similar to the rotating-wave approximation for two-level systems):

$$\hat{H}_{\text{el–phon}} = g(a_1^+ a_2 b + a_2^+ a_1 b^+).$$

Direct calculation of dot (molecule) Green's functions G_{11}^R, G_{22}^R based on the Heisenberg equations for isolated dot (molecule) leads to the system of equations

$$(\omega - \varepsilon_1)G_{01}^R - gG_{2b1}^R = 1,$$

$$(\omega - \varepsilon_2 - \omega_0)G_{2b1}^R - gG_{2n1}^R = 0,$$

$$(\omega - \varepsilon_1)G_{2n1}^R - g(N+1)G_{2b1}^R = 1 - n_2 + N,$$

where the new functions G_{2b1}^R, G_{2n1}^R are introduced:

$$G_{2b1}^R = i\theta(t-t')\langle[a_2(t)b(t), a_1^+(t')]\rangle,$$

$$G_{2n1}^R = i\theta(t-t')$$
$$\times\langle[a_1(t)(b(t)b^+(t) - a_2^+(t)a_2(t)), a_1^+(t')]\rangle.$$

N and n_2 are the number of phonons and electrons at the second level, respectively. At the third step, the mean value of phonon filling number is decoupled from the average $\langle a_2b(1 + b^+b), a_1^+\rangle \longrightarrow \langle a_2b, a_1^+\rangle(N+1)$. After this approximation is performed, the retarded Green's function is determined:

$$G_{01}^R = \frac{1}{(\omega - \varepsilon_1)}$$
$$\times\left[1 + \frac{g^2(N+1-n_2)}{((\omega-\varepsilon_1)(\omega-\varepsilon_2-\omega_0) - g^2(N+1))}\right]. \tag{14}$$

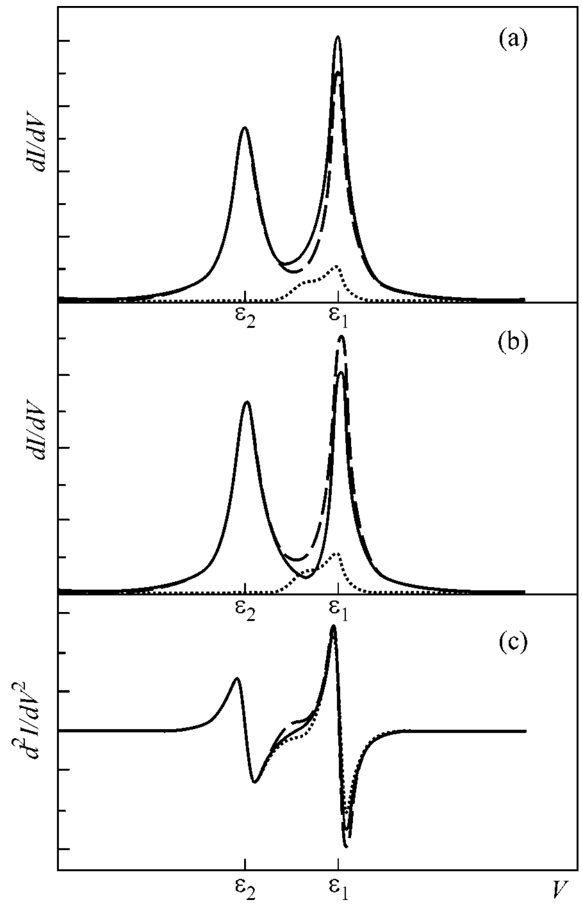

Fig. 1. Tunneling conductivity spectra for weak election–phonon coupling. Elastic and inelastic contributions and total tunneling conductivity are shown in Fig. 1 (a) and (b) by dashed, dotted, and solid curves, respectively. Values of the parameters are $\varepsilon_1 - \varepsilon_2 = 1$, $\omega_0 = 0.6$, $g = 0.4$. (a) $\gamma_1^k\gamma_1^p \gg \gamma_2^k\gamma_1^p$; (b) $\gamma_1^k\gamma_2^p \ll \gamma_2^k\gamma_1^p$ Phonon-induced structure is more pronounced in d^2I/dV^2 as shown in (c) by dashed line for case "a" and by dotted line for case "b"; solid line corresponds to elastic part of the current.

The same procedure for the second level gives

$$G_{02}^R = \frac{1}{(\omega - \varepsilon_2)}$$
$$\times\left[1 + \frac{g^2(N+n_1)}{((\omega-\varepsilon_2)(\omega-\varepsilon_1+\omega_0) - g^2(N+1))}\right].$$

We see that new poles in the Green's functions have appeared, which corresponds to splitting of two resonantly close pairs of levels: ε_1 and $\varepsilon_2 + \omega_0$, as well as ε_2 and $\varepsilon_1 - \omega_0$. We can expect the appearance of three resonant peaks in the local density of states near ε_1 and ε_2. Note that the energies of the two split states depend on the temperature through the phonon filling number N.

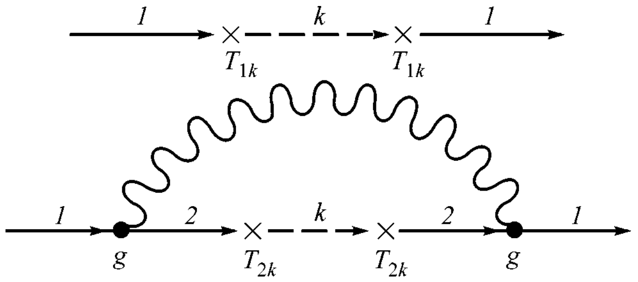

Fig. 2. Two first-order diagrams for the self-energy part Σ_{11}. Dashed line denotes electron Green's function in the leads, wavy line denotes phonon Green's function.

Now we treat as the first-order perturbation the self-energy parts of two kinds, appearing due to the tunneling coupling with the leads (see Fig. 2).

Tunneling current is determined by the self-energies as

$$I = 2\sum_{i=1,2}\gamma_i^k\int[G_i^R(\omega)(-i\Sigma_{ii}^<(\omega))G_i^A(\omega)$$
$$+ n_k^0(\omega)G_i^R(\omega)\mathrm{Im}\Sigma_{ii}^R(\omega)G_i^A(\omega)]d\omega.$$

The contribution of the first diagram is rather simple

$$I_1 = \int[\gamma_1^k\gamma_1^pG_1^R(\omega)G_1^A(\omega) + \gamma_2^k\gamma_2^pG_2^R(\omega)G_2^A(\omega)]$$
$$\times(n_k^0(\omega) - n_p^0(\omega))d\omega.$$

The contribution described by the second diagram reduces in the first nonvanishing order in $(\gamma/g)^2$ to the following form:

$$I_2 = g^2\int d\omega\left|G_1^R(\omega)\right|^2\left|G_2^R(\omega-\omega_0)\right|^2(n_k^0(\omega) - n_p^0(\omega))$$
$$\times(\gamma_1^k\gamma_2^p(n_p^0(\omega-\omega_0) - N(\omega_0) - 1)$$
$$+ \gamma_2^k\gamma_1^p(n_k^0(\omega-\omega_0) - (N(\omega_0) - 1)).$$

It is important that functions G_i^R are determined with the help of Eq. (14):

$$[G_i^R]^{-1} = [G_{0i}^R]^{-1} + i(\gamma_i^k + \gamma_i^p).$$

This expression allows us to estimate the effective width of each of the three resonant peaks near the initial electron levels. It is remarkable that broadening of these peaks is different and depends on nonequilibrium electron numbers; it can thus be tuned by changing the parameters of the tunneling contact. The peak corresponding to ε_1 has the effective width $\Gamma_1^0 = (\gamma_1^k + \gamma_1^p)n_2/(N + 1)$. The two split peaks near it have the width $\Gamma_1^\pm = (\gamma_1^k + \gamma_1^p)(N + 1 - n_2)/2(N + 1)$. The same

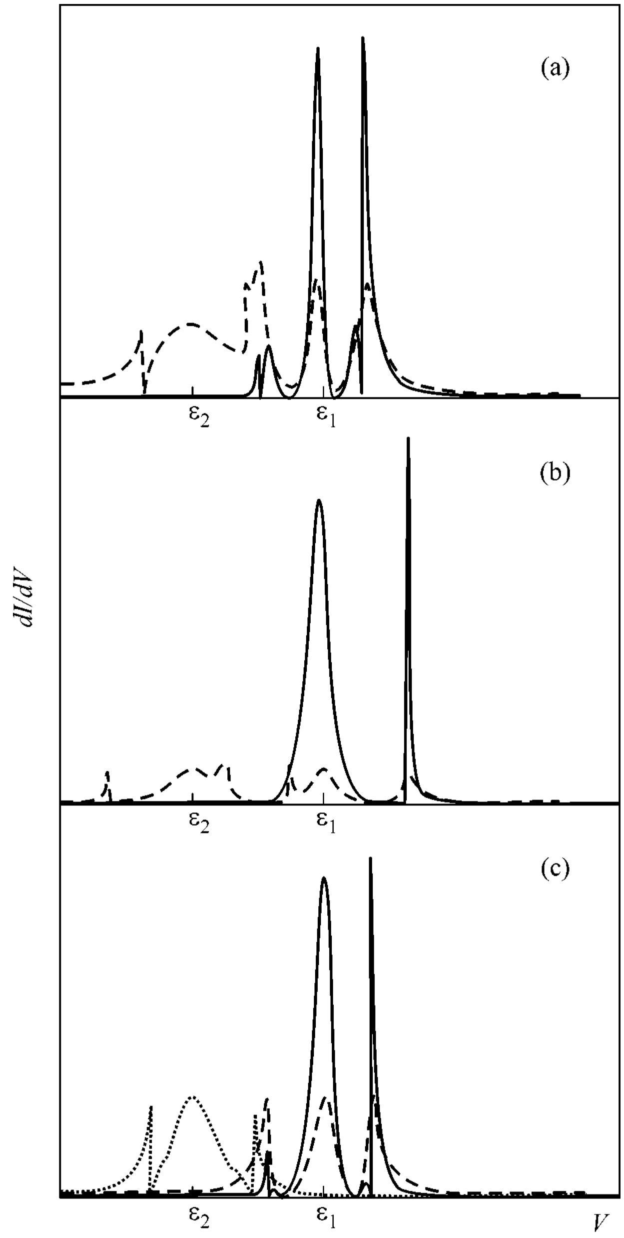

Fig. 3. Tunneling conductivity spectra for strong resonant electron phonon coupling. Elastic and inelastic contributions to the tunneling conductivity are shown by dashed and solid curves respectively. Chosen values of the parameters are $\varepsilon_1 - \varepsilon_2 = 1$, $\omega_0 = 0.9$, $g = 0.4$. (a) $\gamma_2^k = 0.3$, $\gamma_2^p = 0.06$; (b) $\gamma_2^k = 0.06$, $\gamma_2^p = 0.3$; (c) $\gamma_2^k = \gamma_2^p = 0.1$. In (c), elastic tunneling current through each electron level is shown separately by dotted and dashed curves.

values for the second set of peaks near ε_2 are $\Gamma_2^0 = (\gamma_2^k + \gamma_2^p)(1 - n_1)/(N + 1)$, $\Gamma_2^\pm = (\gamma_2^k + \gamma_2^p)(N + n_1)/2(N + 1)$.

Some tunneling conductivity curves for zero temperature ($N = 0$) are shown in Fig. 3. In this figure we consider the case when both levels ε_1 and ε_2 lie above the Fermi level at zero applied bias voltage.

Let us point out the most interesting features of the tunneling conductivity behavior in this case. For the elastic channel in the tunneling conductivity spectra, nonequilibrium narrowing of the two split peaks near ε_2 is always clearly seen, while the peak at initial energy ε_2 is broadened in the usual way by the tunneling rates. In the bias range close to ε_1, we can distinguish two different cases dependent on the ratio between the tunneling rates, because it determines the filling number of the deeper state ε_2. For $\gamma_2^k \ll \gamma_2^p$, two split peaks near ε_1 are narrow, and the tunneling conductivity peak at a bias voltage equal to the initial level ε_1 has the usual tunneling width (Fig. 3).

For $\gamma_2^k \gg \gamma_2^p$ the split peaks are broadened up to the usual tunneling width and peak at a bias voltage equal to the initial level ε_1. For a sufficiently strong electron–phonon coupling, the contribution of the inelastic channel to the tunneling conductivity can strongly exceed the elastic channel's contribution at a certain bias close to ε_1. The tunneling conductivity peaks of the inelastic channel are narrow due to nonequilibrium effects.

At high temperature, when $N \gg 1$, the shape of the tunneling conductivity curves are not so sensitive to the ratio between different tunneling rates. One should observe very narrow peaks at ε_1 and ε_2, while the broadening of split peaks is always equal to one half of the usual tunneling width.

CONCLUSIONS

In the weak electron–phonon coupling limit, we revealed that interference effects between various channels can lead either to a certain increase in the total current or to its suppression. The sign of the resulting effect depends on the ratios between the tunneling rates.

For tunneling rates which are too large, observation of inelastic peaks in the tunneling conductivity spectra is nearly impossible.

For strong electron–phonon coupling, three peaks can arise in the tunneling conductivity spectra near each electron level in the resonant situation. Nonequilibrium narrowing of these peaks at a certain ratio between the tunneling rates is discovered. The positions of satellite peaks in this case are determined not only by the phonon frequency ω_0 but also by the electron–phonon coupling constant and the temperature.

An important feature of the system under consideration is that we can change the relative intensity and width of elastic and inelastic peaks by tuning the tunneling coupling of the intermediate system with the leads.

This research was supported by the Russian Foundation for Basic Research, project nos. 03-02-16807 and 04-02-19957, the Leading Scientific Schools program, project no. 1909.2003.2, and the Russian Academy of Sciences program "Strongly correlated electrons in metals, semiconductors, and superconductors." Support from the Samsung Corporation is also gratefully acknowledged.

REFERENCES

1. L. H. Yu, Z. K. Keane, J. W. Ciszek, *et al.*, Phys. Rev. Lett. **93**, 266802 (2004).
2. D. M. Eigler, C. P. Lutz, and W. E. Rudge, Nature **352**, 600 (1991).
3. B. N. J. Persson and A. Baratoff, Phys. Rev. Lett. **59**, 339 (1987).
4. S. G. Tikhodeev and H. Ueba, Phys. Rev. B **70**, 125414 (2004).
5. D. A. Ryndyk and J. Keller, cond-mat/0406181.
6. G. D. Mahan, *Many Particle Physics*, 3rd ed. (Plenum, New York, 2000).
7. M. Born and K. Huang, *Dynamical Theory of Crystal Lattices* (Oxford Univ. Press, London, 1954; Inostrannaya Literatura, Moscow, 1958).
8. I. N. Kotel'nikov and S. E. Dizhur, Pis'ma Zh. Éksp. Teor. Fiz. **81**, 574 (2005) [JETP Lett. **81**, 458 (2005)].
9. Y. Meir and N. S. Wingreen, Phys. Rev. Lett. **68**, 2512 (1992).
10. P. I. Arseev and N. S. Maslova, Zh. Éksp. Teor. Fiz. **102**, 1056 (1992) [Sov. Phys. JETP **75**, 575 (1992)].

JETP Letters, Vol. 82, No. 5, 2005, pp. 302–305. Translated from Pis'ma v Zhurnal Éksperimental'noĭ i Teoreticheskoĭ Fiziki, Vol. 82, No. 5, 2005, pp. 336–340.
Original Russian Text Copyright © 2005 by Zinov'eva, Nenashev, Dvurechenskiĭ.

Hole Spin Relaxation in Ge Quantum Dots

A. F. Zinov'eva*, A. V. Nenashev, and A. V. Dvurechenskiĭ
Institute of Semiconductor Physics, Siberian Division, Russian Academy of Sciences, Novosibirsk, 630090 Russia
** e-mail: aigul@isp.nsc.ru*

Received July 12, 2005

Hole spin relaxation in an isolated Ge quantum dot due to interaction with phonons is investigated. Spin relaxation in this case occurs through the mechanism of the modulation of the spin–orbit interaction by lattice vibrations. According to the calculations performed, the spin relaxation time due to direct single-phonon processes for the hole ground state equals 1.4 ms in the magnetic field $H = 1$ T at the temperature $T = 4$ K. The dependence of the relaxation time on the magnetic field is described by the power function H^{-5}. At higher temperatures, a substantial contribution to spin relaxation is made by two-phonon (Raman) processes. Because of this, the spin relaxation time decreases to nanoseconds as the temperature is raised to $T = 20$ K. Analysis of transition probabilities shows that the third and twelfth excited hole states, which are intermediate in two-step relaxation processes, play the main part in Raman processes. *© 2005 Pleiades Publishing, Inc.*

PACS numbers: 71.70.Ej, 72.25.Rb, 73.21.La

At present, spin phenomena in nanostructures are considered to be one of the topical problems of modern solid state physics. This area of study has received the separate name "spintronics," which is associated with the potential application of the spin degree of freedom for quantum computations and for the creation of data storage devices. Ge/Si-based heterostructures are the most promising for the use of the spin degree of freedom, because the spin–lattice relaxation time T_1 in Si is 1–10 h at helium temperatures [1] and the dephasing time T_2 equals several milliseconds [2]. In Ge at the same temperatures, the times T_1 and T_2 are of the same order and equal several milliseconds [3].

Ge/Si quantum dots are formed in the course of Ge heteroepitaxy on a Si substrate when, under certain conditions, a transition occurs from the two-dimensional layer-by-layer mechanism of Ge film growth to three-dimensional growth. The characteristic size of islands is 10–20 nm, and their height is 1–2 nm; thus, the behavior of charge carriers in these islands is determined by quantum size effects [4]. The existing energy band discontinuity and deformation effects lead to the formation of a potential well in Ge for holes. Recent investigations have shown that the spin relaxation time increases as the dimensionality of the system decreases [5, 6]. The matter of fact is that the mechanisms associated with quasimomentum scattering become less effective in low-dimensionality systems upon freezing degrees of freedom. Thus, for example, the Dyakonov–Perel mechanism becomes less effective in the case of two-dimensional systems. As the dimensionality further decreases to zero-dimensional objects, the spin relaxation time further increases. The possibility that the spin orientation is retained for a long time is important for the creation of devices that use the spin degree of freedom. Schemes for the implementation of quantum computations using quantum dots [7] and such devices as spin transistors and spin filters based on quantum dots [8] have been proposed to date.

This work presents calculated results for the spin relaxation time of hole states due to interaction with phonons in an isolated Ge quantum dot in a magnetic field. In addition to phonons, a spin flip can be induced by the magnetic field created by nuclear spins [9, 10], as well as by processes that proceed upon hole tunneling from one quantum dot to another [11]. However, there are conditions at which the phonon mechanism of spin relaxation predominates. Tunneling processes can contribute to spin relaxation only in sufficiently dense quantum dot arrays and only for carriers with energy close to the Fermi level. Interaction with nuclear spins (hyperfine interaction) becomes determining only in the case when the external magnetic field is sufficiently small as compared with the field of nuclear spins. For estimation, experimental data on InP quantum dots [12] can be used, in which the effect of electron spin dephasing by nuclear spins is suppressed in the external magnetic field > 0.1 T. For Ge/Si dots, this value can be considered as an upper estimate, because the nuclear momenta of In and P are considerably larger than the nuclear momenta of Ge and Si [13]. The role of hyperfine interaction in Ge/Si quantum dots will be considered in more detail in the subsequent publications.

The nature of the spin relaxation through interaction with phonons is in the fact that lattice vibrations lead to modulation of spin–orbit interaction. Spin–orbit interaction becomes time-dependent, which eventually leads to spin relaxation. Spin–orbit interaction plays a significant role in the formation of the valence band structure and in the spin relaxation of holes in bulk semiconductors. The value of the spin–orbit interaction in Ge (~0.3 eV) is comparable with the quantization energy of Ge in the quantum dot. Therefore, it significantly affects the electronic structure in the Ge quantum dot. For this reason, we suggest that this mechanism of spin relaxation is the main mechanism at helium temperatures.

The calculations were performed for a particular geometry of the quantum dot: a pyramid with a square base and a height ten times smaller than the base side. The choice of the geometry was based on the data of investigations using scanning tunneling microscopy (STM) and high-resolution transmission electron microscopy (HRTEM) [14]. The problem was solved within the framework of the tight-binding method and was mainly based on our previous investigations of the electron spectrum in Ge quantum dots [15–17].

At the first step, we considered spin relaxation due to single-phonon direct processes (first-order perturbation theory). Following the approach developed by Roth [18] for the calculation of the spin–lattice relaxation time, we calculate new wave functions of Zeeman sublevels in a magnetic field and then find the transition matrix element between them due to interaction with phonons. We consider processes at low temperatures ($T < 40$ K) and, therefore, take into account only acoustic phonons. The contribution of optical phonons is suppressed by the Boltzmann exponent $\exp(-E_{\mathrm{ph}}/kT)$, where E_{ph} is the optical phonon energy. The operator of interaction with acoustic phonons is described by the equation

$$H^{\varepsilon}_{m'm} = \sum_{ij} D^{ij}_{m'm}\varepsilon_{ij},$$

where $D^{ij}_{m'm}$ is the deformation potential tensor, deformation potential constants D also determine the change in the spectrum upon a homogeneous deformation, and the subscripts m and m' run over the energy bands. The strain tensor ε_{ij} is determined as

$$\varepsilon_{ij} = \sum_{\mathbf{q}} i\left(\frac{\hbar}{2\rho\omega_{\mathbf{q}}}\right)^{1/2}\frac{1}{2}[q_i(e_{\mathbf{q}})_j + q_i(e_{\mathbf{q}})_j] \times (e^{i\mathbf{qr}}a_{\mathbf{q}} - e^{-i\mathbf{qr}}a^{+}_{\mathbf{q}}),$$

where ρ is the density of the medium, $e_{\mathbf{q}}$ is the phonon polarization vector, $\mathbf{q}$ is the phonon wavevector, and $a^{+}_{\mathbf{q}}$ and $a_{\mathbf{q}}$ are phonon creation and annihilation operators. We used the standard form of the electron–phonon interaction operator for the valence-band states [19].

We suggest that a carrier remains in the state with the same spatial configuration and only flips the spin, emitting a phonon. The transition matrix element between the spin up $|\uparrow\rangle$ and spin down $|\downarrow\rangle$ states

$$M_{\mathbf{q}} = \frac{i}{2}\left(\frac{\hbar(n_{\mathbf{q}}+1)}{2\rho\omega_{\mathbf{q}}}\right)^{1/2}\langle\uparrow|D^{ij}|\downarrow\rangle(q_i(e_{\mathbf{q}})_j + q_j(e_{\mathbf{q}})_i), \quad (1)$$

where $n_{\mathbf{q}}$ are phonon occupation numbers and $\omega_{\mathbf{q}}$ is the phonon energy. In Eq. (1), we set the exponential factor $e^{i\mathbf{qr}}$ equal to 1 because we consider only long-wavelength phonons for which the condition $ql \ll 1$ is fulfilled, where l is the characteristic size of the localization region of the hole wave function in the quantum dot.

The transition probability between the spin up $|\uparrow\rangle$ and spin down $|\downarrow\rangle$ states is determined by the Fermi golden rule

$$\Gamma^{(1)} = \sum_{\mathbf{q},\, e_{\mathbf{q}}}\frac{2\pi}{\hbar}|M_{\mathbf{q}}|^2\delta(\hbar sq - \Delta E_z), \quad (2)$$

where ΔE_z is the Zeeman splitting energy, s is the speed of sound, and a linear dispersion law is assumed for phonons. Substituting Eq. (1) for the transition matrix element $M_{\mathbf{q}}$ into Eq. (2), we obtain

$$\Gamma^{(1)} = \frac{2\pi}{\hbar}\frac{\hbar}{2\rho\omega_{\mathbf{q}}}\frac{(n_q+1)}{(2\pi)^3}\langle D^2_\Omega\rangle\int q^4\delta(\hbar sq - \Delta E_z)dq, \quad (3)$$

where the quantity

$$\langle|D_\Omega|^2\rangle = \frac{1}{4\pi}\int\left|\langle\uparrow|D^{ij}|\downarrow\rangle\right|^2(n_i(e_{\mathbf{q}})_j + n_j(e_{\mathbf{q}})_i)^2 d\Omega$$

is obtained by integration over all the directions of the unit vector $\mathbf{n}$.

In order to elucidate the functional dependence of the transition probability on the magnetic field, we simplified Eq. (3) in the limit of low temperatures ($kT \ll \Delta E_z$) to the following:

$$\Gamma^{(1)} = \frac{1}{2\pi}\frac{\langle|D_\Omega|^2\rangle}{\rho\omega_{\mathbf{q}}}\frac{q_0^4}{\hbar s} = \frac{\langle|D_\Omega|^2\rangle}{2\pi}\frac{\Delta E_z^3}{\rho s^5\hbar^4}. \quad (4)$$

Here, $q_0 = \Delta E_z/\hbar s$.

At the first glance, Eq. (4) demonstrates the third order of the power dependence on the magnetic field, but a quadratic dependence is hidden in the matrix element $\langle|D_\Omega|^2\rangle$, because the variation of the wave functions $\delta\psi$ linearly depends on the magnetic field (up to fields $H \sim 10$ T),

$$\psi = \psi_0 + \delta\psi(H).$$

Thus, the dependence of the spin relaxation rate on the magnetic field is described by a power function $\Gamma \sim H^5$. Calculations by Eq. (2) in the magnetic field $H = 1$ T at temperature $T = 4$ K gave the spin relaxation time for the ground state $\tau = 1.4$ ms. The magnetic field is directed along the quantum dot symmetry axis Z ($H \parallel Z$). The value of the g factor obtained in [15] was used for the calculation of the Zeeman splitting ΔE_z.

The temperature dependence of the relaxation time due to single-phonon processes has the form

$$\tau(T) = \mathrm{const}(2n_{\mathbf{q}}+1)^{-1},$$

where $n_{\mathbf{q}}$ is the number of phonons in the vibrational mode with the phonon energy ΔE_z. The value of $n_{\mathbf{q}}$ is proportional to temperature at $kT \gg \Delta E_z$ and vanishes at $T \longrightarrow 0$. Thus, τ tends to a constant at $T \longrightarrow 0$ (because only spontaneous transitions remain) and $\tau \sim T^{-1}$ at sufficiently high temperatures (which corresponds to the predominance of induced transitions).

Consider in more detail how the wave functions change in a magnetic field. The wave functions are calculated in the same way as in [15–17] by the tight-binding method, but the operator of interaction with the magnetic field is added to the Hamiltonian. According to the calculated results, the wave function of the hole ground state in a Ge quantum dot in a zero magnetic field is mainly formed from states of the heavy-hole band (~84%) and has a small admixture of states of the light-hole band (~8%) and the split-off subband (~8%). The angular momentum **J** serves as the effective spin for the hole states. The expansion of the wave functions of the Zeeman sublevels in the basis set $|J, J_z\rangle$ indicates that the state $|\uparrow\rangle$ is mainly formed by states with $J_z = +3/2$ and $J_z = -1/2$. However, the reverse situation occurs for the state $|\downarrow\rangle$, for which the states with $J_z = -3/2$ and $J_z = +1/2$ play the main role. Therefore, the wave functions of the Zeeman sublevels are conveniently represented in the form

$$|\uparrow\rangle = \alpha|+3/2\rangle + \beta|-1/2\rangle,$$
$$|\downarrow\rangle = \alpha|-3/2\rangle + \beta|+1/2\rangle.$$

This expansion indicates that the admixture of states of the light-hole band and the split-off subband with $J_z = 1/2$ has an opposite spin with respect to the main contribution of heavy-hole states. The magnetic field leads to the following changes in the wave functions: for the upper Zeeman sublevel, the contribution of the light-hole states with the opposite spin increases and the contribution of heavy-hole states decreases. For the lower Zeeman sublevel, the situation is the reverse: the contribution of the heavy hole increases. These changes in the ground-state wave functions in the magnetic field are due to an admixture of excited hole states in the Ge quantum dot. The calculated results demonstrate that not all the excited states make an equivalent contribution to the change in the ground-state wave function $\delta\psi(H)$. The contributions of the first and third excited states to $\delta\psi(H)$ exceed the contributions of the other states by an order of magnitude. On the basis of an analysis of the form of wave functions [15], it was found that the symmetry of wave functions is the main factor determining the contributions of excited states. The ground state is formed by the *s*-type component of the heavy hole and has an admixture of the *d*-type component of the light hole. Under the action of the magnetic field, the *s*-type state of the light-hole component of the third excited state is admixed to the *s*-type state of the heavy hole, because the symmetries of these states coincide. On the other hand, the admixture of the *p*-type state of the light-hole component of the first excited state is explained by the fact that this state is mainly localized at the center of the quantum dot, as well as the ground state [15].

We analyzed the contributions of various components of the strain tensor to the matrix element of interaction with phonons. It was found that the ε_{xz} and ε_{yz} components of the strain tensor make the main contribution to spin relaxation. These components of the strain tensor are responsible for the mixing of the states of the heavy-hole band and the light-hole band. This allowed the conclusion that spin relaxation proceeds because of the mutual oscillating variation of the contributions of heavy- and light-hole states, which is induced by the phonon wave. The contribution of the light hole for excited states is larger than that for the ground state; therefore, the variation introduced by the phonon wave is larger. Correspondingly, spin relaxation proceeds more intensely. Actually, calculations for the first excited state give a shorter spin relaxation time of $\tau = 0.37$ ms.

At the next step, two-phonon (Raman) processes were taken into account in the calculation of the spin relaxation time for the ground state. In this case, the relaxation process proceeds through an intermediate excited state. A carrier makes a transition from the ground state to an excited state and in the reverse direction, which is accompanied by the absorption of a phonon with a frequency ω_q and by the emission of a phonon with a frequency $\omega_{q'}$. A spin flip can occur at any of the two steps. The condition that provides the conservation of energy is written in the form $\omega_{q'} - \omega_q = \omega$, where $\hbar\omega = \Delta E_z$. The probability of Raman processes is defined as

$$\Gamma^{(2)} = \sum_{q,\, q',\, e_q,\, e_{q'}} \frac{2\pi}{\hbar} \left| \sum_j \frac{\langle f|H_\varepsilon(\omega_{q'})|j\rangle \langle j|H_\varepsilon(\omega_q)|i\rangle}{E_i - E_j \mp \hbar\omega_q} \right|^2 \times \delta(E_f - E_i \pm \hbar\omega_q \mp \hbar\omega_{q'});$$

here, the operator H_ε describes electron–phonon interaction, j is the number of the excited state, and the summation is over the wave vectors and their polarizations.

When the Raman processes are taken into account, the temperature dependence becomes more important. While the spin relaxation time for the ground state of a hole in a Ge quantum dot equals 0.3 ms (magnetic field $H = 1$ T) at the temperature $T = 4$ K, it drops to 0.65 μs at $T = 10$ K. With a further increase in temperature, the spin relaxation time continues to decrease and makes up several nanoseconds at 20 K. The temperature dependence of the relaxation rate with regard to two-phonon processes is described by the T^7 law (see figure), while relaxation due to single-phonon processes weakly depends on temperature. Analysis of transition probabilities shows that the third and twelfth excited states play the main part in Raman processes; these states are intermediate states in two-step relaxation pro-

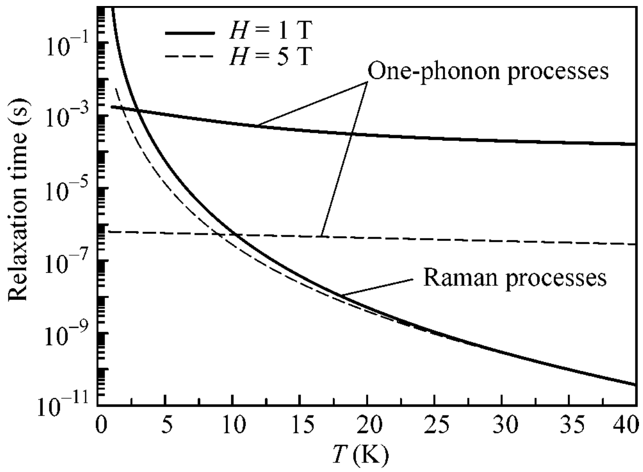

Temperature dependence of the spin relaxation time due to interaction with phonons for the hole ground state in a Ge quantum dot (the height $h = 1.5$ nm, the base size $l = 15$ nm). The magnetic field is $H \parallel Z$, where Z is the growth direction of the Ge quantum dot.

cesses. It should also be noted that direct processes become determining at temperatures below a certain critical temperature. This critical temperature for the field $H = 1$ T equals 3 K.

In conclusion, we formulate the range of applicability of the obtained results. The first restriction stems from the condition $\Delta E_z \ll E_0 - E_n$; that is, the Zeeman splitting must be smaller than the distance between the quantization levels. This condition is fulfilled for magnetic fields $H \sim 10$ T. The second restriction follows from the condition $\lambda \gg l$, where l is the characteristic size of the localization region of the hole wave function and λ is the phonon wavelength. This corresponds to the temperature restriction $T < 70$ K, because the localization region $l \approx 3$ nm according to our calculations [11]. The latter restriction is also connected with the requirement that the higher orders of the perturbation theory are small. We considered the first two orders of the perturbation theory and obtained the corresponding relaxation rates $\Gamma^{(1)}$ and $\Gamma^{(2)}$. From dimensionality considerations, the following relation can be written for the relaxation rate in the next order of the perturbation theory $\Gamma^{(3)}$:

$$\frac{\Gamma^{(3)}}{\Gamma^{(2)}} \sim \left(\frac{|M^{(3)}|}{|M^{(2)}|}\right)^2 \frac{(kT)^4}{\rho s^5 \hbar^3}.$$

From the condition that this ratio is small, we find the temperature restriction $T < 60$ K.

Thus, the given approach to the calculation of the spin relaxation rate is valid for temperatures $T < 60$ K and magnetic fields up to $H \sim 10$ T. The long relaxation time due to direct processes obtained in this work ($\tau \sim 1$ ms) is the direct consequence of the fact that the character of the hole ground state in the quantum dot is close to the state of the heavy hole. The possibility of relaxation depends on the degree of admixture of the light-hole states, and, because this degree is small, spin relaxation is suppressed.

This work was supported by the Russian Foundation for Basic Research, project no. 05-02-16285, and by INTAS, grant no. 2001-0615.

REFERENCES

1. G. Feher, Phys. Rev. **114**, 1219 (1959); G. Feher and E. Gere, Phys. Rev. **114**, 1245 (1959); D. K. Wilson and G. Feher, Phys. Rev. **124**, 1068 (1961).
2. M. Chiba and A. Hirai, J. Phys. Soc. Jpn. **33**, 730 (1972).
3. R. Vrijen, E. Yablonovitch, K. Wang, *et al.*, Phys. Rev. A **62**, 012 306 (2000).
4. A. I. Yakimov, A. V. Dvurechenskii, A. I. Nikiforov, and O. P. Pcheljakov, Thin Solid Films **336**, 332 (1998).
5. N. S. Averkiev, L. E. Golub, and M. Willander, Fiz. Tekh. Poluprovodn. (St. Petersburg) **36**, 97 (2002) [Semiconductors **36**, 91 (2002)].
6. N. S. Averkiev and L. E. Golub, Phys. Rev. B **60**, 15582 (1999).
7. D. Loss and D. DiVicenzo, Phys. Rev. A **57**, 120 (1998).
8. P. Recher, E. V. Sukhorukov, and D. Loss, Phys. Rev. Lett. **85**, 1962 (2000).
9. I. A. Merkulov, Al. L. Efros, and M. Rosen, Phys. Rev. B **65**, 205 309 (2002).
10. A. V. Khaetskii, D. Loss, and L. Glazman, Phys. Rev. Lett. **88**, 186 802 (2002).
11. A. F. Zinovieva, A. V. Nenashev, and A. V. Dvurechenskii, Phys. Rev. B **71**, 033 310 (2005).
12. P.-F. Braun, X. Marie, L. Lombez, *et al.*, in *Proceedings of 13th International Symposium on Nanostructures: Physics and Technology*, Ed. by Zh. Alferov and L. Esaki (Ioffe Physicotechnical Inst., St. Petersburg, 2005), p. 45.
13. A. Losche, *Kerninduktion* (Wissenschaften, Berlin, 1957; Inostrannaya Literatura, Moscow, 1963).
14. A. I. Yakimov, A. V. Dvurechenskii, Yu. Yu. Proskuryakov, *et al.*, Appl. Phys. Lett. **75**, 1413 (1999).
15. A. V. Nenashev, A. V. Dvurechenskii, and A. F. Zinovieva, Phys. Rev. B **67**, 205 301 (2003).
16. A. V. Nenashev, A. V. Dvurechenskiĭ, and A. F. Zinov'eva, Zh. Éksp. Teor. Fiz. **123**, 362 (2003) [JETP **96**, 321 (2003)].
17. A. V. Dvurechenskii, A. V. Nenashev, and A. I. Yakimov, Nanotechnology **13**, 75 (2002).
18. L. M. Roth, Phys. Rev. **118**, 1534 (1960).
19. G. L. Bir and G. E. Pikus, *Symmetry and Strain-induced Effects in Semiconductors* (Nauka, Moscow, 1972; Wiley, New York, 1974), p. 393.

Translated by A. Bagatur'yants

JETP Letters, Vol. 82, No. 5, 2005, pp. 306–310. Translated from Pis'ma v Zhurnal Éksperimental'noĭ i Teoreticheskoĭ Fiziki, Vol. 82, No. 5, 2005, pp. 341–345.
Original Russian Text Copyright © 2005 by Gulyaev, Zil'berman, Épshteĭn.

Switching Effect in Ferromagnetic Metallic Junctions

Yu. V. Gulyaev, P. E. Zil'berman, and É. M. Épshteĭn
Institute of Radio Engineering and Electronics, Russian Academy of Sciences, Fryazino, Moscow region, 141190 Russia
e-mail: zil@ms.ire.rssi.ru

Received July 15, 2005

Mechanisms are determined for homogeneous current-induced switching in ferromagnetic metallic junctions of the spin-valve type. The spin flux is perpendicular to the junction surface and is directed from the pinned layer to the free one. The switching is due to the joint action of two mechanisms: (i) current-induced surface torque and (ii) current-induced injection of nonequilibrium longitudinal spins into the free-layer bulk. Both mechanisms lead to the instability and reorientation of magnetization; however, only the injection mechanism can stabilize the switching. *© 2005 Pleiades Publishing, Inc.*

PACS numbers: 72.25.–b

Magnetic junctions represent an interesting object for investigation and subsequent applications, because current-induced magnetic-moment instability in them was recently predicted [1, 2] and manifestations of this instability—resistance jumps [3] and microwave emission [4]—have been observed experimentally. It has been found that the torque mechanism proposed in [1, 2] is not the only one essential mechanism leading to instability. Another mechanism associated with longitudinal-spin injection by current into the bulk of the ferromagnetic layer was proposed and studied in [5–8]. In the recent work [9] (and in the preprint [10]), a theory has been constructed in which the joint action of both instability mechanisms mentioned above was described.

However, the question remains open as to what properties the new magnetic state arising from the development of this instability should possess. Meanwhile, in the end, this question is most essential, because it is the resulting state that is experimentally observed for the present. However, the possibilities of applications depend in many respects on the properties that will be exhibited by this state.

Since the first works [1, 2], it has been considered that the instability caused by only the torque action leads to magnetic switching. However, this has not been proved and is still only a suggestion. Nevertheless, the fact of switching itself has been confirmed experimentally. In this work, we demonstrate for the first time that the torque action by itself cannot provide the stability of switching. To explain this effect, the effect of longitudinal-spin injection by current must be taken into account in the theory.

1. Model and calculations. In the calculation, the junction is considered as a planar layered structure perpendicular to axis x. Two ferromagnetic metallic layers are separated at $x = 0$ by a thin nonmagnetic layer that does not preclude conductivity and does not disturb the spin polarization of the current. At $x < 0$, ferromagnetic layer **1** is located with fully pinned magnetization vectors of the lattice $\mathbf{M}_1$ and the mobile electrons $\mathbf{m}_1$ ("injector"). At $0 < x < L$, ferromagnetic layer **2** is located with free magnetization vectors $\mathbf{M}$ and $\mathbf{m}$, which can vary as functions of the external magnetic field $\mathbf{H}$ and the current density vector $\mathbf{j}$. The electron flux flows in the direction from the injector to layer **2**. This direction is further considered positive, so that $j/e > 0$ (e is the electron charge). At $x > L$, there is a well conducting nonmagnetic layer, which is necessary for the closure of the electric circuit. It is considered that the external circuit provides the regime of the specified current, so that the processes under consideration can change only the voltage drop V across the junction.

According to the main idea of the works [1, 2], an important part is played by an extremely narrow layer near the interface $0 < x < \lambda_F \leq 1$ nm. Inside this layer, which we will further call the Slonczewski–Berger (SB) layer, the directional deflection of vector $\mathbf{M}$ from the fixed vector $\mathbf{M}_1$ by a certain angle χ leads to a precession of vector $\mathbf{m}$ around $\mathbf{M}$, that is, to the appearance of the transversal $\mathbf{m}_\perp$ and longitudinal $\mathbf{m}_\parallel$ (relative to $\mathbf{M}$) components. Component $\mathbf{m}_\perp$ decays inside the SB layer because of the statistical scatter of electrons by velocities. Parameter λ_F determines the thickness of the SB layer and, in essence, is close to the quantum electron wavelength at the Fermi surface. Owing to the decay of component $\mathbf{m}_\perp$, the transversal part of the electron spin flux vanishes. However, the total transversal spin flux must be conserved and, therefore, its vanished part must be transferred from the mobile electrons to the magnetic lattice. This is the torque appearance mechanism.

The spin injection mechanism considered in [5–8], as distinct from torque, is associated with the longitudinal $\mathbf{m}_\parallel$ rather than transversal component. The longitudinal-spin flux penetrates deep into layer **2** at the diffusion length $l \sim 10–100$ nm. It creates a current-dependent effective *sd*-exchange field $\mathbf{H}_{sd}$, which also affects the magnetic lattice.

Further, we will use the theory of the joint action of the above effects that was developed in [9]. The theory is based on the solution of the macroscopic Landau–Lifshitz–Gilbert (LLG) equations for vector **M** and the continuity equation for vector **m**. According to this theory, the spin flux in pinned layer **1** arises only because of the occurrence of an electric current and can be presented in the form

$$\mathbf{J}_1 = \frac{\mu_B}{e} Q_1 j \hat{\mathbf{M}}_1, \qquad (1)$$

where parameter $0 < Q_1 < 1$ is the degree of current spin polarization, $\hat{\mathbf{M}}_1 = \mathbf{M}_1/M_1$ is the unit vector, and μ_B is the Bohr magneton. The flux given by Eq. (1) contains both the longitudinal $\mathbf{J}_{1\parallel}$ and transversal $\mathbf{J}_{1\perp}$ components with respect to vector $\hat{\mathbf{M}} = \mathbf{M}/M$ taken at the boundary $x \longrightarrow +0$. Namely,

$$\begin{aligned} \mathbf{J}_{1\parallel} &= \frac{\mu_B}{e} Q_1 j (\hat{\mathbf{M}}_1 \hat{\mathbf{M}}(+0)) \hat{\mathbf{M}}(+0), \\ \mathbf{J}_{1\perp} &= \frac{\mu_B}{e} Q_1 j [\hat{\mathbf{M}}(+0), [\hat{\mathbf{M}}_1, \hat{\mathbf{M}}(+0)]]. \end{aligned} \qquad (2)$$

The longitudinal component $\mathbf{J}_{1\parallel}$ continuously passes into layer **2** and, at $x > \lambda_F$, equals

$$\mathbf{J}(x) = \left(\frac{\mu_B}{e} Q j - \tilde{D} \frac{\partial m(x)}{\partial x}\right) \hat{\mathbf{M}}(x), \qquad (3)$$

where parameter Q is similar in its sense to Q_1 but is taken for layer **2**. Parameter $\tilde{D}$ is the spin diffusion coefficient in layer **2**. The designation $\mathbf{m}_\parallel = m \cdot \hat{\mathbf{M}}$ is introduced for the longitudinal magnetization. The characteristic length over which the quantity m varies is the spin diffusion length l, and the characteristic length for the quantity $\hat{\mathbf{M}}$ is the inverse wave number of spin waves in the lattice q^{-1}. As in [9], we assume further that λ_F is the least of all the characteristic lengths in the problem and, in particular, $\lambda_F \ll l$, $q\lambda_F \ll 1$, which corresponds to the real situation. Then, the equation

$$\mathbf{J}_{1\parallel} = \mathbf{J}(+0) \qquad (4)$$

holds. This equation can be considered as one of the boundary conditions in the determination of the magnetization $m(x)$. Another boundary condition is the continuity of the spin flux at the boundary $x = L$. Flux $\mathbf{J}_3$ in layer **3** coincides with that given by Eq. (3) if the substitutions $Q \longrightarrow Q_3 = 0$, $\tilde{D} \longrightarrow \tilde{D}_3$, and $m \longrightarrow m_3$ are made. Then the continuity condition is written as

$$\mathbf{J}(L-0) = \mathbf{J}_3(L+0). \qquad (5)$$

Moreover, the difference of the chemical potentials of the spin subbands must also be continuous at $x = L$ [9].

The continuity equation for the magnetization m and the above boundary conditions describe the process of nonequilibrium longitudinal spin injection by current. The solution of this problem in [9] yielded the expression

$$\begin{aligned} m(x) &= m_{\text{eq}} + \frac{j}{j_D} \frac{\mu_B n}{\sinh\lambda + \nu\cosh\lambda} \\ &\times \{ Q\cosh\xi + [Q_1(\hat{\mathbf{M}}_1 \hat{\mathbf{M}}(+0)) - Q] \\ &\times [\cosh(\lambda - \xi) + \nu\sinh(\lambda - \xi)] \}, \end{aligned} \qquad (6)$$

where m_{eq} is the equilibrium magnetization value at $j = 0$. The current-induced nonequilibrium term in Eq. (6) contains the following designations: n is the concentration of mobile electrons, $\lambda = L/l$, $\xi = x/l$, $j_D = enl/\tau$, τ is the spin equilibration time, and $\nu \sim 1$ is the parameter characterizing the matching of spin fluxes at the boundary of layers **2** and **3**. At typical values of parameters $n \sim 10^{22}$ cm^{-3}, $l \sim 3 \times 10^{-6}$ cm, $\tau \sim 3 \times 10^{-13}$ s, the estimate $j_D \sim 1.6 \times 10^{10}$ A/cm^2 is obtained. The currents of interest are on the order of the instability thresholds, that is, $j \sim j_{\text{th}} \le 3 \times 10^7$ A/cm^2 [3, 4]. Thus, $j/j_D \sim 2 \times 10^{-3} \ll 1$, so that the conditions of weak spin injection are fulfilled.

Note in addition that, in the derivation of Eq. (6) in [9], it was taken into account that the precession of the lattice outside the SB layer occurs at frequencies ω of the microwave range for which $\omega\tau \ll 1$. Hence, electrons react to the instant magnetization of the lattice, which explains why the quantity m in Eq. (6) depends instantaneously on the nonequilibrium vector $\hat{\mathbf{M}}$.

Now, it is necessary to consider the passage of the transversal spin flux across the layer interface. Inside layer **2**, the LLG equation is valid, and this equation can be presented according to [9] in the form

$$\begin{aligned} &\frac{\partial \mathbf{M}}{\partial t} + \gamma A \left[\mathbf{M}, \frac{\partial^2 \mathbf{M}}{\partial x^2}\right] + \gamma [\mathbf{M}, \mathbf{H}_{sd}] \\ &+ \gamma [\mathbf{M}, \mathbf{H}'] - \kappa \left[\mathbf{M}, \frac{\partial \mathbf{M}}{\partial t}\right] = 0, \end{aligned} \qquad (7)$$

where $A \sim 10^{-12}$ cm^2 is the intralattice exchange constant, $0 < \kappa \ll 1$ characterizes dissipation, and γ is the gyromagnetic ratio. The field $\mathbf{H}' = \mathbf{H} + \mathbf{H}_a + \mathbf{H}_d$ includes the external field **H**, the anisotropy field $\mathbf{H}_a$, and the demagnetization field $\mathbf{H}_d$. The effective *sd*-exchange field in this problem must be presented in the functional derivative form [11]

$$\mathbf{H}_{sd}(x) = -\frac{\delta U_{sd}}{\delta \mathbf{M}(x)}, \qquad (8)$$

where the *sd*-exchange energy equals

$$U_{sd} = -\alpha\int_0^L \mathbf{m}(x', t)\mathbf{M}(x', t)dx', \tag{9}$$

and α is the dimensionless *sd*-exchange constant (for example, $\alpha \sim 2 \times 10^4$). We emphasize that, when substituting Eq. (9) into Eq. (8) and computing the derivative, it is essential to take into account the functional dependence $m(\mathbf{M})$, which, in this case, is given explicitly by Eq. (6). Then, the direct calculation gives

$$\begin{aligned}\mathbf{H}_{sd}(x) &= \alpha\mu_B nQ_1 l\left(\frac{j}{j_D}\right)\\ &\times\left(1-\frac{\nu}{\sinh\lambda+\nu\cosh\lambda}\right)\hat{\mathbf{M}}_1\delta(x-0),\end{aligned} \tag{10}$$

where only the nonequilibrium ($\sim j$) part of the effective field is retained. Its equilibrium part is collinear with **M** and therefore makes no contribution to Eq. (7). The field $\mathbf{H}_{sd}$ describes the bulk spin injection effect and, therefore, depends on the bulk parameters of layer **2**: n, ν, L, and l. However, the δ function in the right-hand side of Eq. (10) shows that this field is applied to the boundary surface $x \longrightarrow +0$. Therefore, it can be taken into account as a certain addition to the continuity condition for the transversal spin flux across this boundary.

Consider the second and the third terms on the left-hand side of Eq. (7). After the substitution of Eq. (10) and direct transformations (see Appendix I in [9]), these terms take the form

$$\gamma A\left[\mathbf{M}, \frac{\partial^2\mathbf{M}}{\partial x^2}\right] + \gamma[\mathbf{M}, \mathbf{H}_{sd}] = \frac{\partial(\mathbf{J}_M + \mathbf{J}_{sd})}{\partial x}, \tag{11}$$

where the quantities

$$\mathbf{J}_M(x) = a\left[\hat{\mathbf{M}}, \frac{\partial\mathbf{M}}{\partial x}\right] \tag{12}$$

and

$$\begin{aligned}\mathbf{J}_{sd}(x) &= \gamma\alpha\mu_B nQ_1 l\frac{j}{j_D}\left(1-\frac{\nu}{\sinh\lambda+\nu\cosh\lambda}\right)\\ &\times[\mathbf{M}(+0), \hat{\mathbf{M}}_1]\theta(x-0)\end{aligned} \tag{13}$$

are treated as lattice magnetization fluxes due to intralattice exchange and *sd* exchange, respectively. Here, $a = \gamma MA$, $\theta(x-\varepsilon) = 1$ at $x > \varepsilon$, and $\theta(x-\varepsilon) = 0$ at $x < \varepsilon$. Fluxes given by Eqs. (12) and (13) are transversal with respect to vector **M**. Owing to the smallness of λ_F, the two latter terms in Eq. (7) can be neglected inside the SB layer. Then, the continuity condition for the transversal flux at the boundary $x = 0$ is reduced to the equation

$$\mathbf{J}_{1\perp} = \mathbf{J}_M(\lambda_F) + \mathbf{J}_{sd}(\lambda_F). \tag{14}$$

This equation can be regarded as one of the boundary conditions when the LLG equation is solved in the region $\lambda_F < x < L$ of layer **2**. Another condition arises at the boundary $x = L$ and can be written as

$$\mathbf{J}_M(L-0) = 0, \tag{15}$$

because flux $\mathbf{J}_{sd}(x)$ according to Eq. (13) is constant at $x = L$ and falls out of the continuity condition given by Eq. (15).

2. Stability of the initial static state. The simplest initial static state is accomplished with collinear vectors $\bar{\mathbf{M}}_1$, $\bar{\mathbf{M}}$, $\mathbf{H}_a$, and **H** lying in the junction plane. In this case, Eq. (7) is fulfilled by a homogeneous magnetization distribution over the sample. There are two possibilities: either static vectors $\bar{\mathbf{M}}_1$ and $\bar{\mathbf{M}}$ are parallel (P state) or they are antiparallel (AP state). Consider then the most important case when the AP state is accomplished in the absence of current ($j = 0$), namely, $\hat{\mathbf{M}}_1 = -\hat{\mathbf{z}}$, $\hat{\mathbf{M}} = \hat{\mathbf{z}}$, and $\mathbf{H} = \hat{\mathbf{z}}$, where $\hat{\mathbf{x}}$, $\hat{\mathbf{y}}$, and $\hat{\mathbf{z}}$ designate unit vectors of coordinate axes. Upon switching on the current, fluctuations can become unstable. The instability threshold was calculated in [9]; however, in that case, the singular (containing δ function) *sd*-exchange field [10] was taken into account in the equation of motion itself (Eq. (7)) rather than in the flux $\mathbf{J}_{sd}(x)$ and in the boundary condition (Eq. (14). In the new approach proposed in this work, the singularity is eliminated from the equations of motion. This significantly simplifies the solution of Eq. (7) and allows one to find not only the threshold of instability but also nonlinear solutions arising from the development of this instability.

Fluctuations $\Delta\hat{\mathbf{M}}$ are introduced by the equation $\hat{\mathbf{M}} = \hat{\mathbf{z}} + \Delta\hat{\mathbf{M}}$. Equation (7) linearized with respect to fluctuations take the form (taking into account that $\mathbf{H}_d = -4\pi M\Delta\hat{M}_x\hat{\mathbf{x}}$)

$$\begin{aligned}&\frac{\partial^2\Delta\hat{M}_x}{\partial x^2} - \frac{(\Omega_x - i\kappa\omega)}{a}\Delta\hat{M}_x - \frac{i\omega}{a}\Delta\hat{M}_y = 0,\\ &\frac{\partial^2\Delta\hat{M}_y}{\partial x^2} - \frac{(\Omega_y - i\kappa\omega)}{a}\Delta\hat{M}_y + \frac{i\omega}{a}\Delta\hat{M}_x = 0,\end{aligned} \tag{16}$$

where $\Omega_x = \gamma(H + H_a + 4\pi M)$, $\Omega_y = \gamma(H + H_a)$, and $\Omega_x > \Omega_y$. After linearization, the boundary conditions (Eqs. (14) and (15)) are reduced to the equations

$$\begin{aligned}\frac{\partial\Delta\hat{M}_x}{\partial x} &= k\Delta\hat{M}_y - p\Delta\hat{M}_x,\\ \frac{\partial\Delta\hat{M}_y}{\partial x} &= -k\Delta\hat{M}_x - p\Delta\hat{M}_y\end{aligned} \tag{17}$$

at $x = 0$ and to the equations

$$\frac{\partial \Delta \hat{M}_x}{\partial x} = 0, \quad \frac{\partial \Delta \hat{M}_y}{\partial x} = 0 \qquad (18)$$

at $x = L$. Solving the linear problem given by Eqs. (16)–(18) leads to the dispersion relation for fluctuations

$$q\tan qL = -p \pm ik, \qquad (19)$$

in which the square of the wave number equals

$$q^2 = -\frac{1}{2a}\left[\Omega_x + \Omega_y - 2i\kappa\omega \pm \sqrt{(\Omega_x - \Omega_y)^2 + 4\omega^2}\right], \qquad (20)$$

and the parameters

$$p = \frac{a\mu_B Q_1 \tau j}{eAM}\left(1 - \frac{\nu}{\sinh\lambda + \nu\cosh\lambda}\right), \qquad k = \frac{\mu_B Q_1 j}{e\gamma M^2 A} \qquad (21)$$

describe the spin injection (p) and torque (k) effects. Dispersion equation (19) allows the instability condition $\mathrm{Im}\,\omega > 0$ to be obtained. Consider sufficiently small thicknesses of layer **2** obeying the inequality $|p \pm ik|L \ll 1$. This inequality is fulfilled, for example, at $L \sim 2$–7 nm. At such thicknesses, the instability condition takes the form

$$\kappa^2\left(\Omega_x - \frac{ap}{L}\right)\left(\Omega_y - \frac{ap}{L}\right) - \left(\frac{ak}{L}\right)^2 < 0. \qquad (22)$$

Because, according to Eq. (21), parameters p and k are proportional to current j, we obtain from Eq. (22) for the instability threshold

$$\frac{j_{th}}{j_\perp} = \eta\frac{(f^{-1} + f) - \sqrt{(f^{-1} - f)^2 + 4\eta^2}}{2(1 - \eta^2)}, \qquad (23)$$

where $f = \sqrt{\Omega_y/\Omega_x} < 1$, $j_\perp = \kappa eML\sqrt{\Omega_x\Omega_y}/\mu_B Q_1$, and an important parameter

$$\eta = \left[\gamma\alpha M\tau\kappa\left(1 - \frac{\nu}{\sinh\lambda + \nu\cosh\lambda}\right)\right]^{-1}, \qquad (24)$$

is introduced. This parameter characterizes the relative role of parameters p and k, that is, spin injection and torque. At $\eta \gg 1$, torque dominates and it follows from Eq. (23) that $j_{\rm th} \longrightarrow j_\perp$. At $\eta \ll 1$, spin injection dominates. In this case, $j_{\rm th} \longrightarrow \eta f j_\perp \ll j_\perp$; that is, the instability threshold becomes significantly lower. A numerical estimation gives $j_\perp \sim 3 \times 10^7$ A/cm^2, which corresponds to experimental data (see [3, 4] and others).

3. Switching effect. As was already mentioned, junctions of small thickness are considered for which $|p \pm ik|L \ll 1$ and, in addition, $L \ll l$, $qL \ll 1$. Then the state arising from the development of instability must remain spatially homogeneous. There exist only two such states: P and AP. Since the AP state was selected as the initial state, the development of instability can give rise only to the P state. Switching will take place only in the case when the P state turns out to be stable.

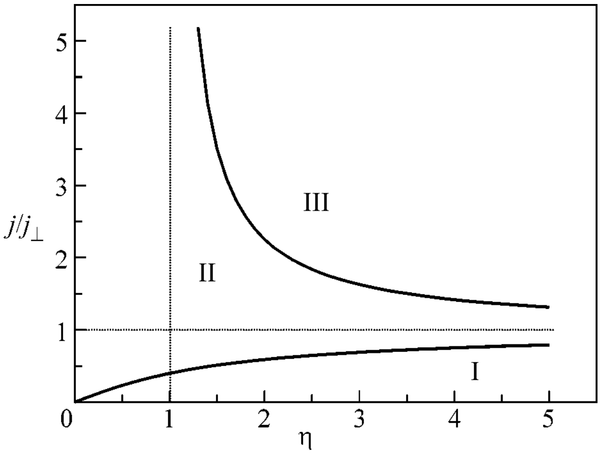

Stability–instability regions. The boundaries of regions I and II are constructed by Eqs. (23) and (25), respectively: (I) P and AP are stable, (II) P is stable and AP is unstable, and (III) P and AP are unstable.

The stability of the P state can be investigated in the same way as in section 2, but the substitution $\mathbf{M}_1 \longrightarrow -\mathbf{M}_1$ should be made in Eqs. (2) and (13). In the condition (22), this will lead to the substitution $p \longrightarrow -p$ and $k \longrightarrow -k$. At a positive current ($j/e > 0$), which is the only case that we consider, spin injection will always make a positive contribution to the left-hand side of Eq. (22), that is, will suppress instability. However, instability still could occur because of the action of torque. The threshold of such instability is obtained from the condition given by Eq. (22) with the above substitutions and is given by the equation

$$\frac{j_{\rm th}}{j_\perp} = \eta\frac{(f^{-1} + f) + \sqrt{(f^{-1} - f)^2 + 4\eta^2}}{2(\eta^2 - 1)}. \qquad (25)$$

A schematic diagram constructed by Eqs. (23) and (25) is shown in the figure. This diagram shows the regions of stability and instability in the plane (j, η). It is seen that the new P state is stable only at not-too-high values of parameter η, when the injection of nonequilibrium transversal spins by current. Contrary to the prevailing opinion, the torque mechanism alone does not provide stable switching. In fact, the torque arises from the decay of the precession in the SB layer. This decay always exists regardless of whether vector **M** is oriented in this layer parallel or antiparallel with respect to $\mathbf{M}_1$. At the same time, the parallel orientation of the above vectors corresponds to a minimum of the *sd*-exchange energy and, therefore, is the most stable orientation in the effective field $\mathbf{H}_{sd}$. It should be noted that, if the current increases to become considerably higher than the threshold value $j_{\rm th}$, both homogeneous states, P and AP, can become unstable because of the torque effect. In this case, evidently, a new time-dependent state of the turbulence type can arise.

We are grateful to A.I. Krikunov and A.V. Medved' for interesting discussions. This work was supported by the Russian Foundation for Basic Research, project nos. 03-02-17540 and 04-02-08248.

REFERENCES

1. J. C. Slonczewski, J. Magn. Magn. Mater. **159**, L1 (1996).
2. L. Berger, Phys. Rev. B **54**, 9353 (1996).
3. J. A. Katine, F. J. Albert, R. A. Buhrman, *et al.*, Phys. Rev. Lett. **84**, 3149 (2000).
4. M. Tsoi, A. G. M. Jansen, J. Bass, *et al.*, Phys. Rev. Lett. **80**, 4281 (1998); Phys. Rev. Lett. **81**, 493(E) (1998).
5. C. Heide, P. E. Zilberman, and R. J. Elliott, Phys. Rev. B **63**, 064 424 (2001).
6. Yu. V. Gulyaev, P. E. Zil'berman, É. M. Épshteĭn, and R. J. Elliott, Pis'ma Zh. Éksp. Teor. Fiz. **76**, 189 (2002) [JETP Lett. **76**, 155 (2002)].
7. R. J. Elliott, E. M. Epshtein, Yu. V. Gulyaev, and P. E. Zilberman, J. Magn. Magn. Mater. **271**, 88 (2004).
8. Yu. V. Gulyaev, P. E. Zil'berman, É. M. Épshteĭn, and R. J. Elliott, Pis'ma Zh. Éksp. Teor. Fiz. **79**, 507 (2004) [JETP Lett. **79**, 402 (2004)].
9. Yu. V. Gulyaev, P. E. Zil'berman, É. M. Épshteĭn, and R. J. Elliott, Zh. Éksp. Teor. Fiz. **127**, 1138 (2005) [JETP **100**, 1005 (2005)].
10. R. J. Elliott, E. M. Epshtein, Yu. V. Gulyaev, and P. E. Zilberman, cond-mat/0412523.
11. A. I. Akhiezer, V. G. Bar'yakhtar, and S. V. Peletminskiĭ, *Spin Waves* (Nauka, Moscow, 1967; North-Holland, Amsterdam, 1968).

Translated by A. Bagatur'yants

JETP Letters, Vol. 82, No. 5, 2005, pp. 311–315. Translated from Pis'ma v Zhurnal Éksperimental'noĭ i Teoreticheskoĭ Fiziki, Vol. 82, No. 5, 2005, pp. 346–351.
Original Russian Text Copyright © 2005 by Bugrij, Iorgov, Shadura.

Alternative Method of Calculating the Eigenvalues of the Transfer Matrix of the τ_2 Model for $N = 2$

A. I. Bugrij, N. Z. Iorgov, and V. N. Shadura
Bogolyubov Institute for Theoretical Physics, National Academy of Sciences of Ukraine, Kiev, 03143 Ukraine
e-mail: abugrij@bitp.kiev.ua, iorgov@bitp.kiev.ua, shadura@bitp.kiev.ua

Received July 14, 2005

It has been shown that the τ_2 (Baxter–Bazhanov–Stroganov) model for $N = 2$ with arbitrary parameters is a particular case of the generalized Ising model. The model satisfies the free-fermion condition, which enables one to solve it by the method of the auxiliary Grassmann field. Explicit expressions have been derived for the partition function on a finite-size lattice and eigenvalues of the transfer matrix. In this approach, in contrast to the functional relation method, there is no problem with the multiplicities of the eigenvalues of transfer matrix. *© 2005 Pleiades Publishing, Inc.*

PACS numbers: 05.50.+q, 75.10.Hk

The τ_2 model is one of a few exactly solvable models in which pseudospin variables take N values. This model was found by Baxter [1], who noted that the inverse matrix to the column–column transfer matrix of the superintegrable chiral Potts model specifies a new integrable model and called it the "Inverse SOS" model. More recently, this model in the L matrix formulation appeared in work [2] by Bazhanov and Stroganov as an auxiliary model that enables one to find a connection between six-vertex model and chiral Potts model. The connection between these three models makes it possible to formulate a system of functional relations [2, 3] for the transfer matrices of these models. The solution of this system of functional relations is one of the basic methods of calculating the free energy of the chiral Potts model. Recently, using the connection of the τ_2 model with the chiral Potts model and certain assumptions concerning analytic properties, the formula for the order parameter in the chiral Potts model was verified [4]. In what follows, we use the term Baxter–Bazhanov–Stroganov (BBS) model rather than the term τ_2 model.

In this work, it has been shown that the BBS model for $N = 2$ is a particular case of the generalized Ising model. The model satisfies the condition of "free fermions," which enables one to solve it by the method of the auxiliary Grassmann field [5]. Simple calculations provide explicit expressions for the partition function on a finite-size lattice and the eigenvalues of the transfer matrix. A similar expression for eigenvalues was obtained by the functional relation method in [6]. A disadvantage of this method is that it provides a set of solutions that contains all eigenvalues of the transfer matrix, but additional analysis is necessary in order to determine which solutions are really eigenvalues (and their multiplicities). The method used in this work does not have this disadvantage: it provides a set of eigenvalues unambiguously.

The BBS model is considered [7] on a rectangular lattice at whose sites there are the pseudospin variables b_r (r is the number of a site) taking N values $0, 1, \ldots, N-1$, where $N \geq 2$. It is convenient to specify b_r values by all integers, identifying two values whose difference is a multiple of N. Not all values are allowable: values at the rth and sth sites neighboring in the vertical (r is higher than s) must satisfy the additional condition

$$b_r = b_s \text{ or } b_s + 1 \mod N. \tag{1}$$

The model includes the parameters (complex in general) α, t, x, y, μ, x', y', and μ'. Each plaquette has the Boltzmann weight

$$W_\tau(b^1, b^2, b^3, b^4) = \alpha \sum_{m=0}^{1} \omega^{m(b^4 - b^2)} (-\omega t)^{b^1 - b^4 - m}$$
$$\times F(b^1 - b^4, m) F'(b^2 - b^3, m),$$

where $\omega = e^{2\pi i/N}$,

$$F(0, 0) = 1, \quad F(0, 1) = -\omega t/y,$$
$$F(1, 0) = \mu/y, \quad F(1, 1) = -\omega x\mu/y,$$

and expressions for $F'(l, m)$ are obtained from the expressions for $F(l, m)$ by changing x, y, and μ to x', y', and μ', respectively. Note that the BBS model is $\mathbb{Z}_N$-symmetric; i.e., the addition of the same number to b_r values at all lattice sites does not change the Boltzmann weights of plaquettes.

For $N = 2$, we reformulate the model as follows. Ising spins σ_r, which take the values 1 and –1 instead of 0 and 1 for b_r, respectively, are located at lattice sites. Condition (1) is automatically satisfied for $N = 2$. The

0021-3640/05/8205-0311$26.00 © 2005 Pleiades Publishing, Inc.

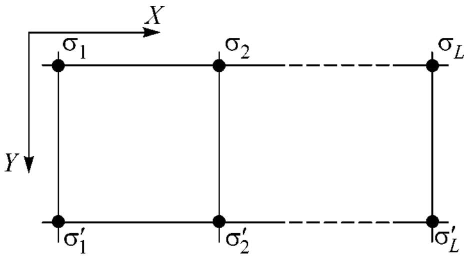

Fig. 1.

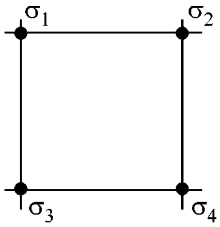

Fig. 2.

Boltzmann weight associated with a plaquette has the form

$$w_\tau(\sigma^1, \sigma^2; \sigma^4, \sigma^3) = \alpha \sum_{m=0}^{1} (-1)^{m(b^4 - b^2)} t^{|b^1 - b^4| - m} \times F(|b^1 - b^4|, m) F'(|b^2 - b^3|, m), \quad (2)$$

where $b^k = (1 - \sigma^k)/2$, for $k = 1, 2, 3$, and 4, and

$$F(0, 0) = 1, \quad F(0, 1) = t/y,$$
$$F(1, 0) = \mu/y, \quad F(1, 1) = x\mu/y.$$

The functions F' are defined similarly.

The transfer matrix of the generalized Ising model in the absence of the external field has the form (numbering of lattice sites is shown Fig. 1)

$$T_{[\sigma, \sigma']} = \prod_{x=1}^{L} w(\sigma_x, \sigma_{x+1}; \sigma'_x, \sigma'_{x+1}). \quad (3)$$

Its dimension is equal to $2^L \times 2^L$, where L is the number of lattice sites along the horizontal axis. In Eq. (3), σ_x is the Ising pseudospin. The boundary conditions are periodic ($\sigma_{L+1} = \sigma_1$). The most general form of the $\mathbb{Z}_2$ symmetric function of the four spin variables are specified by eight parameters:

$$w(\sigma^1, \sigma^2; \sigma^4, \sigma^3) = a_0\left(1 + \sum_{i<k}^{4} a_{ik}\sigma^i\sigma^k + a_4\sigma^1\sigma^2\sigma^3\sigma^4\right). \quad (4)$$

The numbering of the spins in the expression (4) for the statistical weight in the elementary plaquette of the lattice is shown in Fig. 2.

Note that the generalized Ising model in the absence of an external field in terms of dipole arrows unambiguously corresponds to (at the statistical-weight level) the eight-vertex model with the external field [8].

The BBS model under consideration given by Eq. (2) corresponds to the following set of the parameters of Boltzmann weight (4):

$$\begin{aligned}
a_0 &= \frac{\alpha}{4}\left(1 + \frac{t\mu}{y}\right)\left(1 + \frac{\mu'}{y'}\right),\\
a_0 a_{14} &= \frac{\alpha}{4}\left(1 - \frac{t\mu}{y}\right)\left(1 + \frac{\mu'}{y'}\right),\\
a_0 a_{23} &= \frac{\alpha}{4}\left(1 + \frac{t\mu}{y}\right)\left(1 - \frac{\mu'}{y'}\right),\\
a_0 a_4 &= \frac{\alpha}{4}\left(1 - \frac{t\mu}{y}\right)\left(1 - \frac{\mu'}{y'}\right),\\
a_0 a_{24} &= \frac{\alpha t}{4yy'}(1 + x\mu)\left(1 + \frac{x'\mu'}{t}\right),\\
a_0 a_{12} &= \frac{\alpha t}{4yy'}(1 - x\mu)\left(1 + \frac{x'\mu'}{t}\right),\\
a_0 a_{34} &= \frac{\alpha t}{4yy'}(1 + x\mu)\left(1 - \frac{x'\mu'}{t}\right),\\
a_0 a_{13} &= \frac{\alpha t}{4yy'}(1 - x\mu)\left(1 - \frac{x'\mu'}{t}\right).
\end{aligned} \quad (5)$$

Using the additional Grassmann-field method [5], the partition function of the generalized Ising model on the $L \times M$ plane lattice with periodic boundary conditions can be represented as the following sum of four integrals over the four-component Grassmann field:

$$Z = \mathrm{Tr}(T^M) = (2a_0)^{ML}\frac{1}{2}(Q^{\mathrm{aa}} + Q^{\mathrm{ap}} + Q^{\mathrm{pa}} - Q^{\mathrm{pp}}). \quad (6)$$

Here,

$$Q = \int d[\psi] e^{S[\psi]}, \quad d[\psi] = \prod_r \prod_{j=1}^{4} d\psi_r^j, \quad (7)$$

$r = (x, y)$ are the coordinates of the lattice sites, where $x = 1, 2, \ldots, L$ and $y = 1, 2, \ldots, M$. The action $S[\psi]$ has the form

$$S[\psi] = \frac{1}{2}(\psi \hat{D} \psi) + g\sum_r \psi_r^1 \psi_r^2 \psi_r^3 \psi_r^4, \quad (8)$$

where

$$\hat{D} = \hat{a} + \hat{\nabla} \quad (9)$$

is the lattice analogue of the Dirac operator, antisymmetric matrices $\hat{a}$ and $\hat{\nabla}$ have the form

$$\hat{a} = \begin{pmatrix} 0 & a_{12} & -a_{13} & a_{14} \\ -a_{12} & 0 & a_{23} & -a_{24} \\ a_{13} & -a_{23} & 0 & a_{34} \\ -a_{14} & a_{24} & -a_{34} & 0 \end{pmatrix},$$

$$\hat{\nabla} = \begin{pmatrix} 0 & -\nabla_{-x} & \nabla_{-x}\nabla_{-y} & \nabla_{-y} \\ \nabla_x & 0 & \nabla_{-y} & \nabla_x\nabla_{-y} \\ -\nabla_x\nabla_y & -\nabla_y & 0 & -\nabla_x \\ -\nabla_y & -\nabla_{-x}\nabla_y & \nabla_{-x} & 0 \end{pmatrix},$$

and the operators ∇_x and ∇_y of the one-step shift in the horizontal and vertical directions, respectively, are specified as

$$\nabla_x\psi_{(x,y)} = \psi_{(x+1,y)}, \quad \nabla_y\psi_{(x,y)} = \psi_{(x,y+1)},$$
$$\nabla_x^T = \nabla_{-x} = \nabla_x^{-1}, \quad \nabla_y^T = \nabla_{-y} = \nabla_y^{-1}.$$

The superscripts p and a of the terms on the right-hand side of Eq. (6) correspond to the periodic and antiperiodic boundary conditions, respectively, that are specified as

$$(\nabla_x^{\mathrm{p}})^L = 1, \quad (\nabla_x^{\mathrm{a}})^L = -1,$$
$$(\nabla_y^{\mathrm{p}})^M = 1, \quad (\nabla_y^{\mathrm{a}})^M = -1.$$

The constant g in the quartic term in action (8) is expressed in terms of the parameters of Boltzmann weights (4) as

$$g = a_4 - a_{12}a_{34} + a_{13}a_{24} - a_{14}a_{23}. \tag{10}$$

If the parameters of the model are such that $g = 0$ (free-fermion condition), the quartic term in action (8) vanishes and integrals (7) are expressed in terms of the Pfaffians of the matrix $\hat{D}$. Representation (6) coincides in form with the classical solution of the two-dimensional Ising model by the Pfaffian method [9] and reproduces the corresponding result in this particular case.

It is easy to verify that parameters (5) of the BBS model satisfy the free-fermion condition $g = 0$. For this reason, the partition function of this model, as well as all eigenvalues of the transfer matrix, is calculated elementarily.

Let D_{qp} be the Fourier transform ($\nabla_{\pm x} \longrightarrow e^{\pm iq}$, $\nabla_{\pm y} \longrightarrow e^{\pm ip}$), of the matrix $\hat{D}$ given by Eq. (9). Then,

$$Q = \mathrm{Pf}(\hat{D}) = \prod_{qp} |D_{qp}|^{1/2}, \tag{11}$$

where q and p are the quasimomentum components taking (half-)integer values (in $2\pi/L$ and $2\pi/M$ units, respectively) in the Brillouin zone in the case of (anti)periodic boundary conditions. [In what follows, we call this set of values the "(anti)periodic" spectrum.]

The determinant of the 4×4 matrix D_{qp} has the form

$$\begin{aligned} d_{qp} &= |D_{qp}| = C_1 + C_2\cos q + C_3\cos p \\ &\quad + C_4\cos q\cos p + C_5\sin q\sin p, \end{aligned} \tag{12}$$

where

$$\begin{aligned} C_1 &= \frac{1}{4}(d_{00} + d_{0\pi} + d_{\pi 0} + d_{\pi\pi}), \\ C_2 &= \frac{1}{4}(d_{00} + d_{0\pi} - d_{\pi 0} - d_{\pi\pi}), \\ C_3 &= \frac{1}{4}(d_{00} - d_{0\pi} + d_{\pi 0} - d_{\pi\pi}), \\ C_4 &= \frac{1}{4}(d_{00} - d_{0\pi} - d_{\pi 0} + d_{\pi\pi}), \end{aligned} \tag{13}$$

$$C_5 = -C_4 \text{ at } (a_{12}, a_{23}, a_{24}) \longrightarrow -(a_{12}, a_{23}, a_{24});$$

$$\begin{aligned} d_{00} &= (1 + a_4 - a_{12} - a_{34} + a_{14} + a_{23} + a_{13} + a_{24})^2, \\ d_{0\pi} &= (1 + a_4 - a_{12} - a_{34} - a_{14} - a_{23} - a_{13} - a_{24})^2, \\ d_{\pi 0} &= (1 + a_4 + a_{12} + a_{34} + a_{14} + a_{23} - a_{13} - a_{24})^2, \\ d_{\pi\pi} &= (1 + a_4 + a_{12} + a_{34} - a_{14} - a_{23} + a_{13} + a_{24})^2. \end{aligned} \tag{14}$$

Note that the critical surface in the space of the parameters a_{ik} is determined by the condition that the right-hand side of any of Eqs. (14) vanishes.

Using Eq. (5) for the BBS model, we obtain

$$C_1 = \frac{\alpha^2}{2a_0^2y^2y'^2}(y^2y'^2 + x^2x'^2\mu^2\mu'^2 + t^2(1 + \mu^2\mu'^2)),$$

$$C_2 = \frac{\alpha^2}{a_0^2y^2y'^2}(xx'yy' - t^2)\mu\mu',$$

$$C_3 = \frac{\alpha^2}{2a_0^2y^2y'^2}(y^2y'^2 + x^2x'^2\mu^2\mu'^2 - t^2(1 + \mu^2\mu'^2)),$$

$$C_4 = \frac{\alpha^2}{a_0^2y^2y'^2}(xx'yy' + t^2)\mu\mu',$$

$$C_5 = \frac{\alpha^2}{a_0^2y^2y'^2}(xy + x'y')t\mu\mu'.$$

The product with respect to one of the components of the quasimomentum in Eq. (11) is calculated in the explicit form by representing the determinant given by Eq. (12) in the factorized form

$$\begin{aligned} 4d_{qp} &= 2u_q - v_q e^{ip} - v_{-q}e^{-ip} \\ &= \rho_q(1 - \nu_q e^{ip})(1 - \nu_{-q}e^{-ip}), \end{aligned} \tag{15}$$

where

$$\begin{aligned} u_q &= 2(C_1 + C_2\cos q), \quad \rho_q = u_q + \sqrt{u_q^2 - V_q V_{-q}}, \\ V_q &= -2(C_3 + C_4\cos q - \mathrm{i}C_5\sin q), \quad \nu_q = V_q/\rho_q. \end{aligned} \tag{16}$$

Then,

$$\begin{aligned} &2^{LM}\prod_{qp}|D_{qp}|^{1/2} \\ &= \prod_q \rho_q^{M/2}\left(\prod_p (1 - \nu_q e^{\mathrm{i}p})(1 - \nu_{-q}e^{-\mathrm{i}p})\right)^{1/2} \\ &= \prod_q \rho_q^{M/2}(1 \pm \nu_q^M), \end{aligned} \tag{17}$$

where the plus and minus signs on the right-hand side of Eq. (17) appear for the antiperiodic and periodic spectra for *p*, respectively.

For each pair of terms in Eq. (6), we introduce the notation

$$\begin{aligned} (2a_0)^{LM}\frac{1}{2}(Q^{\mathrm{aa}} + Q^{\mathrm{ap}}) &= Z^{\mathrm{a}}, \\ (2a_0)^{LM}\frac{1}{2}(Q^{\mathrm{pa}} - Q^{\mathrm{pp}}) &= Z^{\mathrm{p}}, \end{aligned} \tag{18}$$

where the superscripts a and p on the right-hand sides correspond to the antiperiodic and periodic spectra, respectively, of the *q* component of the momentum. As a result, we obtain

$$\begin{aligned} Z^{\mathrm{a}} &= (\lambda^{\mathrm{a}})^M \frac{1}{2}\left(\prod_q (1 + \nu_q^M) + \prod_q (1 - \nu_q^M)\right), \\ \lambda^{\mathrm{a}} &= (a_0)^L \prod_q \rho_q^{1/2}, \quad \frac{Lq}{2\pi} \in \mathbb{Z} + \frac{1}{2}; \\ Z^{\mathrm{p}} &= (\lambda^{\mathrm{p}})^M \frac{1}{2}\left(\prod_q (1 + \nu_q^M) - \prod_q (1 - \nu_q^M)\right), \\ \lambda^{\mathrm{p}} &= (a_0)^L \prod_q \rho_q^{1/2}, \quad \frac{Lq}{2\pi} \in \mathbb{Z}. \end{aligned} \tag{19}$$

Expanding the products in Eqs. (19), we arrive at

$$\begin{aligned} Z^{\mathrm{a}} &= (\lambda^{\mathrm{a}})^M \left(1 + \sum_{q_1 < q_2} (\nu_{q_1}\nu_{q_2})^M \right. \\ &\quad \left. + \sum_{q_1 < \ldots < q_2} (\nu_{q_1}\nu_{q_2}\nu_{q_3}\nu_{q_4})^M + \ldots \right), \\ Z^{\mathrm{p}} &= (\lambda^{\mathrm{p}})^M \left(\sum_q \nu_q^M + \sum_{q_1 < q_2 < q_3} (\nu_{q_1}\nu_{q_2}\nu_{q_3})^M + \ldots \right). \end{aligned} \tag{20}$$

The sum of these expressions should coincide with the expansion of the trace of the *M*th power of the transfer matrix in its eigenvalues; i.e.,

$$\mathrm{Tr}(T^M) = Z^{\mathrm{a}} + Z^{\mathrm{p}} = \lambda_1^M + \lambda_2^M + \ldots + \lambda_{2^L}^M$$

for all values of *M*, in particular, up to $M = 2^L$. This system of 2^L equations for eigenvalues λ_k has the single solution $(\lambda^{\mathrm{a,\,p}}\prod_{k=1}^{n}\nu_{q_k})$ (up to renumbering). It is easy to see from definitions (16) for ν_q that $|\nu_q| < 1$ for $L \neq \infty$. Therefore, the maximum eigenvalue is λ^{a} given in Eqs. (19).

Representation (20) not only provides explicit expressions for all 2^L eigenvalues of the transfer matrix but also evidently specifies a classification of eigenvalues. First, it is seen from Eqs. (20) that the eigenvalues are characterized by a certain number of momenta and by their specific values, which is a consequence of the translational invariance of the system. Second, they are divided into two families: the first family with an even number of momenta ("particles") with the antiperiodic spectrum $\lambda^{\mathrm{a}}(q_1, \ldots, q_{2n})$ including vacuum $\lambda^{\mathrm{a}}(\varnothing) = \lambda^{\mathrm{a}}$ and the second family with an odd number of particles and the periodic spectrum for momenta $\lambda^{\mathrm{p}}(q_1, \ldots, q_{2n+1})$ including the "one-particle" state

$$\lambda^{\mathrm{p}}(q) = \lambda^{\mathrm{p}}\nu_q = \lambda^{\mathrm{p}}e^{-\gamma_q + i\Theta_q}.$$

Here,

$$u_q/|V_q| = \cosh\gamma_q, \quad \Theta_q = \arg(V_q). \tag{21}$$

In terms of this notation, the resulting expressions for the eigenvalues of the transfer matrix have the form

$$\begin{aligned} \lambda^{\mathrm{a}}(q_1, \ldots, q_{2n}) &= \lambda^{\mathrm{a}}\exp\left\{\sum_{k=1}^{2n}(-\gamma_{q_k} + \mathrm{i}\Theta_{q_k})\right\}, \\ \frac{Lq_k}{2\pi} &\in \mathbb{Z} + \frac{1}{2}, \end{aligned} \tag{22}$$

$$\begin{aligned} \lambda^{\mathrm{p}}(q_1, \ldots, q_{2n+1}) &= \lambda^{\mathrm{p}}\exp\left\{\sum_{k=1}^{2n+1}(-\gamma_{q_k} + \mathrm{i}\Theta_{q_k})\right\}, \\ \frac{Lq_k}{2\pi} &\in \mathbb{Z}. \end{aligned} \tag{23}$$

The appearance of the phase Θ_q in Eqs. (22) and (23) for eigenvalues indicates that the system evolves not only in "time," but also in "space." The phase Θ_q disappears if the coefficient C_5 in Eq. (12) vanishes, which imposes a certain constraint on the parameters of Boltzmann weights (4). As seen from Eqs. (22) and (23), at $\Theta_q = 0$, the spectrum of eigenvalues corresponding to multiparticle states is strongly degenerate, because $\gamma_q = \gamma_{-q}$ and, therefore, the sums $\sum\gamma_{q_k}$ with different sets of momenta can be equal to each other. If $\Theta_q \neq 0$, degeneration is removed and this property can be useful for calculation of eigenvectors and form factors.

Before presenting the formulas for the eigenvalues of the transfer matrix in terms of parameters (2) and (5) of the BBS model, we introduce the notation

$$\begin{aligned} A_q &= 1-2\mu\mu'\cos q+\mu^2\mu'^2,\\ B_q &= \mu\mu'(xy+x'y')\sin q,\\ C_q &= y^2y'^2+2xx'\mu\mu'yy'\cos q+x^2x'^2\mu^2\mu'^2,\\ D_q &= A_qC_q-B_q^2. \end{aligned} \tag{24}$$

Then,

$$\begin{aligned} u_q &= \frac{\alpha^2}{a_0^2y^2y'^2}(A_qt^2+C_q),\\ u_q^2-v_qv_{-q} &= \frac{4\alpha^4t^2}{a_0^4y^4y'^4}D_q. \end{aligned} \tag{25}$$

From Eqs. (16) and (25), it follows that $a_0^2\rho_q$ is a quadratic polynomial of t:

$$\begin{aligned} a_0^2\rho_q &= \frac{\alpha^2}{y^2y'^2}(A_qt^2+C_q+2t\sqrt{D_q})\\ &= \frac{\alpha^2}{y^2y'^2}A_q(t+t_q)(t+t_{-q}) \end{aligned} \tag{26}$$

with the roots $-t_q$ and $-t_{-q}$, where

$$t_q = \frac{1}{A_q}(\sqrt{D_q}-\mathrm{i}B_q). \tag{27}$$

The sign of the root $\sqrt{D_q}$ is fixed by the conditions

$$\begin{aligned} \sqrt{D_q} &= \sqrt{D_{-q}}, \quad q\neq 0,\pi,\\ \sqrt{D_0} &= (\mu\mu'-1)(yy'+xx'\mu\mu'),\\ \sqrt{D_\pi} &= (\mu\mu'+1)(yy'-xx'\mu\mu'). \end{aligned}$$

Since the function $a_0^2v_q = a_0^2\rho_q\nu_q$ in notation (24) has the form

$$\begin{aligned} a_0^2\rho_q\nu_q &= \frac{\alpha^2}{y^2y'^2}(A_qt^2-C_q+2\mathrm{i}tB_q)\\ &= \frac{\alpha^2}{y^2y'^2}A_q(t-t_q)(t+t_{-q}), \end{aligned} \tag{28}$$

using Eqs. (26) and (28), it is easy to verify that

$$\nu_q = \frac{t-t_q}{t+t_q}.$$

Finally, the formulas for the eigenvalues of the transfer matrix have the form

$$\lambda^{\mathrm{a}}(q_1,\ldots,q_{2n}) = \lambda^{\mathrm{a}}\prod_{k=1}^{2n}\frac{t-t_{q_k}}{t+t_{q_k}}, \quad \frac{Lq_k}{2\pi}\in\mathbb{Z}+\frac{1}{2}, \tag{29}$$

$$\lambda^{\mathrm{p}}(q_1,\ldots,q_{2n+1}) = \lambda^{\mathrm{p}}\prod_{k=1}^{2n+1}\frac{t-t_{q_k}}{t+t_{q_k}}, \quad \frac{Lq_k}{2\pi}\in\mathbb{Z}, \tag{30}$$

where t_{q_k} values are given by Eq. (27), and

$$\lambda^{\mathrm{a}} = \frac{\alpha^L(1+\mu^L\mu'^L)}{y^Ly'^L}\prod_q(t+t_q),$$

$$\lambda^{\mathrm{p}} = \frac{\alpha^L(1-\mu^L\mu'^L)}{y^Ly'^L}\prod_q(t+t_q).$$

A similar expression for the eigenvalues was obtained for the particular case of $x'=x$, $y'=y$, and $\mu'=\mu$ in [6] using the functional relation method. However, we again emphasize that, in contrast to this method, which provides only possible eigenvalues of the transfer matrix (without indicating their multiplicities: 0, 1, or more), the method described in this work, as is seen from the above formulas, provides a set of the eigenvalues unambiguously.

This work was supported by INTAS (grant no. 03-51-3350), the Ukrainian–French project “Dnipro,” and the Ukrainian State Foundation for Fundamental Research (project no. 2.7/00152).

REFERENCES

1. R. J. Baxter, J. Stat. Phys. **57**, 1 (1989).
2. V. V. Bazhanov and Yu. G. Stroganov, J. Stat. Phys. **59**, 799 (1990).
3. R. J. Baxter, V. V. Bazhanov, and J. H. H. Perk, Int. J. Mod. Phys. B **4**, 803 (1990).
4. R. J. Baxter, Phys. Rev. Lett. **94**, 130 602 (2005).
5. A. I. Bugrij, in *Electron–Electron Correlation Effects in Low-Dimensional Conductors and Superconductors*, Ed. by A. A. Ovchinnikov and I. I. Ukrainskii (Springer, Berlin, 1991), p. 135.
6. H. Au-Yang, B.-Q. Jin, and J. H. H. Perk, J. Stat. Phys. **102**, 471 (2001).
7. R. J. Baxter, J. Stat. Phys. **117**, 1 (2004).
8. R. J. Baxter, *Exactly Solved Models in Statistical Mechanics* (Academic, London, 1982; Mir, Moscow, 1985).
9. B. M. McCoy and T. T. Wu, *The Two-Dimensional Ising Model* (Harvard Univ. Press, Cambridge, 1973).

Translated by R. Tyapaev